

5-2019

Lithium molybdate-sulfur battery.

Ruchira Ravinath Dharmasena
University of Louisville

Follow this and additional works at: <https://ir.library.louisville.edu/etd>

 Part of the [Condensed Matter Physics Commons](#), and the [Energy Systems Commons](#)

Recommended Citation

Dharmasena, Ruchira Ravinath, "Lithium molybdate-sulfur battery." (2019). *Electronic Theses and Dissertations*. Paper 3148.
<https://doi.org/10.18297/etd/3148>

This Doctoral Dissertation is brought to you for free and open access by ThinkIR: The University of Louisville's Institutional Repository. It has been accepted for inclusion in Electronic Theses and Dissertations by an authorized administrator of ThinkIR: The University of Louisville's Institutional Repository. This title appears here courtesy of the author, who has retained all other copyrights. For more information, please contact thinkir@louisville.edu.

LITHIUM MOLYBDATE-SULFUR BATTERY

By

Ruchira Ravinath Dharmasena

B.S., University of Peradeniya, Sri Lanka, 2009

M.S., University of Louisville, USA, 2014

A Dissertation

Submitted to the Faculty of the

College of Art and Science at the University of Louisville

In Partial Fulfilment of the Requirement

for the Degree of

Doctor of Philosophy in Physics

Department of Physics and Astronomy

University of Louisville

Louisville, Kentucky

May 2019

LITHIUM MOLYBDATE-SULFUR BATTERY

By

Ruchira Ravinath Dharmasena

B.S., University of Peradeniya, 2009

M.S., University of Louisville, 2014

A Dissertation Approved on

April 25th, 2019

By the Following Dissertation Committee:

Dr. Gamini Sumanasekera (Dissertation Director)

Dr.Chakram. S. Jayanthi

Dr.Ming Yu

Dr. Mahendra. K. Sunkara

ACKNOWLEDGEMENTS

First, I would like to thank my advisor Dr. Gamini Sumanasekara and co-advisor Dr. Mahendra K. Sunkara for the unconditional support and mentorship they showed throughout my academic career at the University of Louisville. I must thank Dr. Chakram. S. Jayanthi and Dr. Ming Yu for reviewing my dissertation as committee members. The Department of Physics & Astronomy and the Conn Center for Renewable Energy Research-University of Louisville played a vital role in my Ph.D research work.

There are many other staff members and friends who showed their support towards the success of my Ph.D research work. I need to thank Dr. Arjun K. Thapa for sharing his expertise in battery research and Josh Rimmer at the machine shop-Department of Physics & Astronomy for helping me to make parts for my research. Dr. C. Davis and Mary Gayle were also very influential during my Ph.D studentship at the Department of Physics and I humbly grateful for their service. Also, I need to remind my lab colleagues, Muhammad Zain Akram and Rong Zhao for their support in the lab.

Completing the doctoral degree is a long-awaited achievement for me and words cannot explain how grateful I'm for the continuous dedication of my dearest parents to educate me.

Finally, I would like to thank my loving sisters for being there to share my happiness and sadness and my loving wife Dilshani for being a very supportive and a caring companion throughout this dissertation research work.

ABSTRACT

LITHIUM MOLYBDATE-SULFUR BATTERY

Ruchira Ravinath Dharmasena

April 25th 2019

Rechargeable energy storage systems play a vital role in today's automobile industry with the emergence of electric vehicles (EVs). In order to meet the targets set by the department of energy (DOE), there is an immediate need of new battery chemistries with higher energy density than the current Li-ion technology. Lithium-sulfur (Li-S) batteries have attracted enormous attention in the energy-storage, due to their high specific energy density of 2600 Wh kg⁻¹ and operational voltage of 2.0 V.

Despite the promising electrochemical characteristics, Li-S batteries suffer from serious technical challenges such as dissolution of polysulfides Li_2S_x ($3 \leq x \leq 8$) in the electrolyte and the shuttling of polysulfide between the sulfur cathode and the lithium metal anode hindering cycling efficiency and life. There is also an immediate need to replace lithium metal (as the anode in Li-S batteries) with a suitable material.

To improve the cyclability of Li-S battery, a novel method is described using mesoporous TiO_2 to prevent the loss of active material from the sulfur cathode. Herein, the surface adsorbance of TiO_2 for lithium polysulfides is used to prevent the leaking of soluble polysulfides into the electrolyte. Hence, cyclability with high specific capacity is achieved.

The mesoporous TiO₂ (titania) coated carbon-sulfur cathodes exhibit a retention capacity of 980 mAhg⁻¹ over 100 cycles at C/3 rate (433 mA g⁻¹) vs lithium metal anode.

Further, pre-lithiated α -MoO₃ is investigated as a state-of-the art anode material for Li-S batteries. α -MoO₃ demonstrates lithiation potential of \sim 0.2 V with a specific capacity of \sim 1000 mAh g⁻¹. Herein, α -MoO₃ are synthesized by two different techniques; direct synthesis by Hot Wire CVD (HWCVD) technique and 40% H₂/Ar reduction of impure MoO₃. The initial specific charge capacities of these material are found to be over 1000 mAh g⁻¹. The α -MoO₃ electrodes of different morphologies are then assembled with mesoporous TiO₂ coated sulfur cathode to make S-Li_{1.33}Mo_{0.66}O₂ full cell, achieving initial capacity of 905 mAh g⁻¹ at C/10 rate and 635 mAh g⁻¹ at C/3 rate. Finally, a novel cell design is demonstrated, allowing manufacture of high energy density lithium molybdate-sulfur batteries in one step process.

In this dissertation, high energy density cathodes based on mesoporous titania coated sulfur and pre-lithiated anodes based on α -MoO₃ are developed for Li-S batteries by analyzing their electrochemical properties. Finally, these electrode materials are used to manufacture commercially viable Li-S pouch cells with >300 Wh kg⁻¹ energy density over 100 cycles as the outcome of this dissertation.

TABLE OF CONTENTS

ACKNOWLEDGEMENTS	iii
ABSTRACT.....	v
LIST OF TABLES.....	xii
LIST OF FIGURES.....	xiii
CHAPTER 01 INTRODUCTION.....	1
1.1 Motivation.....	1
1.2 Challenges and limitations of rechargeable battery technologies	5
1.2.1 Li-ion batteries.....	5
1.2.2 Li-Air batteries.....	6
1.2.3 Rechargeable magnesium batteries (RMB).....	7
1.3 Lithium-Sulfur (Li-S) batteries	8
1.4 Proposed Concepts for a High Capacity Li-S Battery.....	10
1.4.1 Sulfur cathode.....	10

1.4.2 Pre-lithiate anoded.....	12
1.5 Dissertation objectives.....	17
CHAPTER 02 BACKGROUND.....	19
2.1 Scope.....	19
2.2 Chemistry of rechargeable batteries.....	19
2.2.1 Li-ion batteries (LIB).....	19
2.2.2 Li-Air batteries	22
2.2.3 Magnesium-sulfur batteries.....	23
2.2.4 Lithium-Sulfur batteries (Li-S).....	24
2.3 Proposed electrolytes for Li-S batteries.....	26
2.4 Challenges associated with developing a high capacity sulfur cathode.....	31
2.5 State-of-the art α -MoO ₃ anode material for high capacity Li-S batteries.....	34
2.6 Instruments of material and electrochemical characterization.....	36
2.6.1 Material characterization	36
2.6.1.1 X-ray diffraction (XRD) technique	36
2.6.1.2 Scanning electron microscope (SEM) imaging.....	37
2.6.1.3 X-ray photo electron spectroscopy (XPS) analysis.....	37
2.6.1.4 Thermogravimetric analysis (TGA).....	37
2.6.2 Electrochemical characterization.....	38

2.6.2.1 Galvanostatic electrochemical characterization.....	38
2.6.2.2 Potentiostatic electrochemical characterization.....	38
CHAPTER 03 MESO-POROUS TiO ₂ COATED SULFUR CATHODE.....	38
3.1 Scope.....	40
3.2 Introduction	40
3.3 Mesoporous TiO ₂ coating as a polysulfide adsorbing agent	41
3.4 Material synthesis for sulfur/carbon electrodes.....	43
3.4.1 Carbonized microfiber (CMF) based sulfur cathode.....	43
3.4.2 Activated carbon (ACP) based sulfur cathode.....	47
3.5 Coin cell assembling for electrochemical testing.....	47
3.6 Electrochemical and structural analysis	50
3.7 Results and discussion.....	51
3.8 Conclusions.....	65
CHAPTER 04 ANODE DEVELOPMENT USING α -MoO ₃ FOR HIGH CAPACITY LI-S BATTERIES	67
4.1 Scope.....	67
4.2 Introduction.....	67
4.3 α -MoO ₃ synthesis and S-Li@MoO ₃ full cell assembling in coin cell format	69
4.4 Electrochemical and structural analysis.....	71

4.5 Characterization.....	71
4.6 Results and discussion.....	72
4.7 Conclusions	82
CHAPTER 05 HIGH ENERGY DENSITY LITHIUM MOLYBDATE-SULFUR	
POUCH CELL FORMATION.....	
5.1 Scope.....	83
5.2 Material preparation	83
5.3 Electrochemical measurements of lithium molybdate -sulfur pouch cell.....	89
5.4 Capacity matching of cathode and anode.....	91
5.5 Capacity retention and voltage profile improvement using MoO ₃ nano-wires in anode formation.....	97
5.6 Scale-up of sulfur cathode and α -MoO ₃ anode fabrication.....	100
5.7 Electrode formation and assembling of high energy density 1.5 V, 700 mAh Li-S pouch cell.....	103
5.8 Conclusions.....	108
REFERENCES	110
APPENDICES.....	116

Appendix 1:

A1. Half-cell electrochemical characteristics of CMF based sulfur cathode.....116

Appendix 2:

A2.1 Half-cell electrochemical characteristics of HWCVD deposited α -MoO₃ vs Lithium.....117

A2.2 Half-cell electrochemical characteristics α -MoO₃ powder vs Lithium.....118

Appendix 3:

A3.1 Electronic and optical properties of MoO₃.....119

A3.2 Optical Properties of MoO₃ using UV absorption technique.....119

Appendix 4:

A4.1 Electronic properties of α -MoO₃ using four probes technique.....122

Appendix 5:

A5.1 Effect of the lithiation on the Charge Transfer Resistance of α -MoO₃127

CURRICULAM VITAE.....131

LIST OF TABLES

Table 1.1 USABC Goals for Advance High-Performnace Batteries for Electric Vehicles (EV) Applications. Published by USABC 2019.....	3
Table 2.1 popular Li-ion battery technologies and their properties	21
Table 5.1 Specific capacity of electrodes in mAhg^{-1} with reference to the capacity curves shown in figure 5.1.....	93
Table 5.2 Capacity values for baseline 35 Ah cell	94
Table 5.3 Required mass loading calculation for the given example.....	97
Table 5.4 capacity matching and required mass loading for 700 mAh S-MoO ₃ full cell	105
Table 5.5 Specific energy densities of lithium molybdate-sulfur batteries made with pre-lithiated α -MoO ₃ from different synthesis techniques.	109

LIST OF FIGURES

Figure 1.1 The next generation Li-ion and beyond Li-ion (BLI) cost estimation	4
Figure 1.2 Experimental gravimetric and volumetric capacity of anode materials for the lithiated state in dependence to their half-cell potential. Dotted lines are the target lines for both energy densities in respect to three different classes of cathodes: reference layered (middle line), high-voltage (lower line and conversion (upper line) cathode material.....	15
Figure 1.3 Delithiation voltage profiles of selected anode materials. Possible upper cut-off voltage of the anodes.....	16
Figure 2.1 Schematic of a typical Li-ion battery.....	20
Figure 2.2 Diagram of a non-aqueous Li-Air battery	23
Figure 2.3 Diagram of a Mg-S battery.....	24
Figure 2.4 Schematic of a Li-S battery.....	25
Figure 2.5 Charge and discharge curves a typical lithium sulfur battery.....	25
Figure 2.6 Schematic of a Li-S battery showing the actions of solvent, salt and additive	27
Figure 2.7 Chemical structures of solvents used in electrolytes for Li-S batteries.....	28
Figure 2.8 Chemical structures of salts used in electrolytes for Li-S batteries.....	29
Figure 2.9 Schematic of polysulfide dissolution, SEI formation	30

Figure 2.10 Schematics of a Li-S cell and its electrochemical reactions.....	32
Figure 2.11 Illustration of the shuttle mechanism of a Li-S battery.....	33
Figure 2.12 Illustration of dendrite formation process (a) lithium dissolution (b) lithium deposition.....	34
Figure 2.13 (a) Thermodynamically stable orthorhombic α - MoO_3 (b) meta stable β - MoO_3	36
Figure 2.14 Cross section of TGA instrument	38
Figure 3.1 STM image of sulfur adsorbed on TiO_2 (110). S atoms are located at the bright spots.....	42
Figure 3.2 Unit cell of Rutile TiO_2	42
Figure 3.3 Unit cell of Anatase phase	42
Figure 3.4 (a) fiber collector drum (b) synthesized poly-acrylonitrile fiber mat.....	44
Figure 3.5 Electrospinning setup	44
Figure 3.6 SEM images of the carbonized microfibers	45
Figure 3.7 SEM image of the sulfur diffused carbonized fiber electrode	46
Figure 3.8 Figure 3.8. Free standing electrode made of activated carbon.....	47
Figure 3.9 Schematic diagram of the titania coated electrode (a) without electrical contact (b) with electrical contact for ACP supported sulfur cathode in a Li-S cell. The SEM images of the sulfur support and the titania coating and (c) pore width distribution (d) N_2 adsorption–desorption isotherms for anatase titania powder are also shown	49

Figure 3.10: Gravimetric capacity results of ACP based sulfur electrodes; (a) potential vs. specific capacity curves of optimized ACP based titania coated sulfur cathode, (b) comparison of the discharge capacity of various ACP based cathodes; (i) titania coated sulfur cathode with (purple) and without (blue) improved electrical connection to the current collector and (ii) uncoated electrodes (red); left axis represent the discharge capacity and the right axis represents the coulombic efficiency for the optimized sulfur cathode (c) rate capability performances of ACP52

Figure 3.11. Electrical conductivity measurements of the cathode material: Nyquist plots for titania coated sulfur electrode (a) with part of the backside uncoated (exposed) (b) both sides coated with titania. The inserts show the equivalent circuit network utilized for impedance analysis. (c) and (d) show the side view of the titania coated electrode with provisions for electrical bridging and the electrode with both sides completely coated with titania respectively55

Figure 3.12 Cyclic voltammetry measurement of (a) uncoated sulfur electrode (b) titania coated sulfur electrode (ACP based) at the voltage range 2.8-1.5 V at scan rate of 0.3 mVs⁻¹56

Figure 3.13 (a) Raman spectra of titania coated sulfur electrodes (ACP based) before and after discharge (b) XPS surface analysis for titania coating (c) XRD spectra of titania coated sulfur electrodes before and after discharge, spectra for Li₂S and TiO₂ powders are also shown for comparison. The * represents the signature of the polymer bag and the dotted vertical lines represent the aluminum substrate.....59

Figure 3.14 Schematics of the chemical processes in (a) uncoated and (b) titania coated sulfur electrode in Li-S battery.....	61
Figure 3.15 Fitting parameters of EIS data for ACP based sulfur cathode to an equivalent electrical circuit model: Each plot contains charge transfer resistance at cathode (R_{cct}), charge transfer resistance at anode (R_{act}), electrolyte resistance (R_e), and interface resistance (R_{int}). Plots (a) and (b) represent results for titania coated and uncoated samples respectively against DOD; plots (c) and (d) represent results for coated and uncoated samples respectively against DOC. Plots (e) and (f) represent results for titania coated and uncoated samples respectively against cycle number	62
Figure 4.1. Synthesis process of α - MoO_3 using Hot Wire CVD technique	71
Figure 4.2 <i>In-situ</i> XRD analysis for pre-lithiation of Hot Wire CVD deposited MoO_3 powder in teflonized acetylene black carbon binder electrode. α - MoO_3 [00-005-0508], $Li_{1.33}Mo_{0.66}O_2$ [01-073-2300] and $Li_2Si_2O_5$ [00-015-0637].....	73
Figure 4.3 (a) Potential vs discharge curve of $Li_{1.33} Mo_{0.66}O_2$ -S full cell, at C/10 rate (b), (c) and (d) capacity vs cycle number and coulomb capacity of $Li_{1.33}Mo_{0.66}O_2$ -S full cell at C/10, C/3 and 1 C.lithiated α - MoO_3 synthesized by HFCVD technique	75
Figure 4.4 (a) Cyclic voltammetry curve of $Li_{1.33}Mo_{0.66}O_2$ -S (working electrode vs reference electrode) (b) Schematic of three electrode Swagelok test cell which used for CV.....	76
Figure 4.5 (a) discharging and (b) charging curves for impedance analysis. DoD % (percent depth of discharge), DoC % (percent depth of charge). Sharp peaks on discharge and charge curves indicate the points at which the impedance was measured.....	77

Figure 4.6 (a) equivalent circuit for the working electrode and (f) equivalent circuit for counter electrode Nyquist plots of c) working (sulfur) electrode at discharge. d) counter (Li_{1.33}Mo_{0.66}O₂) electrode at discharge e) working electrode at charging, f) counter electrode at charging.....79

Figure 4.7 Fitted resistance values at depth of discharge (DoD) and depth of charge (DoC) for (a) and (b) working electrode and counter electrode at discharge, (c) and (d) working electrode and counter electrode at charge.....80

Figure 5.1 (a) as prepared MoO₃ after oxidizing at 500 °C (b) α-MoO₃ after reduction in 40 % H₂/Ar at 150 °C (c) XRD spectrums of as prepared MoO₃ and α-MoO₃ after reduction in 40 % H₂/Ar.....85

Figure 5.2 Schematic diagram of the pouch cell (a) before lithiation of α-MoO₃ (b) after lithiation of α-MoO₃. Red dashed lines show the separator completely covering both electrodes. Middle inter layer in green color is the lithium foil supported on a stainless-steel mesh.....88

Figure 5.3 (a) Potential vs specific capacity curve of sulfur-Li half cell (first cycle) (b) Capacity retention and coulombic efficiency of sulfur-Li half cell (c) Potential vs specific capacity of α-MoO₃-Li halfcell, (d) Capacity retention and coulombic efficiency of α-MoO₃-Li half-cell. (Half -cells were cycled at C/3 current rate).....89

Figure 5.4 (a) lithium molybdate-sulfur pouch cell (b) Discharge capacity vs Cycle index (c) Potential vs specific capacity of S-Li_{1.33}Mo_{0.66}O₂ (c) Potential vs specific capacity curve for lithiating the α-MoO₃ (d) Specific capacity retention curve for α-MoO₃ vs Li/Li⁺91

Figure 5.5 (a) charge capacity of positive electrode (b) charge capacity of negative electrode.....	92
Figure 5.6 Capacity balancing in a hypothetical 35 Ah cell.....	95
Figure 5.7. Effective potential range of the negative electrode.....	96
Figure 5.8 Ah capacity matching of positive electrode and negative electrode.....	96
Figure 5.9. (a) charge/ discharge curves of α -MoO ₃ nano-wire cathode and Li anode half cell (b) Potential vs specific capacity curves of α -MoO ₃ (nano-wire)- Li half-cell. Testing were done at C/10 rate.....	98
Figure 5.10. Potential vs specific capacity curves of S cathode and MoO ₃ (nanowire) full cell (discharged at C/10).....	99
Figure 5.11 Capacity retention curves of S-Li@ α -MoO ₃ (nanowire) full cell (a) mAh capacity vs cycle index (b) Energy density vs cycle index (discharged at C/10)	99
Figure 5.12 (a) vibrator attached to the sample holder to shake the sample for efficient reduction (b) Two samples after decanting (c) XRD spectrum comparison of two different MoO ₃ samples separated by sonication and XRD of pure α - MoO ₃ sample (red line).....	102
Figure 5.13 Capacity curves of sulfur cathode and α -MoO ₃ anode.....	103
Figure 5.14 (a) Comparison of reversible and irreversible capacities of cathode and anode, (b) capacity matching for S-Li@MoO ₃ full cell. (black line shows the capacity of MoO ₃ required to have in the anode).....	104
Figure 5.15 (a) Cathode coating on Aluminum (b) Anode coating on Copper.....	106
Figure 5.16 Schematics of cathode electrode.....	106

Figure 5.17 Schematic of anode electrode.....107

Figure 5.18 (a) internal schematic of Li- S pouch cell (b) external appearance of Li-S pouch cell (c) finished pouch cell after L terminal removed after lithiation.....108

CHAPTER 01

INTRODUCTION

1.1 Motivation

In order to improve the driving range (distances after a recharge) of electric vehicles (EVs), better performing rechargeable batteries with higher energy densities than current Li-ion technology are needed. More than a quarter century old Li-ion battery technology uses graphite anodes and transition metal oxide cathodes with total energy density of around 250 Wh kg^{-1} [12]. The high cost and low specific energy density of the electrode materials used in Li-ion batteries are among the main challenges of developing battery packs with energy density comparable to gasoline. Even though there is some room left to improve existing Li-ion technology, it will not be enough to meet future requirements and demands. Instead, the battery innovation needs (i) materials-science breakthroughs, (ii) new electrode chemistries and architectures, (iii) new electrolytes etc. to achieve safe, economical, and long-lasting energy storage systems.

In 2012 the governing body of USA at that time, together with the department of energy (DOE) launched a program called “EV Everywhere Grand Challenge” to boost the production of plug in electric vehicles (PEV) in the United States. DOE has set forth targets to reach this set of goals by 2022. These goals include, (i) lowering the battery costs from \$500/kWh to \$125/kWh (ii) eliminate 30% of vehicle weight (iii) reduce the cost of electric drive from \$30/kWh to \$8/kWh. Also, United States Advanced Battery Consortium (USABC) have published the DOE target for advance battery chemistries for 2019.

According to them, specific energy density at cell level should be 350 Wh kg^{-1} at C/3 discharge rate. The C rate is defined as nC when the battery is fully discharged in 1/n hours. Other specifications provided can be found in table 1.1. To achieve these targets, battery chemistries beyond Li-ion must be considered. An overview of the technologies and their likelihood to achieve the DOE/ U.S DRIVE cost goals are shown in Fig 1.1.

Table 1.1: USABC Goals for Advance High-Performance Batteries for Electric Vehicles (EV) Applications. Published by USABC 2019

End of Life Characteristics at 30 °C	Units	System Level	Cell Level
Peak discharge power density 30s pulse	W/L	1000	1500
Peak specific discharge power, 30s pulse	W/kg	470	700
Peak specific regen power, 10s pulse	W/kg	200	300
Useable energy density @C/3 discharge rate	Wh/L	500	750
Useable specific energy @C/3 discharge rate	Wh/kg	235	350
Useable energy @C/3 discharge rate	kWh	45	N/A
Calendar life	Years	15	15
DST cycle life	Cycles	1000	1000
Cost @ 100K units	\$/kWh	125	100
Operating environments	°C	-30 to +52	-30 to +52
Normal recharge time	Hours	<7 hours	<7 hours
High rate charge	Minutes	80% in 15min	80% in 15min
Maximum operating voltage	V	420	N/A
Minimum operating voltage	V	220	N/A
Peak current. 30s	A	400	400
Unassisted operating at low temperature	%	>70% Usable energy @ C/3 discharge rate at -20 °C	>70% Usable energy @ C/3 discharge rate at -20 °C
Survival temperature range, 24Hr	°C	-40 to +66	-40 to +66
Maximum self-discharge	%/month	<1	<1

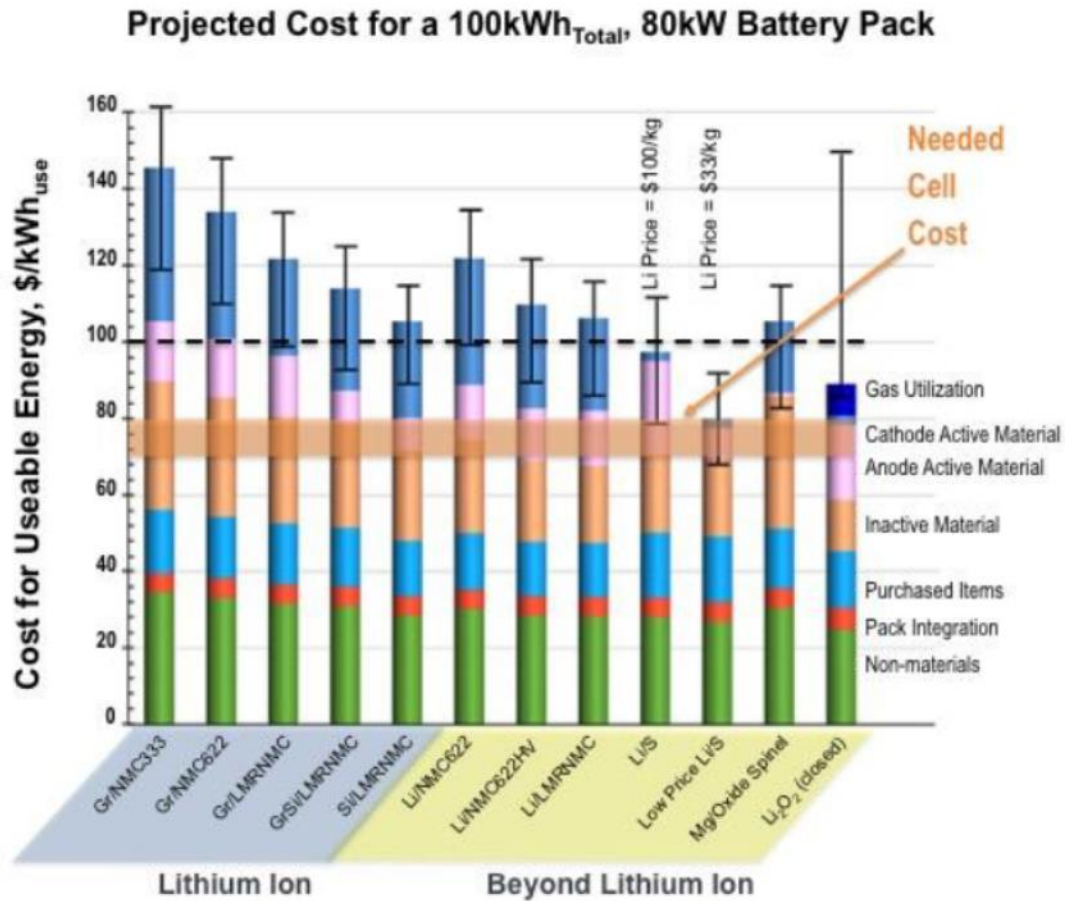


Figure. 1.1 The next generation Li-ion and beyond Li-ion (BLI) cost estimation [14]

According to the information given in Fig. 1.1., Li-S battery chemistry demonstrates promise in terms of the cost per kilowatt hour compared to all other battery chemistries, due to the attractive energy density of sulfur cathode (2500 Wh kg^{-1} vs Lithium). However, the commercialization of Li-S technology is hampered by technical challenges such as poor cycle life, poor rate capabilities, self-discharging issues and unavailability of pre-lithiated anode materials with good stability. Much of today's research on Li-S batteries is focused

on understanding of materials, construction and the fundamental scientific understanding of cell behavior. The importance of this should not be questioned, but there is a need to develop the engineering science and techniques necessary for deployment of Li-S batteries in practical applications which is the main motivation of this dissertation.

1.2 Challenges and limitations of rechargeable battery technologies

1.2.1 Li-ion batteries

The first Li-ion battery was based on a LiCoO_2 cathode and a carbon anode. Upon charging the battery, the cathode becomes $\text{Li}_{1-x}\text{CoO}_2$ by delithiation and the anode converts to Li_xC_6 . The practical capacity of LiCoO_2 anode was found to be 140 mAh g^{-1} which corresponds to $x \approx 0.5$ (i.e., ~50%) of its theoretical value (273 mAh/g). The high possibility of thermal runaway caused by overcharge and the high cost of Cobalt, have led to the investigation of other cathode materials for Li-ion cells with better capacity and cycle life.

Insertion electrodes of Li-ion cells need to have wide compositional range, so that maximum lithium can be extracted and reinserted during charging and discharging to maximize the energy density. In addition, the electrode host material needs to have good transport properties for Li-ion providing high power capability. Carbon in the form of graphite has been the source of anode material in Li-ion batteries thus, the required properties need to be sought in novel cathode materials.

$\text{LiNi}_{0.8}\text{Co}_{0.15}\text{Al}_{0.05}\text{O}_2$ (NCA), spinel electrodes $\text{Li}_{1+x}\text{Mn}_{2-x}\text{O}_4$ and LiFePO_4 have been studied as alternative materials for LiCoO_2 cathode material. Despite of slightly higher practical capacity (180 mAh g^{-1}) of NCA cathode material, its thermal instability on delithiation compromises the safety of Li-ion cells. In contrast Spinel LiMn_2O_4 and LiFePO_4 are significantly more stable but have less capacity of $100\text{-}150 \text{ mAh g}^{-1}$ above 3 V.

Recently developed manganese-based cathodes using Li_2MnO_3 and electrochemically active LiMO_2 ($\text{M}=\text{Mn, Ni, Co}$) have shown that, it can lower the material cost while excess lithium boosts the specific capacity to 250 mAh g^{-1} between 4.6 V and 2.5 V. However, their deliverable capacity decreases dramatically when cycled against graphite anodes thus these Li-ion cells made of Ni-Mn-Co oxides (NMC) suffer severe energy density loss in practical Li-ion cells. Furthermore, these cathode materials have higher operating potentials, and thus needs electrolytes that are stable at higher potentials. Novel electrolytes have been investigated with higher oxidative stability such as sulfones, nitriles and fluorinated solvents. They, however, introduce new problems due to solid electrolyte interphase (SEI) formation.

1.2.2 Li-Air batteries

The lithium air battery is the closest technology to reach the gravimetric capacity of fossil fuel which is around 13000 Wh kg^{-1} [15, 16] when free oxygen is not included in the calculations. Otherwise, at the cell level, Li-Air batteries give 3623 Wh kg^{-1} (when discharged to form Li_2O_2 at 3.1 V) or 5200 Wh kg^{-1} (when discharged to form Li_2O at 2.9 V).

A Li-air battery is comprised of a Li metal anode and an O_2 cathode. Typically, Oxygen is pumped from an external source. Currently, there are three main architectures proposed for Li-Air batteries. These include versions with (i) aqueous electrolyte, (ii) a fully aprotic liquid electrolyte and (iii) a hybrid structure with cathode immersed in aqueous electrolyte and anode immersed in aprotic electrolyte.

Realization of high theoretical capacity and practical application of Li-Air Battery technology is limited by low power output and poor cycle-ability. The non-aqueous electrolytes used in Li-Air batteries are volatile and unstable at high voltages, causing poor cyclability. It is found that, the supplied oxygen can crossover with the electrolyte affecting the overall functionality of the cell. This problem obviously mitigates the cycle life of Li-Air cell. Li_2O and Li_2O_2 depositions on the carbon cathode surface can clog the pores, restricting the oxygen flow, leading to poor capacity. Inefficient cathode structures and catalysis that can access the oxygen efficiently causes significant charge overpotentials.

1.2.3 Rechargeable magnesium batteries (RMB)

Mg metal has more attractive volumetric capacity than lithium metal, i.e., 3832 mAh cm^{-3} vs 2061 mAh cm^{-3} for lithium and it is a less expensive metal than Li, thus cost reduction could be a benefit of using Mg as an anode material. However, Mg lacks the gravimetric capacity and redox potential compared to Li metal. Mg has a gravimetric capacity of 2205 mAh g^{-1} vs 3862 mAh g^{-1} for Lithium. The redox potential of Mg is -2.4 V compared to -3.04 V for Li vs. normal hydrogen electrode (NHE). The Mg anode has demonstrated the absence of dendrite formation upon reversible plating of Mg. Batteries with Mg anode thus alleviate the dendrite formation issue related to Li metal anodes. Commercializing the Mg battery has, however, been a challenge due to the unavailability of practical electrolytes which are stable with Mg anodes. Also, the sluggish kinetics of Mg^{+2} ion limits the energy density of Mg to a few hundred watt-hours per kilogram. It has been found that the formation of the surface layer as a result of metal-electrolyte interface blocks the Mg^{+2} ions thereby preventing reversible electrochemical reactions. This phenomenon is very different

than the SEI (solid-electrolyte interface) formation on Li metal, which protects the Li metal from electrolyte while Li^+ ions can diffuse through the SEI layer. In order to overcome these limitations induced by the Mg metal, insertion type anode materials are proposed. However, these electrodes too face with challenges caused by extremely sluggish magnesium insertion/extraction kinetics and electrode pulverization due to volume change.

There are several proposed cathode materials for Mg rechargeable batteries. Among them cobalt, vanadium, molybdenum, and sulfur-based cathodes are considered. The cells made with the proposed cathode materials and Mg anode demonstrate poor cyclability, low capacity and low operational potential window.

1.3 Lithium-Sulfur (Li-S) batteries

Li-S battery technology have attracted much more attention than any other battery technology due to its ability to penetrate the Li-ion battery technology with higher charge capacity (1675 mAh g^{-1}) and reasonable operating potential of 2.0 V. In addition, sulfur is an abundant element on earth. Therefore, the material cost per kilowatt hour can be much lower compared to the other high energy density battery materials. Considering all these advantages, Li-S batteries undoubtedly a promising battery chemistry that can fulfill current energy needs, especially in EV's.

Li-S batteries, however, are not closer to industrial readiness mainly due to technical challenges. Developing a Li-S battery with high capacity and durability requires, solving the issues related to the both sulfur cathode and lithium metal anode. It has been found that, there are three main factors affecting the poor cyclability of sulfur cathode, i.e., (i) poor electrical conductivity of sulfur (ii) dissolution of polysulfides in the electrolyte during delithiation and lithiation [6] and (iii) polysulfides shuttling between cathode and

anode. During the lithiation process, sulfur first reduces to S_8^{2-} and forms Li_2S_6 and Li_2S_4 thereafter [18, 19] which can lead to active material inaccessible for further electrochemical reactions. The dissolved polysulfides can cause polysulfide shuttling [20-23]. The polysulfide shuttling occurs by migrating dissolved polysulfides between cathode and anode when the battery is charged and discharged. This phenomenon has been studied extensively [20] and it is found that, dissolved polysulfides can be reduced near the anode forming solid Li_2S_2 and Li_2S on the lithium metal causing blockage for Li^+ ions. To mitigate these problems related to the sulfur cathode, various electrolytes has been investigated. Among them, solvents, 1,2-Dimethoxyethane (DME) and 1,3-Dioxolane (DOL) based organic electrolytes are preferable due to their bulky anions which can effectively reduce polysulfide solubility [24]. Dissolution of sulfur can increase the viscosity of the electrolyte thus less viscous electrolytes are selected.

Lithium metal anode mitigates the practical applicability of Li-S batteries due to the problems such as dendrite formation and fire hazard of lithium. Lithium anode is known to build up solid deposits (dendrites) upon charging the Li-S battery causing cathode and anode short circuiting. To avoid these problems related to lithium anode, pre-lithiated anode materials are investigated such as pre-lithiated Si anodes and Sn (Tin) anodes. But they have problems such as high-volume expansion causing electrode degradation. Therefore, there is a huge need for addressing these issues related both cathode and anode in order to develop high capacity and durable Li-S batteries.

1.4 Proposed concepts for a high capacity Li-S battery

1.4.1 Sulfur Cathode

The dissolution of sulfur however is a necessity for proper operation of Li-S batteries [25] while it is the problem of making a durable Li-S battery. When designing a sulfur cathode, therefore, several factors need to be taken into consideration. 1) the sulfur particles need to be encapsulated to minimize the leakage of polysulfides, 2) the electrode material must be properly wetted by electrolyte, 3) good electronic conductivity must be maintained within the bulk electrode. In addition, there are some reports that indicate gas evolution in Li-S cells could also be problematic for their practical applications [26].

Many techniques have been attempted to prevent dissolution of polysulfide from sulfur cathode into the electrolyte. Lin Ma et al. [27] has published an excellent review of these techniques. One of the ideas for improving the cyclability of sulfur cathode is entrapping of sulfur to limit the chain during the lithiation of the cathode. Entrapping of sulfur in micro/meso pores appear to serve this idea [28-33], but the batteries still tend to show continuous decay of capacity. These micro-pores can be made using a silicon template [34]. Meso-porosity can serve as good electrolyte channeling medium as well. Metal-organic framework has also been investigated as a sulfur hosting medium in Li-S batteries [35]. Sulfur has also been stored in nano-cages and nano-space carbon structures elsewhere [36-38].

Sulfur nanoparticles also can be coated with polymers and then carbonized to make the electrode electrically conductive [39-44]. Such coatings are however prone to crack while sulfur is lithiating to longer polysulfides. To avoid such cracking, core shell type coatings were studied [45, 46]. The ability encapsulate sulfur using graphene has been

demonstrated [47-50]. Carbon-nanotubes can also be used to trap sulfur, with the advantage of acting as a barrier to trap polysulfides [51-56]. Carbon nano-fiber interlayer and graphene layers can also be used as a barrier for dissolved polysulfides [57, 58]. The above techniques are all based on physical trapping of polysulfides in the carbon structure thus continuous decay of capacity is expected. Improvement of sulfur cathode cyclability has been attempted through chemical methods as well [59, 60]. Chemically bonded sulfur however does not seem to participate in lithiation reaction while non-bonded sulfur is found to be electrochemically active. Soluble polysulfides trapping by chemisorption of Amine-functionalized carbon has been reported [61] with a significant capacity retention. In addition to the above modifications of cathode electrodes, the use of solid state electrolytes and gel polymer electrolytes are being investigated [62, 63] to alleviate the sulfur dissolution problem.

Anatase TiO_2 has surface defect sites which show adsorbance properties for lithium polysulfides. In addition, TiO_2 shows a good ionic conductivity for Li^+ . Thus, TiO_2 mixed with carbon and sulfur have been investigated by many other researchers to trap soluble polysulfides. Here, a concept of using mesoporous coating comprised of anatase TiO_2 particles on a sulfur/carbon cathode is investigated to prevent migration of polysulfides and enable lithium diffusion. The semiconducting nature of TiO_2 coating introduces technical challenges to obtain a high charge capacity, thus this issue must also be addressed to gain high capacity with good durability.

Synthesizing electrode material for high capacity and durable Li-S battery is approached by four main methods as mentioned above. Those are (i) sulfur encapsulation in micro/meso porous structures (ii) entrapping sulfur by carbon coating and (iii) polysulfide

trapping in carbon fibers or in graphene and (iv) by chemically bonding sulfur with carbon. In all these methods, carbon is the medium for improving electrical conductivity. In this work, it is intended to synthesize low cost carbon structures to host sulfur and then use TiO₂ as a polysulfide trapping barrier.

1.4.2 Pre-lithiated anode

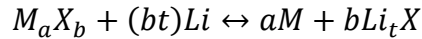
Development of an anode electrode (other than Li metal) for Li-S battery is more challenging than developing cathodes. The reason being the unavailability of many anode materials that need to be pre-lithiated and stable over many cycles. When developing the Li-ion battery, graphite was found to be very popular for the Li-ion batteries. Typically, carbon anode has a gravimetric capacity around 372 mAh g⁻¹, which is large enough for Li-ion battery technology as most of the cathode materials do not exceed the capacity of more than 250 mAh g⁻¹. For high energy density batteries, finding a suitable anode becomes much more challenging. When selecting the anode material, the cathodic and anodic potential as well as capacity matching need to be considered very carefully. In addition to graphite, Si and Sn, especially in nanostructure forms have been studied as anodes for Li-ion batteries [64, 65]. Germanium (Ge) has also been tested as an anode material [66], but the high lithiation potential of 1.0 V for Ge is a disadvantage for Li-ion batteries and its high material cost makes it not suitable to use as an anode material. Graphite is obviously not a good anode material for Li-S batteries, because of its poor capacity [67] compared to the high cathode capacity of sulfur. Si and Sn have been widely investigated as high charge capacity anode materials. They have charge capacities 3570 mAh g⁻¹ [67] and 991 mAh g⁻¹ [68] respectively. Both Si and Sn are known for their high-volume expansion upon lithiation; Si expands about 300% [69, 70] and Sn expands by >250%. This volume

expansion causes pulverization and cracking [69] of the electrode. However, Silicon nano particles and nanowires have proven to be withstand the expansion during lithiation [71]. Cui et al. has shown that silicon nanowire anode architecture can improve the capacity retention while maintaining the structural integrity of the anode [72]. Transverse expansion of silicon nanowires is believed to be the main reason for withstanding the stress upon lithiation. SiO₂ nanowires have also been investigated in Ref [73] as an anode material in Li batteries.

Based on lithiation/de-lithiation characteristics, anode materials of the batteries can be grouped into three classes; (i) intercalation materials (ii) single-phase conversion material (alloying material) and (iii) multi-phase conversion materials. Graphite and titanium oxide are among the most investigated intercalation type anode materials. Intercalation type anode materials demonstrate minimal structural changes during the lithiation/de-lithiation process, e.g., Li₄Ti₅O₁₂ demonstrates comparatively smaller volume changes, thus its stability during the lithiation/de-lithiation is far superior to that of its counterparts. Low gravimetric and volumetric capacity are the main drawbacks of intercalation type materials due to the low number of lithium ions that can be stored per host atom. The single-phase conversion anode materials are the ones with both, reactants and products, are single-phase materials. Silicon can be considered as a single-phase anode material as it can lithiate forming Li₂₂Si₅. In the scientific world, this type of single-phase reactions is called alloying. The multi-phase conversions on the contrary are comprised of two or more reactants or products. Unlike intercalation materials, both single-phase and multi-phase conversion materials undergo significant structural changes during the lithiation and delithiation. Most of the alloying materials are the metals and semi-metals from group IIIa,

IVa and Va of the periodic table. Silicon is the most investigated alloying material. At room temperature it can react with 3.75 lithium ions per Si atom, giving 3570 mAh g⁻¹. Si demonstrates slightly higher delithiation potential (0.4 V) compared to graphite (0.1 V). Tin (Sn) is also a widely investigated anode material with less volume expansion compared to Si and with a delithiation potential of 1 V. Aluminum and Gallium have also been investigated for possible anode materials, but they show a delithiation potential of 1 V, like Tin (Sn). Black phosphorus has also been found as a potential anode material with delithiation potential of 1 V and a specific capacity of 2600 mAh g⁻¹ which is only inferior to lithium metal and silicon.

The reaction of multi-phase conversion materials with lithium can be expressed in a general chemical equation as follows;



Where M=transition metal, X=anion and t=oxidation state of X.

These types of materials typically exhibit theoretical capacities in the range of 650 -1000 mAh g⁻¹ due to their ability to transfer more than one electron per atom and exhibit lower volume expansion compared to alloying anode materials. These kinds of materials demonstrate higher delithiation potentials (1-2.2 V) and poor electronic conductivity and ionic conductivity. In addition, poor cycle life caused by complete structural reorganization during the conversion reaction. Fig. 1.2 shows a good comparison of anode potentials at lithiated state and Fig. 1.3 shows the relationship between delithiation potential vs specific capacity of the most investigated anode materials.

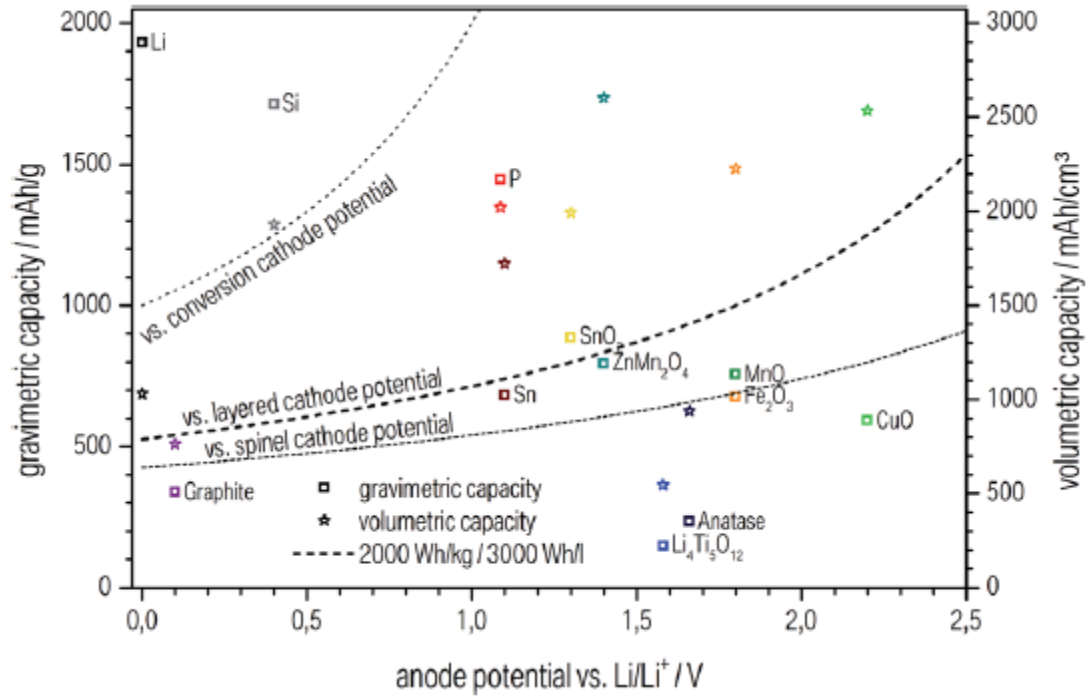


Figure 1.2 Experimental gravimetric and volumetric capacity of anode materials for the lithiated state as a function of their half-cell potential. Dotted lines are the target lines for both energy densities in respect to three different classes of cathodes: reference layered (middle line), high-voltage (lower line) and conversion (upper line) cathode material. [10]

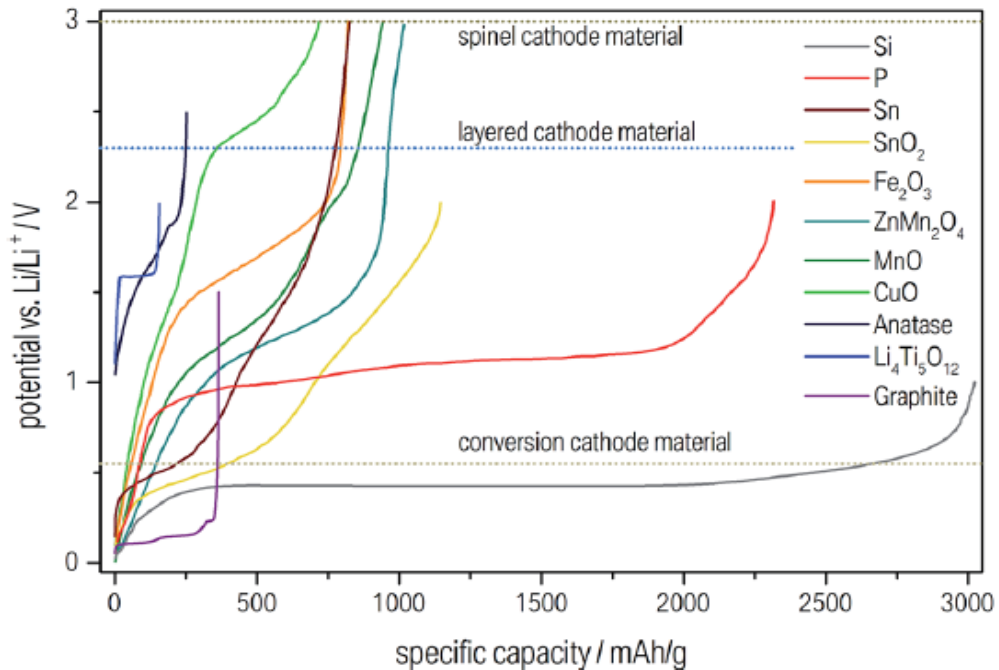


Figure 1.3 Delithiation voltage profiles of selected anode materials with possible upper cut-off voltage of the anodes [10]

The second concept of this dissertation is to investigate α - MoO_3 as a state-of-the-art pre-lithiated anode material for Li-S battery to replace the Li metal anode. This approach improves the safety of Li-S batteries. α - MoO_3 demonstrates a charge capacity of ~ 1000 mAh g^{-1} and a lithiation potential at 0.2 V vs Li and moderately wide potential hysteresis loop with a de-lithiation potential which gives a reasonable ~ 1.7 V to 1.4 V operation discharge potential plateau, when assemble with the sulfur cathode. In addition, lithiation of α - MoO_3 undergo multi-phase conversion reaction which demonstrate smaller volume change than in alloying materials such as Si and Sn. However, pre-lithiation of α - MoO_3 is the major technical challenge of this work. Thus, newer approaches need to be investigated to synthesize pre-lithiated α - MoO_3 with high yield.

1.5 Dissertation objectives

The main goal of this work is to demonstrate a commercially viable Li-S battery with high capacity and durability. The following are dissertation objectives in addressing challenges associated with both anode and cathodes.

- (i) Sulfur cathode development: The main challenges for developing a durable sulfur cathode are polysulfide dissolution in liquid electrolyte, polysulfide shuttle causing a blockage for Li^+ ions at the Li anode and poor electrical conductivity of sulfur.
- (ii) Pre-lithiated anode development: lithium metal anode has problems such as dendrite formation at the anode and high reactivity of lithium with air which poses a fire hazard. Therefore, it is important to find a pre-lithiated anode or a way to pre-lithiate anode materials. There are no known pre-lithiated anode materials that could be made easily.

The overall objective of this work is to demonstrate a high energy density Li-S pouch cell using the mesoporous TiO_2 coated sulfur cathode and pre-lithated $\alpha\text{-MoO}_3$ anode. To approach this goal, special cell design is investigated which simplifies the pouch cell formation towards a commercially viable battery technology.

The dissertation is organized as follows. Chapter 2 provides the background of the known high energy density rechargeable batteries is discussed including their advantages and disadvantages. Chapter 3 details the experimental procedures implemented for cathode and anode development and electrochemical techniques used for testing cells. Chapter 4 is mainly focused on developing a pre-lithiated $\alpha\text{-MoO}_3$ as a novel anode material and its implementation in making Li-S full cells. Chapter 5 includes material quality

improvements and technical details of assembling a high energy density lithium molybdate-sulfur pouch cell.

CHAPTER 02

BACKGROUND

2.1 Scope

This chapter is focusing on outlining the chemistry of Li-ion batteries, Li-Air batteries, Magnesium sulfur batteries and Lithium-sulfur batteries. The chemistry of Li-S battery is described with a detailed description of polysulfide dissolution mechanism and polysulfide shuttling phenomena. A brief review of electrolytes of Li-S batteries is also given. In addition, an outline of electrochemical and material characterization techniques which were used in this dissertation is given at the end of this chapter.

2.2 Chemistry of rechargeable batteries

2.2.1 Li-ion batteries (LIB)

Li-ion batteries sometimes recognized as rocking chair batteries due to its characteristic Li-ion mass transport between the two electrodes. In a typical Li-ion battery, cathode is a pre-lithiated oxide (Li_xMO_y , $\text{M}=\text{Fe}$, Mn or Co etc.) and the anode is mostly graphite. Fig. 2.1 shows a schematic of a typical lithium ion battery.

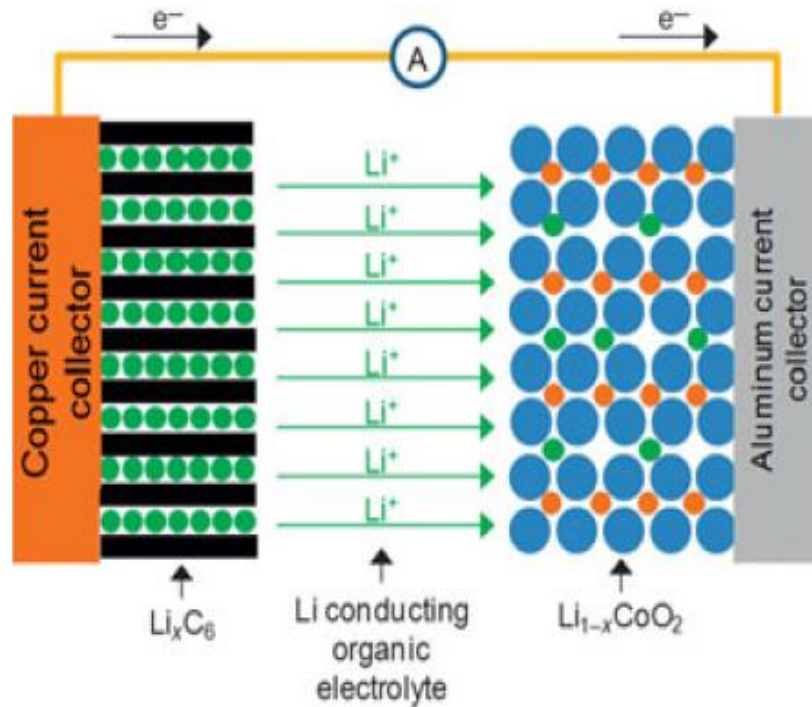
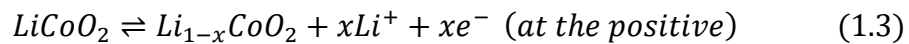
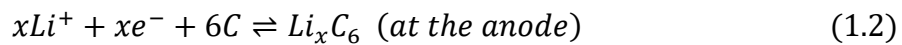


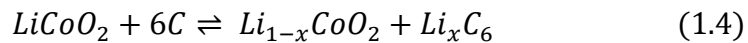
Figure 2.1. Schematic of a typical Li-ion battery [8]

The half cell reactions can be written as follows for the cell chemistry shown in the Fig.

2.1



The overall reaction can be written as



In these equations, the upper arrow shows the charging process, while the lower arrow shows the discharging process. The electrolyte used in these batteries are typically consisted of alkyl carbonate with $LiPF_6$ (lithium hexafluorophosphate salt) to provide Li ion

conduction. Most popular LIB batteries and their properties are shown in the following table 2.1.

Table 2.1 popular Li-ion battery chemistries and their properties [2]

Acronym	Cathode	Anode	Cell Voltage (V)	Energy density (Wh kg ⁻¹)
LCO	LiCoO ₂	Graphite	3.7-3.9	140
LNO	LiNiO ₂	Graphite	3.6	150
NCA	LiNi _{0.8} Co _{0.15} Al _{0.05} O ₂	Graphite	3.65	130
NMC	LiNi _x Mn _y Co _{1-x-y} O ₂	Graphite	3.8-4.0	170
LMO	LiMn ₂ O ₄	Graphite	4.0	120
LNM	LiNi _{1/2} Mn _{3/2} O ₄	Graphite	4.8	140
LFP	LiFePO ₄	Li ₄ Ti ₅ O ₁₂	2.3-2.5	100

The idea of Li ions movement between the cathode and the anode was first formulated by Armon et al. in the first part of 1970's [74]. Then this idea was further developed by Lazzari and Scrosati using a lithiated tungsten dioxide electrode and a titanium disulfide electrode. However, its voltage was limited to 2.2 V. Then the Goodenough laboratory discovered the reversibility of lithiation and delithiation properties of NaFeO₂ structure, and later LiCoO₂ was patented as the cathode material of the Sony's first ever commercial lithium ion battery. After that, J.C Hunter from Eveready laboratories discovered the similar characteristics in MnO₂.

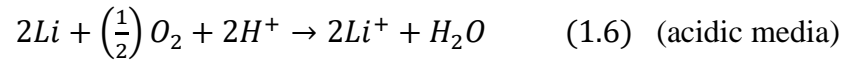
2.2.2 Li-Air batteries

Fig. 2.2 shows the operation of a Li-Air cell. During the discharge of the Li-Air cell, Li is oxidized to Li^+ at the metallic anode. An electrolyte composed of Li salt and non-aqueous solvent provides Li^+ conductance and reacts with O_2 on the cathode composed of carbon and a catalyst. Depending on the electrolyte, the reactions can be written as follows:

in an aprotic electrolyte which gives a cell potential of 3.0 V,



In an aqueous electrolyte, the fundamental reactions are



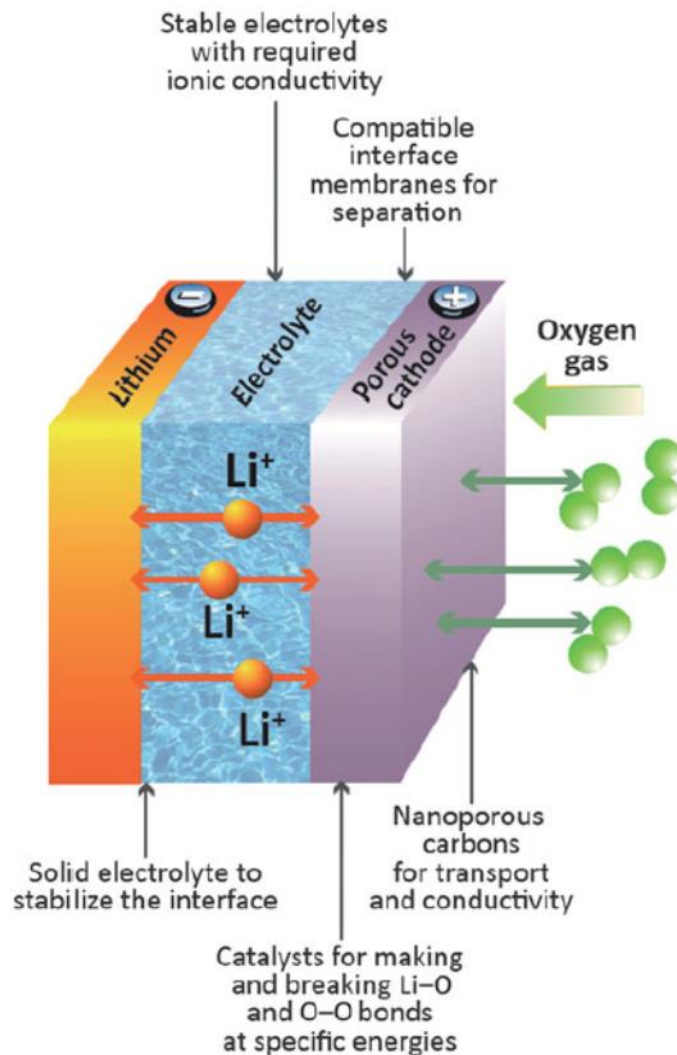


Figure 2.2 Diagram of a non-aqueous Li-Air battery [8]

2.2.3 Magnesium-sulfur batteries

Mg metal as anode material with a redox potential of -2.4 V and the specific capacity of $\sim 2200\text{ mAh g}^{-1}$, allows the cathode materials with high gravimetric capacities to assemble electrochemical cells with acceptable discharge potential and capacities. Sulfur is a good candidate to make such a cell with a practical discharge potential of $\sim 1.7\text{ V}$ and $\sim 800\text{ mAh}$

g^{-1} as demonstrated in the Ref. [75]. However, electrolyte instability with Mg metal anode presents a challenge to make Mg-S cells with good cyclability. Zhirong Zhao-kroger et al. [75] have demonstrated such a Mg-S cell and its chemistry and operation are shown in Fig. 2.3. It is interesting to see that Mg-S and Li-S cell share common features like, polysulfide formation.

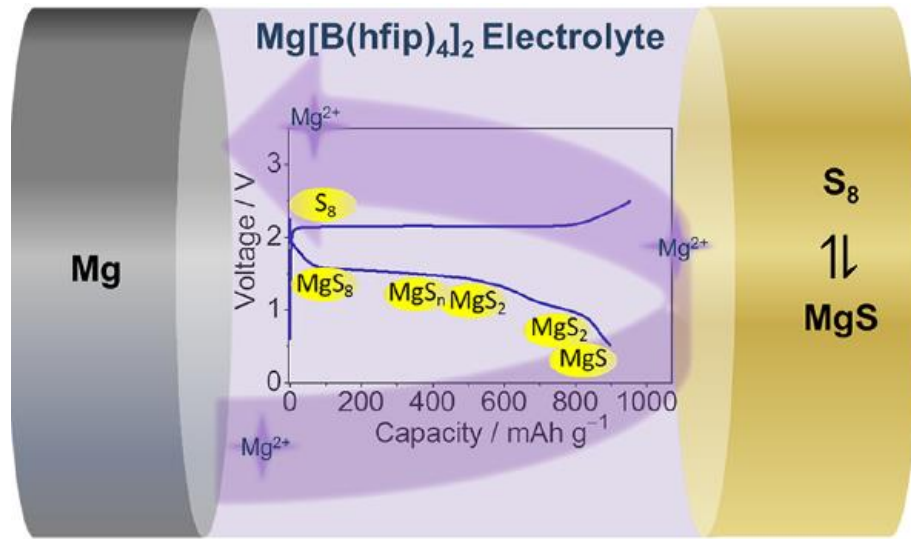


Figure 2.3 Diagram of a Mg-S battery [75]

2.2.4 Lithium-Sulfur batteries (Li-S)

Lithium-sulfur batteries are expected to be one of the viable candidates that can fulfil the energy requirements in the modern world. Further, it is the subject of the topic our research work is based on. Sulfur has a gravimetric capacity of 1672 mAh g⁻¹ versus lithium [13]. It also has an open circuit voltage of 2.53 V versus Li/Li⁺. Lithium-sulfur battery consists of sulfur/carbon composite cathode and lithium anode. Fig. 2.4 shows the schematic of a lithium sulfur battery.

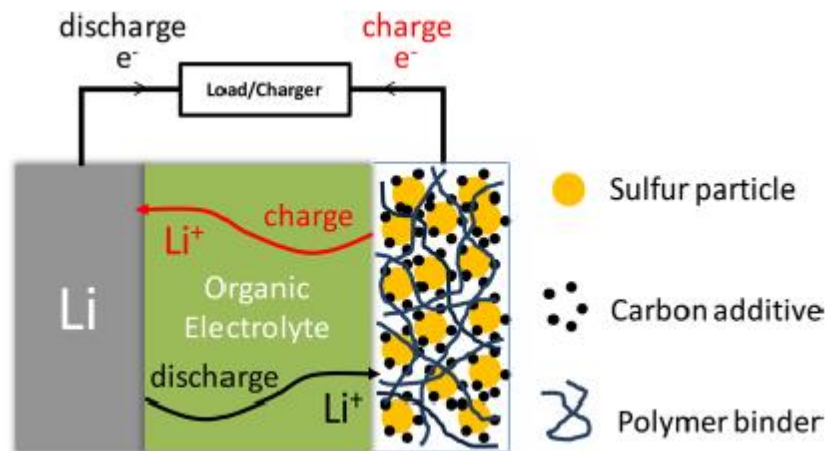


Figure 2.4. Schematic of a Li-S battery [13]

A lithium sulfur battery produces electricity through the electrochemical reaction involving sulfur and lithium forming lithium sulfide (Li_2S) as shown in the Fig. 2.5.

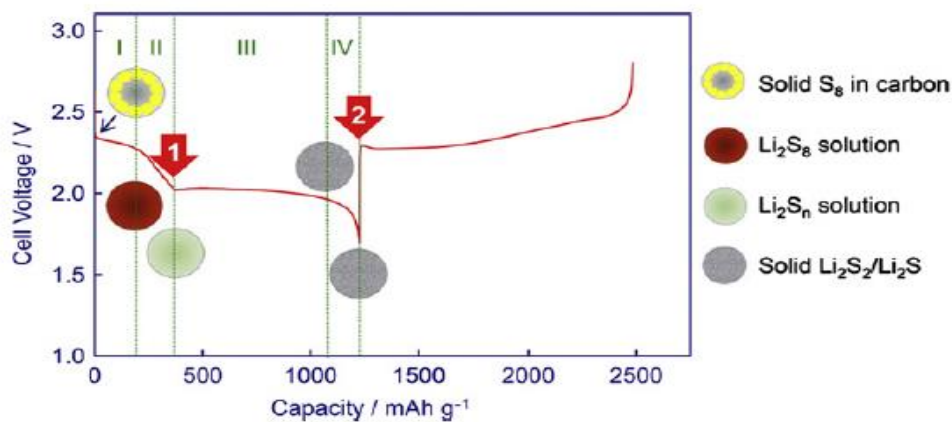
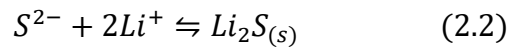
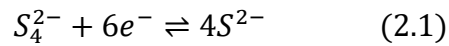
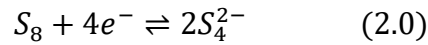


Figure 2.5. Charge and Discharge curves a typical Lithium sulfur battery [6]

However, before the Li_2S formation, lithium and sulfur forms intermediate long chain polysulfide as well. The polysulfides Li_2S_x ($3 \leq x \leq 8$) have been a major issue with

Li-S batteries as they tend to dissolve in the electrolytes which cause substantial capacity degradation during cycling. Intermediate polysulfide formation while discharging is depicted in Fig 2.5. The discharging curve has two plateaus. The voltage plateau at 2.4 V is belong to the formation of Li_2S_8 while plateau at 2.0 V belongs to formation of Li_2S . Polysulfide formation can be shown in equations as follows.



2.3 Proposed electrolytes for Li-S batteries

The challenges inhibiting the commercialization of Li-S batteries due to their well-known problems such as polysulfide dissolution, shuttling effect and self-discharge have already been addressed by many different approaches including use of meso-porous carbon structures to trap dissolved poly sulfides. Moreover, the electrolytes used in Li-S batteries are equally responsible for the development of high-performance Li-S batteries that can cycle much longer. Since the sulfur and its reduced products are non-conductive, the reduction process can only take place at the Carbon-Sulfur interface. Dissolution of polysulfides leads to exposure of unreacted sulfur to carbon so that reaction process can move forward. Therefore, dissolution of polysulfides is seen as a necessary process for proper operation of the Li-S battery [6].

The primary function of an electrolyte of the Li-S battery as in any other battery, is to transport ions between electrodes. High ionic conductivity $> 10^{-4} \text{ S cm}^{-1}$ is required over a wide temperature range of operation [76]. Electrolytes used in Li-S cells are composed of several different chemical components, namely solvents, salts and additives. Each component serves a different function to improve the durability of Li-S battery. It is important to understand each component for its function. Fig. 2.6 shows an overall picture of the electrolyte in a Li-S cell.

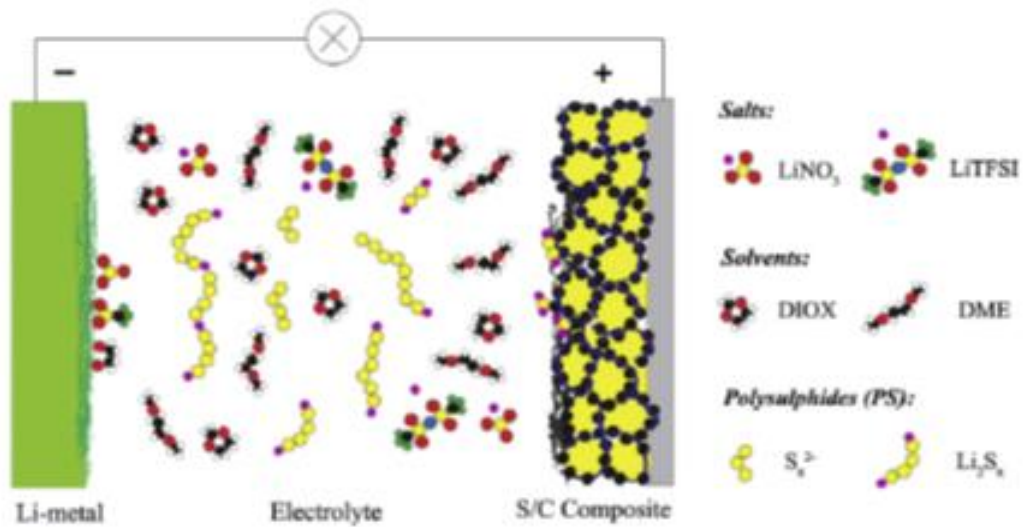


Figure 2.6. Schematic of a Li-S battery showing the actions of solvent, salt and additive [7]

Electrolytes for Li-S batteries are mainly divided into two main groups; non-aqueous-liquid electrolytes and ionic electrolytes. Liquid electrolytes can be composed of single or binary solvents. The single solvents can be either glymes, sulphones or carbonates. For High stability and ionic conductivity, binary organic solvents are predominantly used in Li-S batteries. The main motivation of using binary solvents is to obtain low viscosity,

wide temperature range and good stability with Li metal. The (9:1 v/v) of DIOX: TMF has been found to support ionic conductivity 7 times higher than LiClO₄ electrolyte.

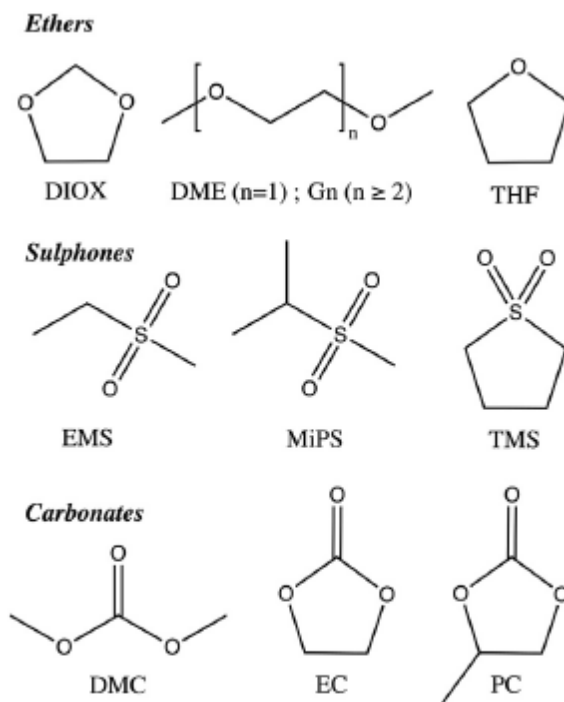


Fig. 4. Organic solvents tested for Li/S battery electrolytes.

Figure 2.7. Chemical structure of solvents used in electrolytes for Li-S batteries [7]

Lithium salts are used as the source of Li⁺ for the electrolyte with selected solvents. The most commonly used lithium salts in Li-S batteries are LiTFSI (lithium bis(trifluoromethanesulfonylimide) and LiTFS (Lithium trifluoromethanesulfonate) [77, 78] due to the high thermal stability, good compatibility with ether based solvents [79, 80] and high dissociation ability [81]. LiPF₆ and LiClO₄ electrolytes have been found not

suitable due to Lewis acid formation and safety reasons [82]. Fig. 2.8 shows the chemical structures of commonly used salts.

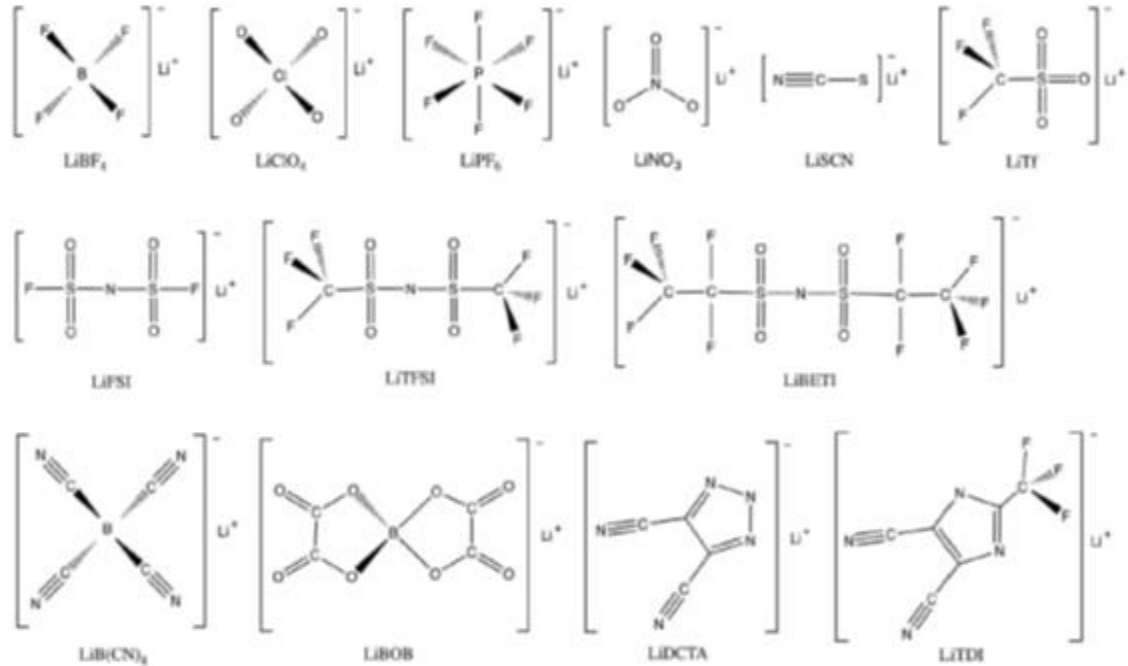


Figure 2.8. Chemical structure of salts used in electrolytes for Li-S batteries [7]

The Main purpose of using additives in Li-S cells is to form a stable SEI layer on the Lithium anode so the cell can cycle longer. LiNO_3 is the most prominent type of additive used in DIOX electrolytes to stabilize the Li metal surface [83]. The functionality of LiNO_3 has been investigated in [84] by ex-situ experiments. However, use of LiNO_3 affects the potential window of Li-S battery, because it has been found that under 1.5 V, LiNO_3 can participate in an electrochemical reaction irreversibly. It has also been found that, Polysulfide itself can also play the role of an additive in Li-S batteries [79, 85, 86]. By adding polysulfides 5 % or less into the electrolyte, it has been found that, leaking of

polysulfides from the cathode can be mitigated. Fig. 2.9 demonstrates the function of additives in Li-S cells on forming the SEI layer.

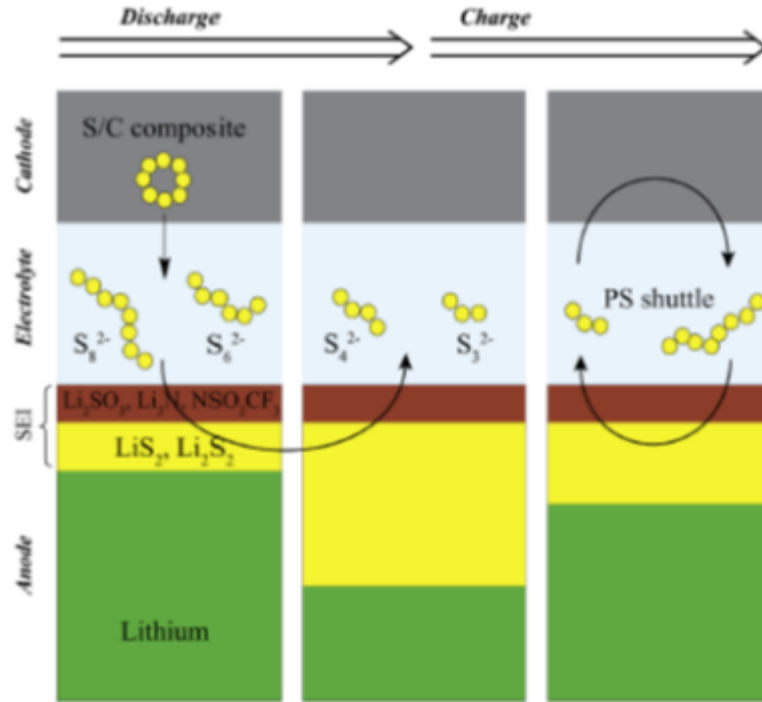


Figure 2.9. Schematic of polysulfide dissolution, SEI formation [7]

Ionic electrolytes attracted the researcher's attention due to their non-volatile and non-flammable nature. Use of ionic liquids as the electrolyte will be safer than liquid electrolytes which pose problems such as leaking and degassing. Ionic electrolyte provides high ion conductivity, large electrochemical stability window and good solubility. However, the problem with ionic electrolytes is their high viscosity which poses problems when used in Li-S batteries in addition to their higher cost.

2.4 Challenges associated with developing a high capacity sulfur cathode

Despite the promising electrochemical characteristic of Li-S cells, producing a commercial Li-S cell is still a challenge. Those problems have been well understood by the scientific community and studied. Among them, lithium polysulfide dissolution in the electrolytes is the main cause of capacity degradation in substantial cycles. Lithium polysulfides Li_2S_x ($8 \leq x \leq 3$) intermediate long chain products which can dissolve in the liquid electrolytes known to use to fabricate Li-S batteries. During the discharging process, insoluble Li_2S_2 and Li_2S are formed at the end of the redox reaction in the cathode. Poor electrical conducting properties of sulfur and its intermediates formed along with the structural changes lead to sluggishness for the reaction kinetics, therefore demonstrate poor rate capabilities in a practical Li-S battery. Fig 2.10 shows a mechanism of polysulfide formation when discharging the Li-S battery.

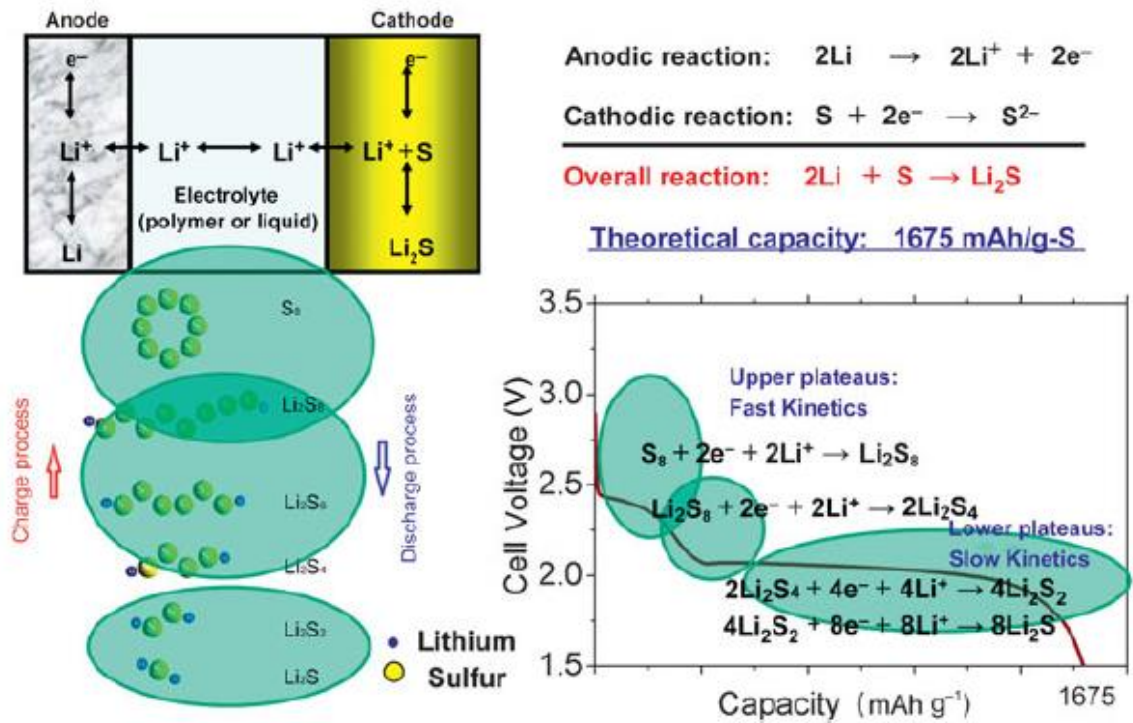


Figure 2.10 Schematics of a Li-S cell and its electrochemical reactions [8]

The dissolved polysulfides are then participate in a phenomenon known as polysulfide shuttling which is a process of migrating dissolved polysulfide chains between cathode and anode during the discharge and charge cycles. Fig. 2.11 depicts the polysulfide shuttling process schematically. The shuttling of polysulfides allows side reactions on the Li anode and it can lead to low utilization of Li in substantial cycles, hence poor cycle life.

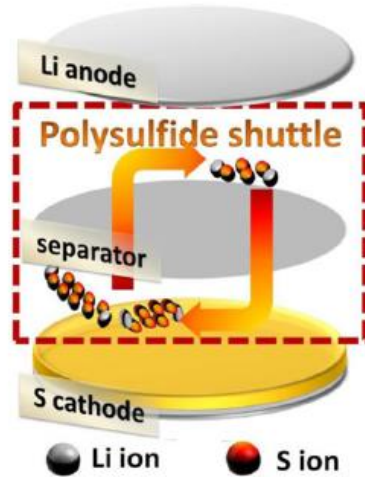


Figure 2.11 Illustration of the shuttle mechanism of a Li-S battery [13]

The third main reason for limited cycle-ability of Li-S battery with metal lithium metal is due to the non-uniform Li-deposition on the anode. These depositions are in two different types. First one is due to the dendrite formation and second is due to the formation of lithium crystals. Dendrites are responsible for short circuiting the cathode and anode while Li-crystal can chemically active with electrolyte due to their high surface area. Fig. 2.12 depicts the dendrite formation process.

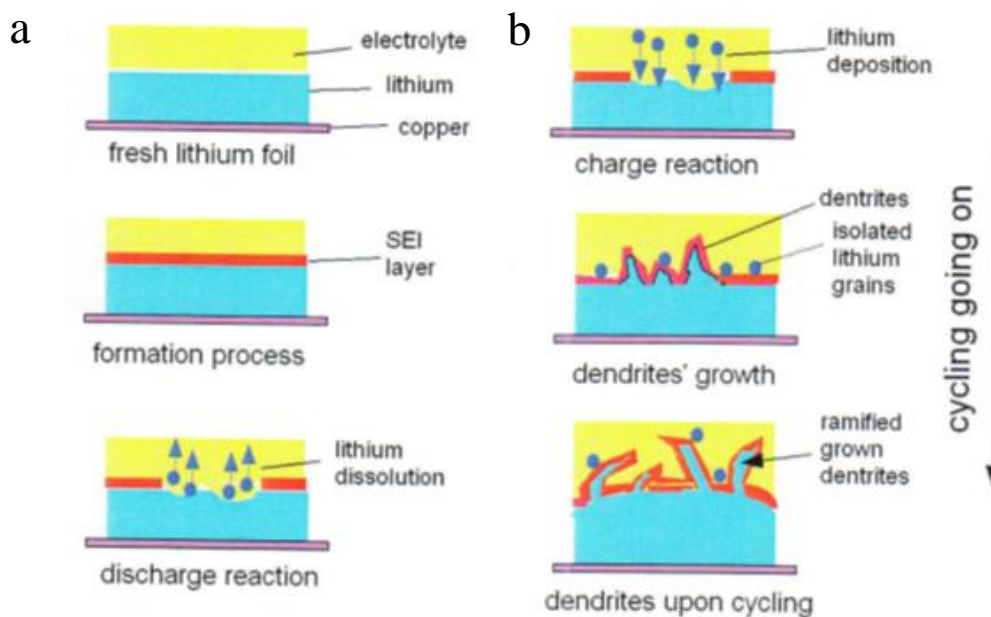


Figure 2.12 Illustration of dendrite formation process (a) lithium dissolution
(b) lithium deposition [2]

2.5 State of the art α -MoO₃ anode material for high capacity Li-S batteries

When Li-S full cells are considered for EV applications, voltage window becomes a major factor in addition to the high charge density as it demands light weight, high energy density battery packs. Si, Sn and graphite have the delithiation potential of 0.5 V, 0.3 V and 0.05 V respectively vs Li⁺/Li [67, 87, 88]. α -MoO₃ demonstrate 0.2 V lithiation voltage [89] which would give very good open circuit voltage when assembled with sulfur in a Li-S battery. The layered structure of α -MoO₃ shows the promise to be used in energy storage systems. Some of the recent work on MoO₃ related to energy storage are discussed in Ref [9, 90]. In [91], α -MoO₃ is synthesized via vapor transport technique and in [92] 1-D α -MoO₃ is synthesized with aqueous solution process starting with (Na₂MoO₄·2H₂O). MoO₃ can also show pseudo-capacitive nature in thin films. In Ref [93], they have shown that the

crystalline MoO_3 has higher gravimetric capacitance compared to amorphous MoO_3 . The low expansion of $\alpha\text{-MoO}_3$ upon lithiation makes it more suitable for Li-S full cell. Further, it eliminates any safety issue associated with Li batteries. One of the major issues with MoO_3 is its poor electrical conductivity. The electrical conductivity of MoO_3 can be improved by mixing with carbon. Ref [94] has demonstrated a carbon- MoO_3 electrode with electrical conductivity enhancements. Nanowire morphology of MoO_3 also is also believed to improve the charge capacity retention. Vertically grown nanowire electrode architecture has been investigated by [95] for $\text{MoO}_{(3-x)}$. In their work, the stable capacity of $\text{MoO}_{(3-x)}$ structure as an anode in Li-ion cell has been shown due to its accommodation for Li^+ with low volume expansion. Li_2MoO_4 has been tested as a pre-lithiated anode material for Li-ion batteries. But Li_2MoO_4 is not suitable for Li-S batteries due to its Mo (+6) oxidation state [96].

The $\alpha\text{-MoO}_3$ yield from above methods of however, is very small, to be able to make high energy density which requires high mass loading. Thus, research must be focused on improving the $\alpha\text{-MoO}_3$ amount as well as ways of pre-lithiating it.

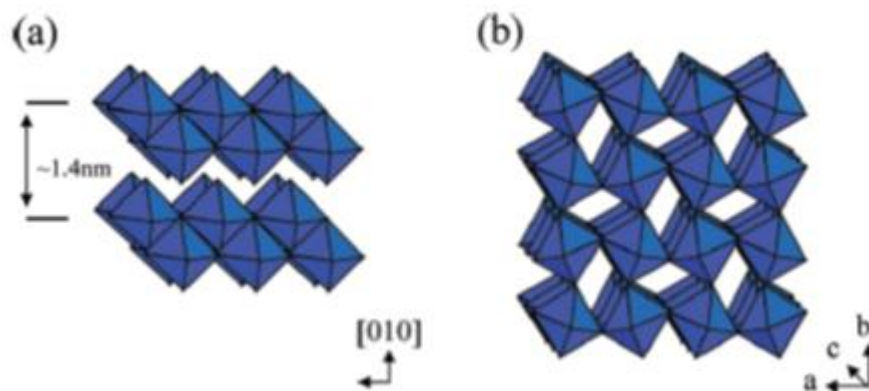


Figure 2.13. (a) Thermodynamically stable orthorhombic α -MoO₃

(b) meta stable β -MoO₃ [11]

The work done in this dissertation uses α -MoO₃ which were synthesized using hot wire CVD technique (HWCVD) to be electrochemically pre-lithiated and assembled with optimized sulfur cathode for making Li-S full cell. Further, the yield of α -MoO₃ synthesis is further improved by introducing novel method to synthesis α -MoO₃ using H₂ reduction technique with similar material characteristics as in α -MoO₃ from HWCVD technique, but with improved electrochemical performance in a practical Li-S full cell.

2.6 Instruments of material and electrochemical characterization

2.6.1 Material characterization

2.6.1.1 X-ray diffraction (XRD) technique

X-ray Diffractometer (Bruker D8) was used to analyze crystalline structure MoO₃. The XRD spectrum was measured with in the 2θ range of 10° - 80° . Copper is target material for single-crystal diffraction, with CuK α radiation = 1.5418 Å. These X-rays are collimated and directed onto the sample. The XRD analysis was performed in both *insitu* and *exsitu*

techniques. *In-situ* XRD cell was used for obtaining the XRD spectrum while electrochemically lithiating α -MoO₃. *Ex-situ* XRD analysis was done using powder technique to observe the crystalline structure of synthesized MoO₃.

2.6.1.2 Scanning electron microscope (SEM) imaging

TESCAN thermionic emission scanning microscope was used to image the surface and cross sections of sulfur cathode. Field emission scanning microscope was used for mapping the material composition of TiO₂ coated sulfur cathodes using X-ray dispersive spectroscopy (EDAX). Semiconducting materials such as TiO₂ was sputtered with thin layer of gold for better image quality under the SEM.

2.6.1.3 X-ray photo electron spectroscopy (XPS) analysis

In this work, XPS analysis was done to investigate the bonding nature of polysulfides trapped in the TiO₂ particle barrier on the sulfur cathode. XPS spectrometer which used was VG Scientific MultiLab 3000 which Al/Mg has a X-ray twin source (1253.6 eV (MgK α), 1486.6 eV (AlK α))

2.6.1.4 Thermogravimetric analysis (TGA)

The mass loading of cathode and anode was measured and calculated using *Q600 scanning* differential thermogravimetry (SDT) analyzer. The Q600 SDT analyzer has a maximum temperature of 1500 °C. Sulfur mass loading was calculated using Q600 SDT analyzer with Air supply. Sulfur is evaporated as SO₂ in the temperature range of 200 °C - 400 °C, hence the mass loading can be calculated by the weight loss.

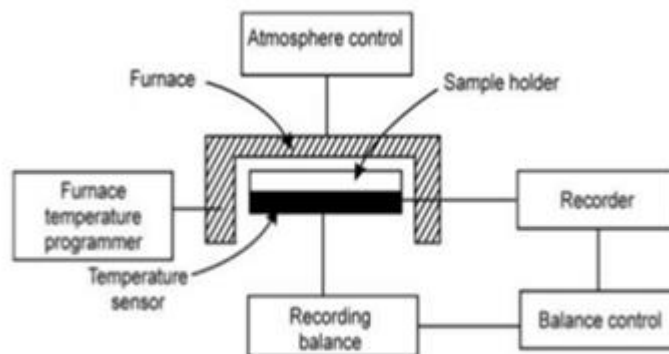


Figure 2.14. Cross section of TGA instrument

2.6.2 Electrochemical characterization

2.6.2.1 Galvanostatic electrochemical characterization

In galvanostatic electrochemical analysis, the voltage is measured while keeping the current constant. Typically, capacity is measured using galvanostats. In this work, Arbin 16 channel battery tester was used for capacity measurements, C-rate measurements and cell cycling. The Arbin battery tester is programmable for the different voltage and current requirements within 5 V and 10 A limits. All experiments were carried out in room temperature at 25 °C.

2.6.2.2 Potentiostatic electrochemical characterization

Potentiostats are one of the key instruments used in electrochemical analysis. In a potentiostat, voltage is the controlled variable, while current is the measured variable. In this work, biologic SP200 potentiostat was used to perform cyclic voltammetry (CV) and

electrochemical impedance spectroscopy (EIS) analysis. The cyclic voltammetry was performed in the range of 2.8 V- 1.5 V for the cathode and 2.8 V – 0 V for the anode. The frequency range used for EIS was 1 GHz – 1 mHz.

CHAPTER 03

MESO-POROUS TiO₂ COATED SULFUR CATHODE

3.1 Scope

The problems associated with sulfur cathode and the mechanism of polysulfide dissolution has been mentioned in Chapter 1. Also, a body of research done elsewhere on developing sulfur cathodes has also been mentioned in Chapter 1. Therefore, this chapter is structured in such a way that, the application of anatase TiO₂ coating on sulfur cathode to trap soluble polysulfides is discussed at the beginning. Then methods of fabricating carbon electrodes are described to improve the electrical conductivity of sulfur cathode. Finally, the electrochemical and materials analysis of anatase titania coated sulfur cathodes are presented.

3.2 Introduction

The use of TiO₂ has been successfully utilized in sulfur cathodes by other researches to improve the performance of Li-S batteries. In the first method, sulfur cathodes were made by simply mixing titania particles with sulfur/carbon composites [97-99]. In the second method, sulfur was first coated with titania followed by carbonization [46, 53, 100]. In the third method, titania nanoparticles

have been coated on a polymer separator, forming an effective polysulfide adsorbing barrier [101]. All these methods have one common feature of mixing titania with carbon to enhance the electrical conductivity of the bulk electrodes. However, the capacity retention in any of these methods is not very attractive.

3.3 Mesoporous TiO₂ coating as a polysulfide adsorbing agent

TiO₂ has two main structures; rutile and anatase. TiO₂ has drawn the attention of many research fields such as optics, semiconductors and energy storage etc. TiO₂ has three naturally occurring crystal structures Rutile (tetragonal, a=b=4.584 Å, c=2.953 Å), brookite (rhombohedral, a=5.436 Å, b=1.166 Å, c=5.135 Å) and anatase (tetrahedral a=b=3.782 Å). TiO₂ is mainly a semiconducting material and it has different applications as catalyst, photoelectrochemical material, bio medical treatments and in energy storages. In this work, the anatase phase of TiO₂ is used for trapping soluble polysulfides. The Anatase titania has a crystal structure of 3D network formed by the stacking of 1D zigzag chains consisting of distorted edge sharing TiO₂ [102]. Rutile and Anatase has been extensively studied in their application as they have studied in their surface science techniques. The main object of this sub section is to describe the properties of Anatase surface which is being used in our work to trap soluble polysulfides. Defect of the TiO₂ can be line defect or point defect. The point defects on TiO₂ surface has been researched by many researchers. Their occurrence can be due to Ti-O bond dissociation on the surface and thermal effect.

TiO₂ surface has been studied extensively for adsorption of different elements. In this work however, we are interested in adsorption of sulfur or polysulfides links to oxygen defect sites. Elemental sulfur (S_n, n≥2) adsorption has been studied by [4]. Bechtold and

co-worker [103] has investigated the polysulfide adsorption by dosing sulfur electrochemically. In their finding polysulfides adsorbed at fivefold coordinated Ti atoms (Fig. 3.3). This is shown in Fig. 3.1 where sulfur atoms are visible as large, white spots situated along the bright rows of empty-states of STM image. The adsorption of Polysulfides onto oxygen vacancies are confirmed by the disappearance of the defect-related band gap state in valance band photoemission spectra [104]. The adsorption properties for $S_n (n \geq 2)$ is the motivation for us to use TiO_2 as a polysulfide trapping barrier via surface adsorptions of polysulfides.

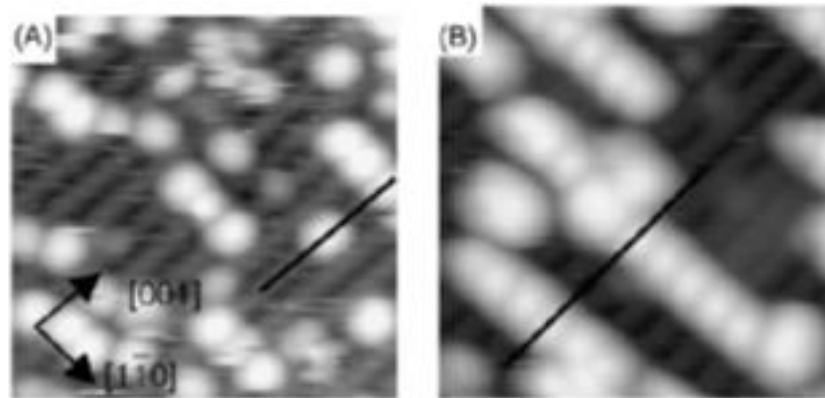


Figure 3.1. STM image of sulfur adsorbed on TiO_2 (110). S atoms are located at the bright spots [4]

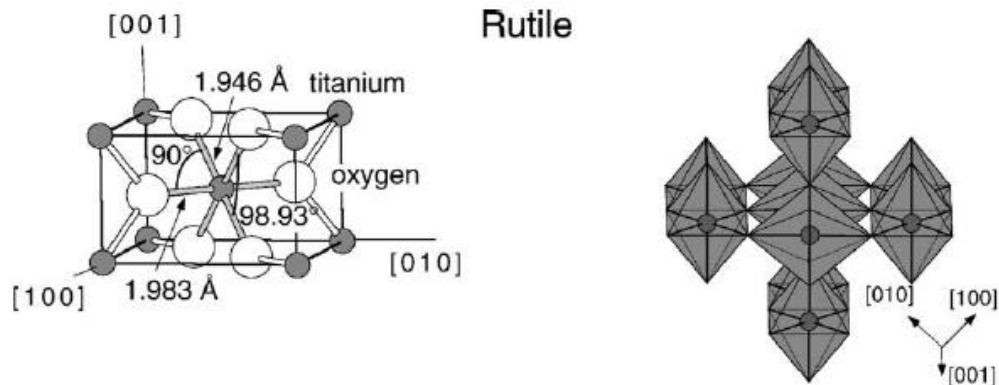


Figure 3.2. Unit cell of Rutile TiO_2 [4]

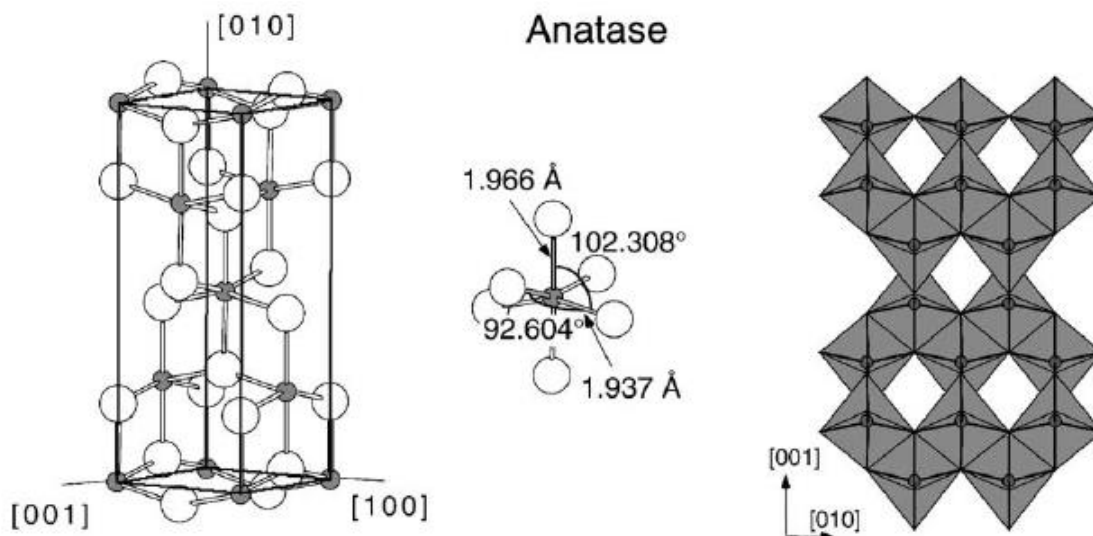


Figure 3.3. Unit cell of Anatase phase [4]

3.4 Material synthesis for sulfur/carbon electrodes

In this work, we attempted to fabricate sulfur cathodes using two different carbon matrices. In one method we used carbonized micro fiber network to host sulfur. Second method used activated carbon as sulfur hosting matrix. Both methods will be discussed in detail below.

3.4.1 Carbonized microfiber (CMF) based sulfur cathode

Micro fiber synthesis using electro-spin technique has been very well established in numerous fields. Electro-spin technique is commonly used in fields such as textile industry. In our electro-spin technique, Poly-acrylonitrile is used as the polymer for synthesizing the fibers. Fibers were extruded from a syringe needle using an electric potential of 15 kV. The distance from anode to cathode was maintained at ~30 cm. When synthesizing the fibers, the flow rate was maintained between 0.7 ml min^{-1} to 1 ml min^{-1} . Fibers were collected

onto a negatively charged rotating drum which made of disposed laser printer cartridge as shown in Fig. 3.4a. The diagram of the experimental setup is shown in Fig. 3.5.

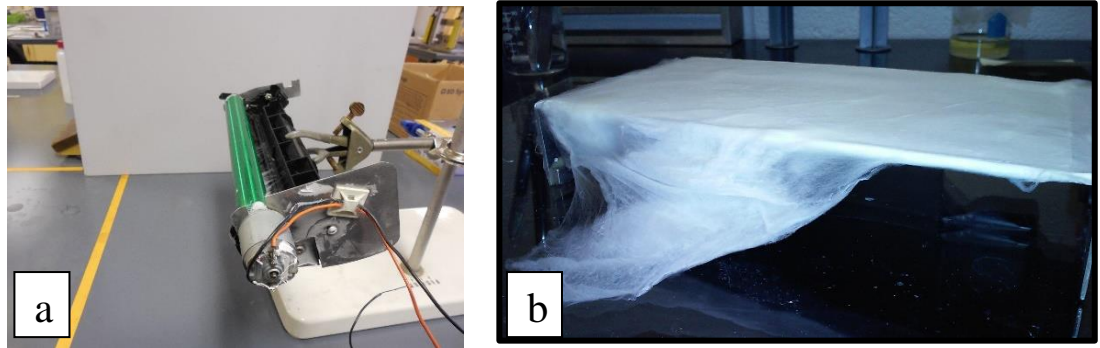


Figure 3.4. (a) fiber collector drum (b) synthesized poly-acrylonitrile fiber mat

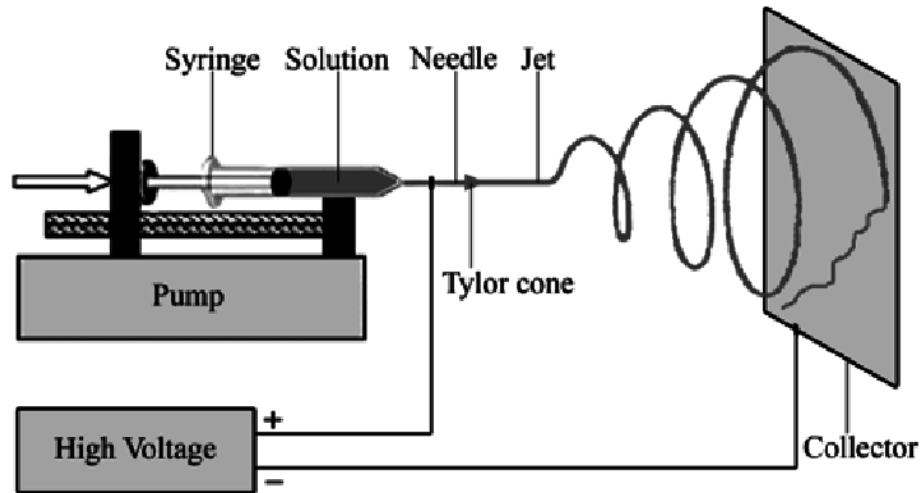


Figure 3.5. Electrospinning setup

The electro-spun fibers are deposited as a free-standing cloth (Fig 3.4b). The non-conducting cloth however needs to be carbonized in order to make it electrically conductive. The carbonization process is done in a nitrogen environment. In the first stage of the process, the fiber mat was stabilized just by heating at 200 °C in the normal atmosphere for about 3 hours to break-down the OH bonds in the carbon structure. Next, the dehydrated fiber structure is fully burned at 900 °C in a nitrogen environment. This process is maintained for about 2 hours. The temperature must be ramped slowly to prevent shrinking and warping of the fiber mat.

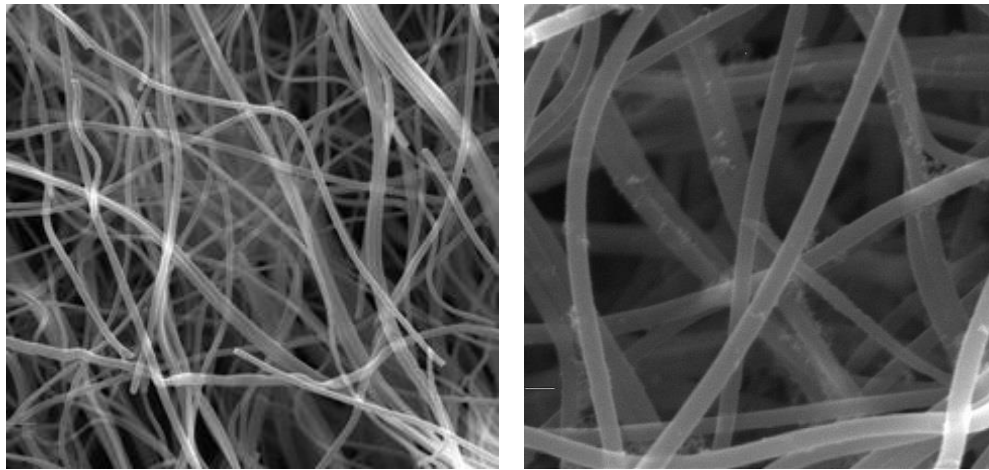


Figure 3.6. SEM images of the carbonized microfibers

After carbonization of the fibers, the fiber mat was cut into $1\text{ cm} \times 1\text{ cm}$ square pieces and 3- 4 mg of sulfur was thermally infused into the fiber network. The low melting temperature of sulfur ($115\text{ }^{\circ}\text{C}$) was beneficial in this process. The fiber network was found to show obvious capillary action. Simply, a known mass of sulfur was first melted, and the carbonized mat was dipped in the molten sulfur so that sulfur can easily infuse into the carbon network. This allowed the establishment of an excellent electrical conductivity of the sulfur-carbon electrode. Finally, the entire sulfur/carbon fiber electrode was dip coated in titania in ethanol to coat TiO_2 .

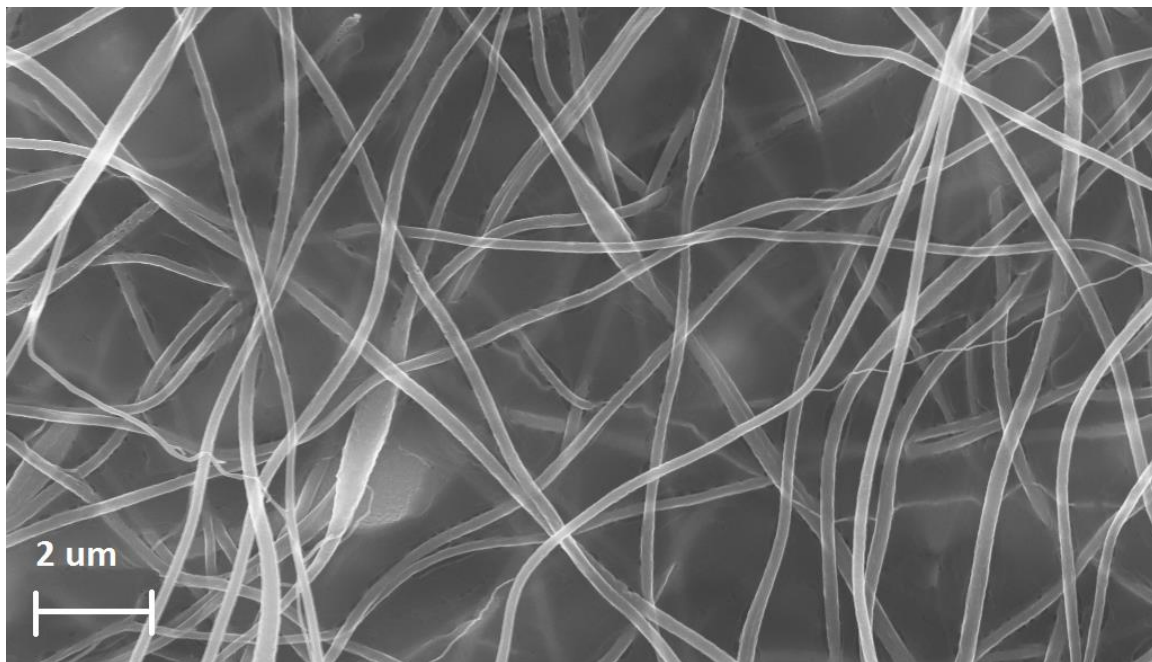


Figure 3.7. SEM image of the sulfur diffused carbonized fiber electrode

3.4.2 Activated carbon (ACP) based sulfur cathode



Figure 3.8. Free standing electrode made of activated carbon

The electrode is prepared by ball milling ACP (derived from agricultural waste) with 10 ml of 60% PVDF (Polyvinylidene fluoride) in NMP (N-Methyl-2-pyrrolidone) solvent for 12 hours. Then the ACP slurry is poured onto a clean glass surface to and let it dry at room temperature to form a free-standing ACP sheet Fig. 3.8. After that, sulfur (3-4 mg) is melted on a hotplate at 130 °C and is impregnated into ACP free standing carbon structures by pressing them onto the melted sulfur. In the third step, ACP electrodes are coated with 200 nm titania paste by dipping the electrodes in titania suspension in ethanol, followed by air drying for 24 hours. A part of the back surface of the titania coating is scratched-off to expose the interior of the carbon/sulfur electrode (bridging) in order to make better electrical contact with the current collector.

3.5 Coin cell assembling for electrochemical testing

Titania coated sulfur electrodes made of either CMF or ACP are pressed against a carbon black pellet forming the electrical bridge. The carbon black pellet is made by mixing 20

mg of acetylene carbon black and 20 ml of PTFE (Polytetrafluoroethylene). Next, it is placed on a stainless-steel mesh with a diameter of 15 mm and pressed under ~300 kg of pressure (using a hydraulic press) to mount the entire assembly on the current collector. The thickness of the carbon black pellet is reduced to about 0.1-0.2 mm after pressing. Then they were assembled in a CR2032 coin cell with pure lithium metal as the anode, inside an argon-filled glove box. Celgard 3401 polymer separator (~30 μm thick) is placed between the electrodes. The composition of the electrolyte used in this work is 1:1 ratio of 1,2-Dimethoxyethane (DME Sigma Aldrich) and 1,3-Dioxolane (DOL Sigma Aldrich) in 1 M Bis(trifluoromethane)sulfonimide lithium salt (LiTFSI) and 1% wt of LiNO_3 for a total of 0.5 ml of electrolyte. The ionic conductivity of the electrolyte is ~14.7 mS/cm at 25 $^\circ\text{C}$. LiNO_3 is widely used as an additive in the electrolyte to form a protective film on the lithium anode. Fig. 3.9 represents the side view of the cell including the SEM image of the titania coating, and the pore width distribution for anatase titania powder measured by BET technique. The mean pore width is found to be 40 nm which is mesoporous. The size of titania particles used in this experiment is around 200 nm. When the electrode is fabricated, we found that the particle coating maintains the meso-porosity.

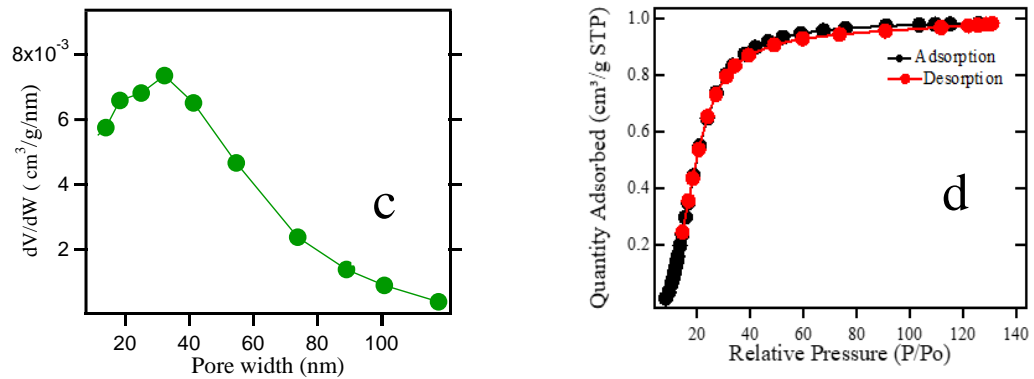
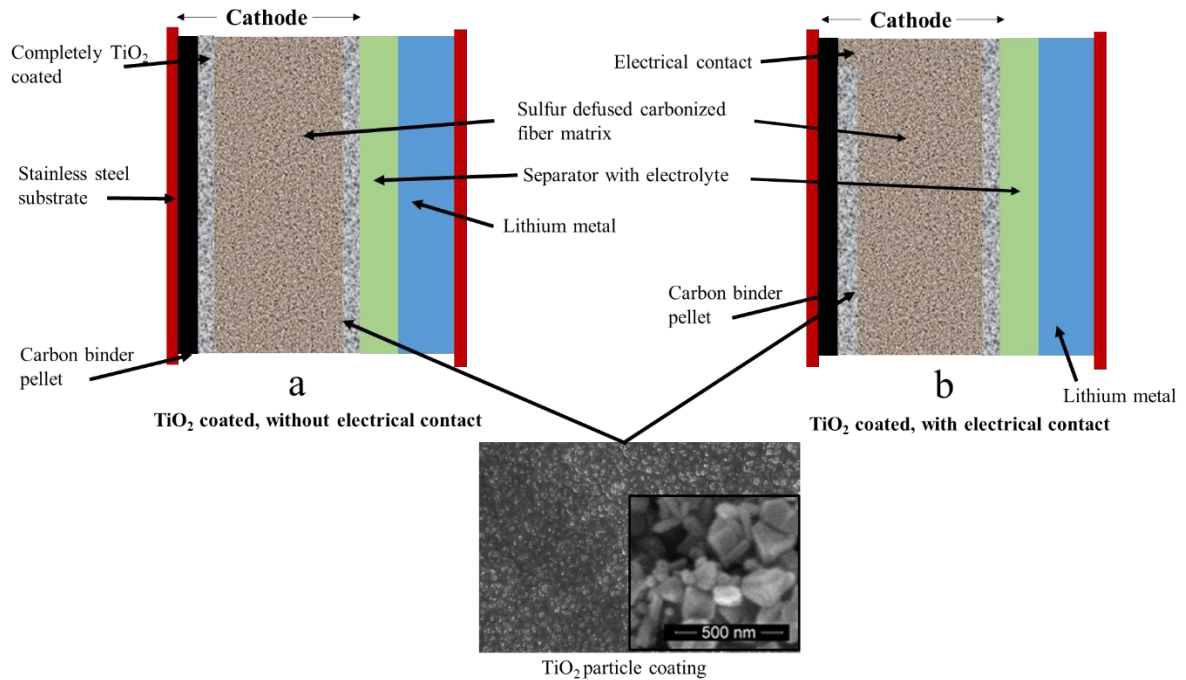


Figure 3.9. Schematic diagram of the titania coated electrode (a) without electrical contact (b) with electrical contact for ACP supported sulfur cathode in a Li-S cell. The SEM images of the sulfur support and the titania coating and (c) pore width distribution (d) N₂ adsorption–desorption isotherms for anatase titania powder are also shown

3.6 Electrochemical and structural analysis

The cells were cycled between 1.5 and 2.8 V versus Li/Li⁺ in galvanostatic mode using 16 channel Arbin battery test system. Cyclic voltammetry (CV) was performed at a scan rate of 0.3 V in the range of 1.5 to 2.8 V using the biologic sp-200 electrochemical system. AC impedance (EIS) of the cell was measured using the same electrochemical system over the 1 mHz to 1 MHz range. Both CV and EIS measurements were conducted using two-electrode configuration with lithium as both the counter electrode and the reference electrode. All performances were carried out at 25 °C.

Characterization: The ionic conductivity was measured by a biologic sp-200 system. The electrode surface morphology before and after cycling was characterized by a TESCAN thermionic emission scanning electron microscope. X-ray photoelectron spectroscopy (VG scientific-MultiLab 3000) was employed to detect the chemical composition of the cathode. All XPS spectra were fitted with Gaussian–Lorentzian functions and a Shirley and linear type background. 2P_{3/2} 2P_{1/2} peaks were fitted using Lorentzian function. The binding energy values were all calibrated using Carbon 1S 284.5 eV. Samples for SEM and XPS characterization were prepared by disassembling cells and rinsing with 1,2-Dimethoxyethane, 1,3-Dioxolane. TGA studies were done by Thermogravimetric analyzer TA 2050

3.7 Results and discussion

Performance of the sulfur cathode is tested against lithium metal as the anode in a coin cell configuration over the voltage range of 2.8–1.5 V using an Arbin battery tester. The sulfur cathodes made of CMF demonstrated poorer electrochemical performances compared to the sulfur cathodes made of ACP. The electrochemical performances of CMF based sulfur cathodes are shown in the Appendix 1.

The electrochemical performances of an uncoated sulfur cathode and a mesoporous titania coated cathode made using ACP are shown in Fig. 3.10. The areal sulfur loading is 2.65 mg-cm⁻² and mass of titania coating is approximately 1.5 mg-cm⁻². In all cases of Fig 3.10b, discharge curves showed two discharge plateaus at 2.4 and 2.0 V. The sudden drop of voltage in Fig. 3.10a from 2.6 V to 2.4 V is due to the polarization and IR drop of electrodes and electrolyte. The plateau at 2.4 V is believed to be due to the reduction of S₈ to high-order soluble lithium polysulfides (e.g. Li₂S₄), and the plateau at 2.0 V is due to further reduction of Li₂S₄ into insoluble Li₂S. The uncoated sulfur electrode shows rapid decay of gravimetric discharge capacity within the first 20 cycles (Fig. 3.10a). There, titania coated electrode shown in purple color however, exhibited stable discharge capacity in excess of 900 mAh g⁻¹ even after the 100th cycle.

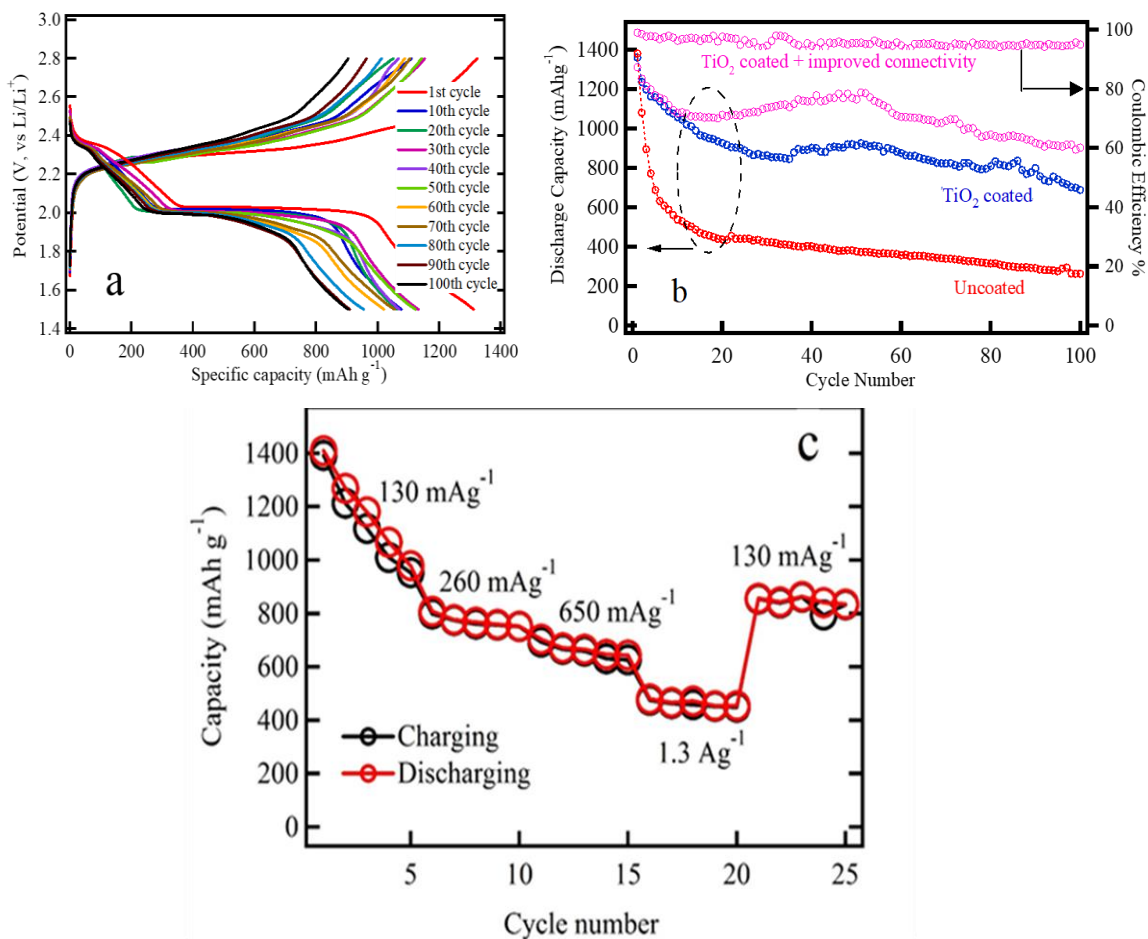


Figure 3.10. Gravimetric capacity results of ACP based sulfur electrodes; (a) potential vs. specific capacity curves of optimized ACP based titania coated sulfur cathode, (b) comparison of the discharge capacity of various ACP based cathodes; (i) titania coated sulfur cathode with (purple) and without (blue) improved electrical connection to the current collector and (ii) uncoated electrodes (red); left axis represent the discharge capacity and the right axis represents the coulombic efficiency for the optimized sulfur cathode (c) rate capability performances of ACP based titania coated sulfur electrode with improved electrical connection.

The influence of proper electrical connection to the conductive matrix of the electrode is investigated by comparing three different activated carbon electrode systems: (i) uncoated, (ii) titania coated with poor electrical connectivity, and (iii) titania coated with improved electrical connectivity (electrical bridging) as shown in Fig. 3.11. Experiments were carried out at C/3 discharge and charge rate. Synthesis of activated carbon is described in the supplementary document. A properly working sulfur electrode has two voltage plateaus at ~ 2.4 V (formation of Li_2S_x polysulfides) and ~ 2.0 V (formation of Li_2S and Li_2S_2). This is an indication that Li^+ transport has not been mitigated by the titania particle barrier. A stable discharge capacity of about 980 mAh g^{-1} for 100 cycles has been achieved for the titania coated ACP supported sulfur electrode with improved electrical conductivity. In contrast, the titania coated ACP supported sulfur electrode with poor electrical connectivity shows lower discharge capacity of $\sim 700 \text{ mAh g}^{-1}$ after 100 cycles while the ACP supported sulfur electrode without a coating layer shows discharge capacity of only 265 mAh g^{-1} at 100th cycle. The idea of coating the back side of the electrode with mesoporous titania is to prevent any leak of soluble polysulfides into the electrolytes when the battery is at idle between cycles.

In this work the electrical conductivity between current collector and active material is established through an electrical bridging technique (Fig. 3.11c). Its effect is further analyzed by 2- probe impedance tests as shown in Fig. 3.11. The electrical contacts were made to the current collector and the titania coating layer on the other side. It is found that the dc resistance for the electrically bridged cathode is 127.88Ω in comparison to the dc resistance value of 1283.63Ω for the electrode with titania coating on both sides. This is

a significant improvement in the net electrical resistance due to the electrical bridging leading to a high discharge capacity as seen in Fig. 3.10b.

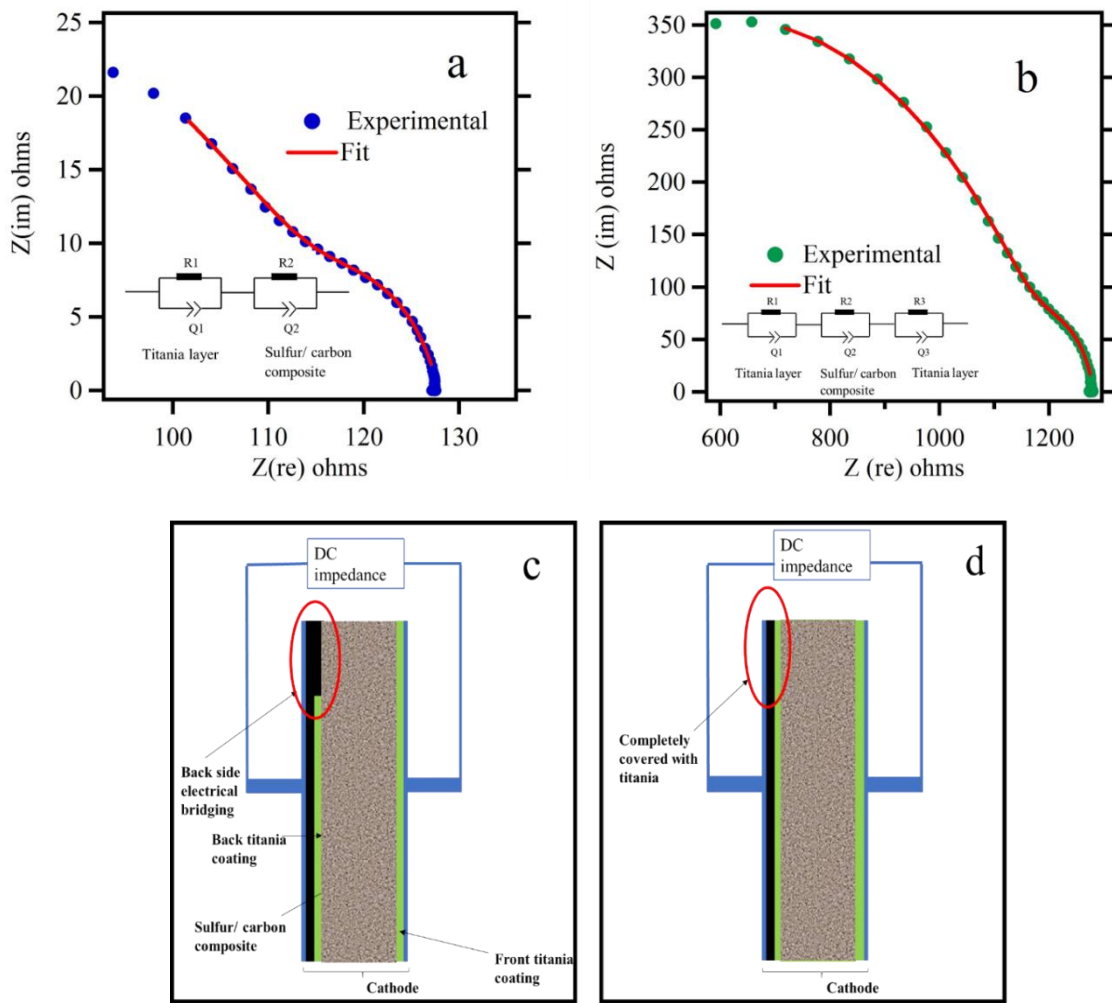


Figure 3.11. Electrical conductivity measurements of the cathode material: Nyquist plots for titania coated sulfur electrode (a) with part of the backside uncoated (exposed) (b) both sides coated with titania. The inserts show the equivalent circuit network utilized for impedance analysis. (c) and (d) show the side view of the titania coated electrode with provisions for electrical bridging and the electrode with both sides completely coated with titania respectively.

In order to investigate high-power performance of the titania coated sulfur electrode with proper electrical contact, rate capability was studied in the voltage range of 2.8–1.5 V with different current densities as shown in Fig. 3.10c. Five initial formation cycles have been shown at 130 mA g^{-1} current density followed by 5 cycles each at 260 mA g^{-1} , 650 mA g^{-1} , and 1.3 A g^{-1} current densities. It shows that discharge capacities at 130 mA g^{-1} , 260 mA g^{-1} , 650 mA g^{-1} , and 1.3 A g^{-1} are approximately 1000, 800, 700, and 450 mAh g^{-1} , respectively. When the current density is reduced back to 130 mA g^{-1} after the rate performance testing, the sulfur cathode can retain the discharge capacity close to the formerly measured value of 900 mAh g^{-1} , indicating its good reversibility and high rate capability and demonstrating the recovery of the titania coated sulfur cathode after subjecting it to different charge-discharge rates.

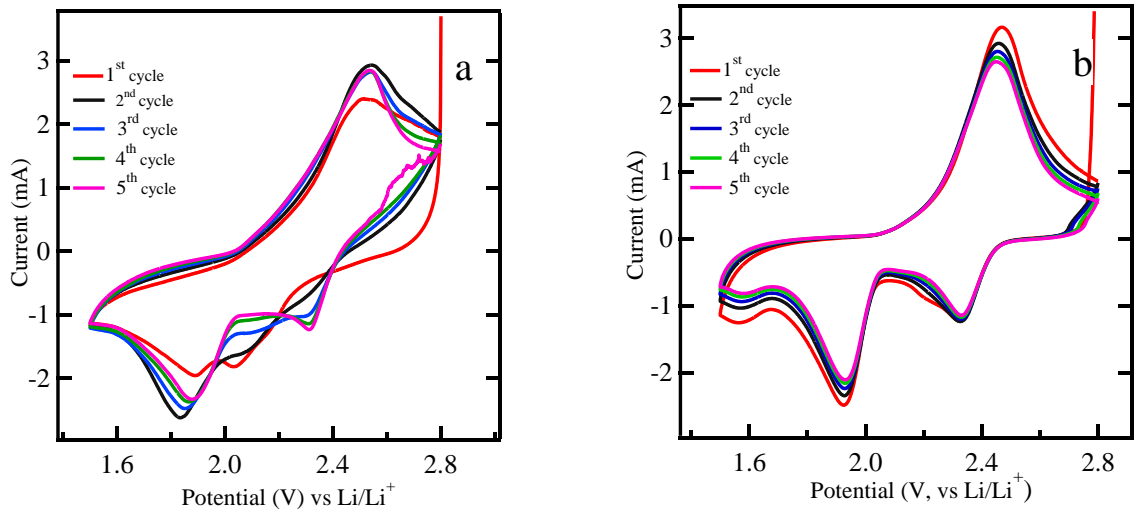


Figure 3.12. Cyclic voltammetry measurement of (a) uncoated sulfur electrode (b) titania coated sulfur electrode (ACP based) at the voltage range 2.8-1.5 V at scan rate of 0.3 mVs⁻¹

Next, cyclic voltammetry (CV) was carried out for the ACP based sulfur impregnated electrodes without and with titania coating as shown in Fig. 3.12 within 2.8 V and 1.5 V range at 0.3 mV s^{-1} rate. The lower end potential is chosen to be 1.5 V since LiNO_3 additive tends to be reduced irreversibly at the voltages below 1.5 V [105]. CV measurements are carried out for up to 5 cycles and both electrodes showed the complete two step redox reactions with two reduction peaks appearing at around 2.3 and 2.0 V and one oxidation peak at ~ 2.4 V. The peak at ~ 2.3 V is ascribed to the reduction of sulfur to form the higher order lithium polysulfides (Li_2S_n , $n > 4$), and the peak at ~ 2.0 V corresponds to further reduction of these lithium polysulfides to lower order lithium polysulfides (Li_2S_n , $n < 4$) including Li_2S_2 and Li_2S . The oxidation peak at ~ 2.4 V can be attributed to the oxidation of lithium polysulfides (Li_2S_n , $n < 4$) back to higher order lithium polysulfides (Li_2S_n , $n > 4$). In theory two oxidation peaks are expected at the sulfur cathode, but in our case, these two peaks appear to merge into a single composite peak. We believe that, the resolution of the oxidation peaks in Li-S battery depend on the charge transfer resistance in the sulfur electrode. Sulfur cathode with better charge transfer properties, will allow all the polysulfide species to oxidize in parallel reactions, causing the peaks to merge in to a single peak. The charge transfer resistance depends on the electronic conductivity, porosity, and the surface area of the conductive material of the sulfur cathode. The work in [19] has reported cyclic voltammetry with two oxidation peaks for Li-S battery. They have reported cyclic voltammetry results for three different electrode architectures made of carbonized polyacrylonitrile (NPCNFs), CO_2 activated carbonized PAN (ACNFs), and carbonized PAN–Nafion nano-fibers (MCNFs). They show that as the surface area increases (MCNF > ACNF > NPCNF in that order), the corresponding oxidation peaks in the cyclic

voltammetry curves become less resolved and merge into a single peak as the surface area increases, presumably due to better charge transfer properties. The CV curve shown in Fig. 3.12b and discharge curves of Fig. 3.10b for a titania coated sulfur cathode shows remarkable durability over the cycles. This is an indication of the reformation of sulfur within the bulk electrode and minimal leakage of polysulfides into the electrolyte. In contrast, the uncoated sulfur electrode shows significant irreversibility in the CV diagram with shifting of peak positions and changes in current levels implying dissolution of polysulfides into the electrolyte. In this work, titania is expected to trap the polysulfides and the CV curves should not show a considerable current at the 2.8 V vertex as in Fig. 3.12b. This reasoning is confirmed by comparing the CV cycles of the uncoated sulfur electrode shown in Fig. 3.12a. It is noticeable that at 2.8 V vertex of Fig. 3.12a, there is a cathodic current ~ 2 mA, implying existence of dissolved polysulfides in the electrolyte still undergoing oxidation.

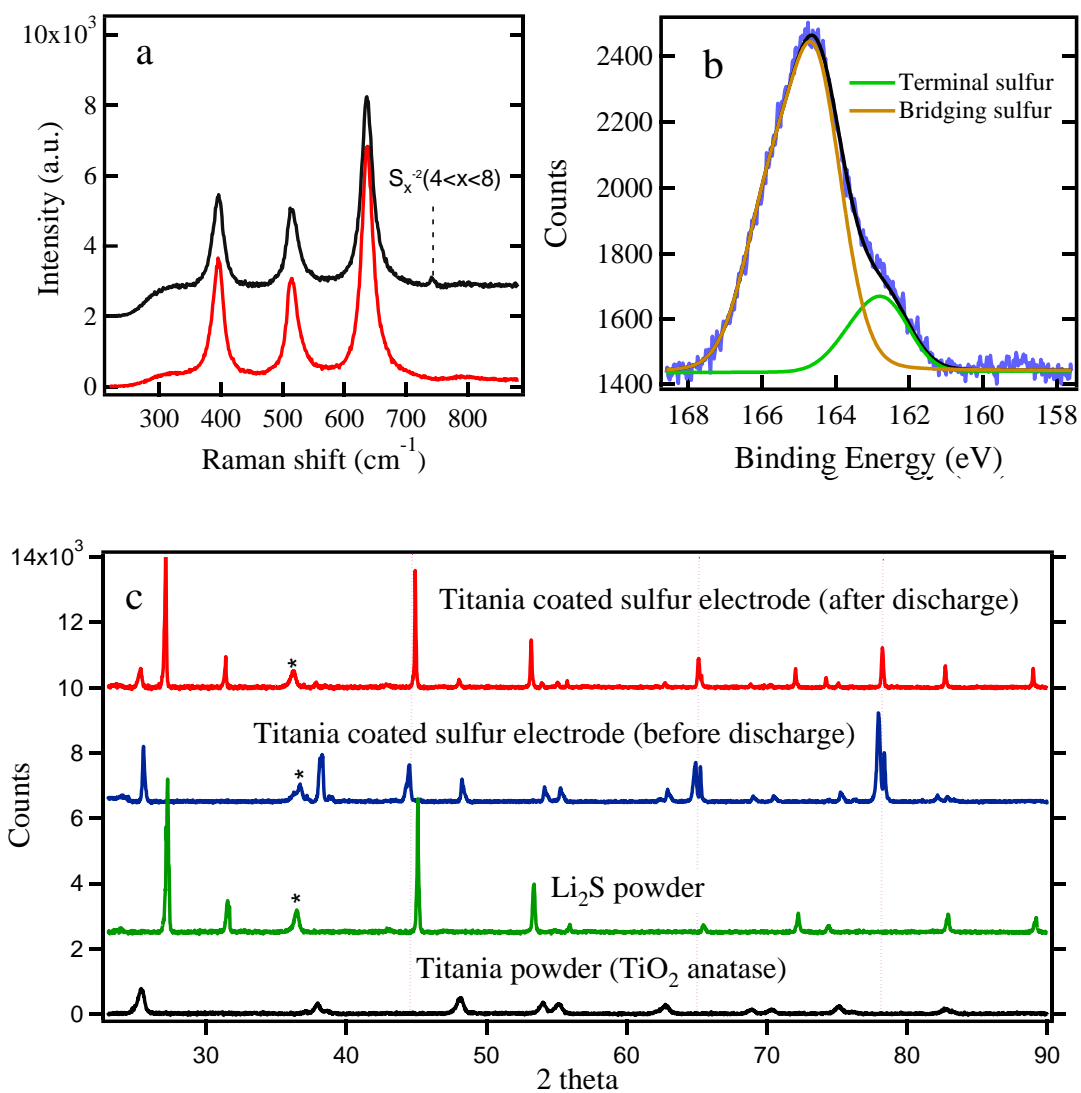


Figure 3.13. (a) Raman spectra of titania coated sulfur electrodes (ACP based) before and after discharge (b) XPS surface analysis for titania coating (c) XRD spectra of titania coated sulfur electrodes before and after discharge, spectra for Li_2S and TiO_2 powders are also shown for comparison. The * represents the signature of the polymer bag and the dotted vertical lines represent the aluminum substrate.

Raman and X-ray photo electron (XPS) analysis were carried out to further confirm the trapping of polysulfides in titania layer. In Raman spectrum analysis, we investigated titania coated electrode before and after discharge as shown in Fig. 3.13a. Both spectra show 3 clear peaks characteristic of crystalline anatase titania. An additional weak peak appearing at $\sim 742 \text{ cm}^{-1}$ for the discharged electrode can be interpreted as due to the polysulfide links (S_x^{-2} , $x=4-8$) [106].

Fig. 3.13b shows the sulfur 2P peak (S^{2p}) with 2 distinct peaks at 164.7 and 162.8 eV corresponding to bridging sulfur and terminating sulfur respectively [40]. This is possible due to the efficient trapping of higher order soluble polysulfides in the mesoporous TiO_2 layer.

The electrode which used in this analysis are washed with the 1:1 ratio of 1,2-Dimethoxyethane (DME Sigma Aldrich) and 1,3-Dioxiolane (DOL Sigma Aldrich) to remove any dissolved polysulfide from the surface of titania coating which might not have adhered to the titania surface. Thus, it is reasonable to conclude that the polysulfides detected by Raman and XPS are from the polysulfides which were adhered on titania particles. Fig. 3.13c compares XRD spectra for titania coated sulfur cathode before and after discharge. XRD spectra for pristine titania and Li_2S are also shown for comparison. It shows clear evidence of the presence of solid Li_2S after the first cycle discharge.

In the uncoated sulfur electrode, soluble polysulfides are expected to dissolve into the electrolyte. In the case of meso-porous titania coating, the dissolved polysulfide ions adsorb on titania surfaces and never reach bulk electrolyte beyond titania barrier. In the schematic diagram in Fig. 3.14, the processes of a Li-S battery with uncoated and titania coated cathodes have been categorized into several regions where key reactions take place.

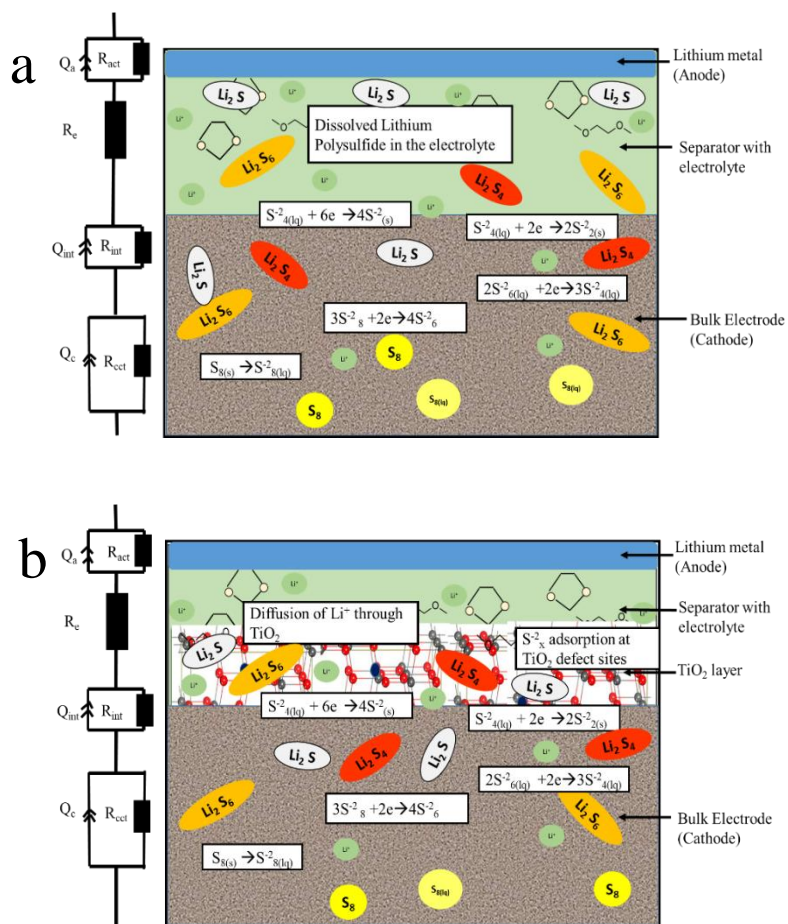


Figure 3.14. Schematics of the chemical processes in (a) uncoated and (b) titania coated sulfur electrode in Li-S battery.

EIS was used to determine impedances within coated and uncoated sulfur cathodes during cycling. Based on the Nyquist plots, an equivalent circuit has been proposed as presented in Fig. 3.14. Here, R_e represents the electrolyte resistance as a single series resistance in the network. The loops in the Nyquist plot consisting of superposition of multiple semicircles are each represented by a combination of a resistance and a constant phase element (CPE) in parallel. A similar equivalent circuit modeling and electrochemical impedance analysis can be found in the supporting materials of the work reported by Lin ma et al [29].

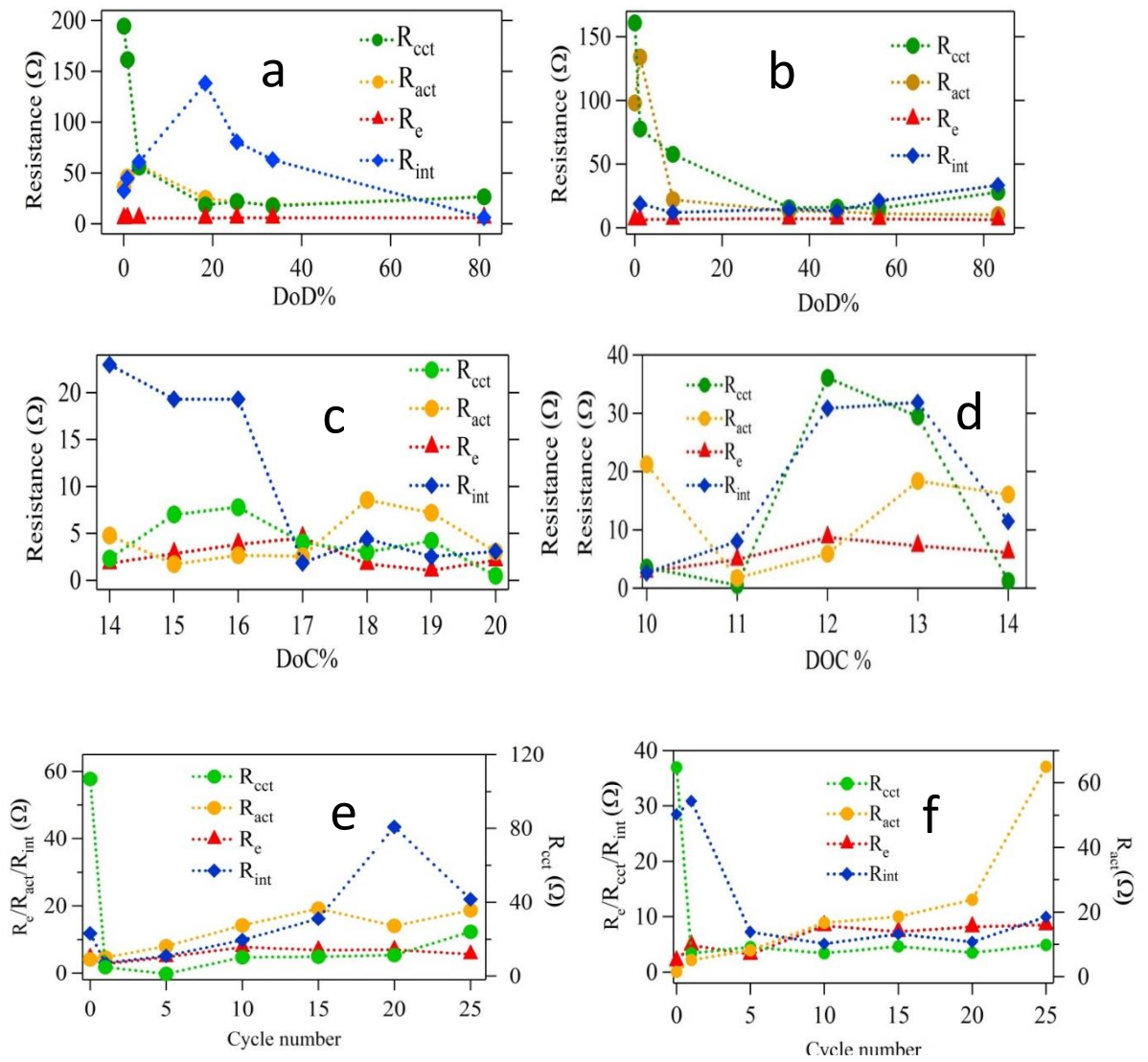


Figure 3.15. Fitting parameters of EIS data for ACP based sulfur cathode to an equivalent electrical circuit model: Each plot contains charge transfer resistance at cathode (R_{cct}), charge transfer resistance at anode (R_{act}), electrolyte resistance (R_e), and interface resistance (R_{int}). Plots (a) and (b) represent results for titania coated and uncoated samples respectively against DOD; plots (c) and (d) represent results for coated and uncoated samples respectively against DOC. Plots (e) and (f) represent results for titania coated and uncoated samples respectively against cycle number.

The choice of a CPE instead of a capacitor is due to the non-ideal behavior of the electrodes. Each semicircle represents (i) charge transfer at the cathode ($R_{\text{cct}}||\text{CPE}_{\text{cct}}$) (ii) charge transfer at the anode ($R_{\text{act}}||\text{CPE}_{\text{act}}$), and (iii) contact interphase at the cathode ($R_{\text{int}}||\text{CPE}_{\text{int}}$) which is present in the bulk of the cathode representing the charge conduction between the cathode current collector and the redox sites in the cathode. The variation of R_{int} in the case of titania coating is expected to be significant. The contribution of the anode impedance is neglected because the anode impedance in an electrolyte with polysulfides is small. Fig. 3.15 shows the relevant impedance parameters extracted by fitting the EIS data with the proposed equivalent circuit during (i) discharging, (ii) charging, and (iii) cycling processes.

The discharge curve has been categorized into three zones according to the key actions taking place in the cell. In zone 1, both electrodes are polarized, and solid sulfur starts to dissolve in the electrolyte. In zone 2, longer polysulfide chains are shortened via further reduction (in the presence or absence of titania). In zone 3, solid Li_2S and Li_2S_2 are formed. These solid products are more ionic in nature. In Fig. 3.15a and 3.15b, fitting parameters corresponding to charge transfer resistance (R_{cct}) and interphase resistance (R_{int}) at cathode for titania coated and uncoated sulfur electrode respectively during discharge are shown at various depth of discharge (DOD).

The behavior of the charge transfer resistance, R_{cct} at the cathode is similar in both cases. They both show initial decrease of R_{cct} reaching a minimum $\sim 40\%$ DOD followed by a slow increase. The initial decrease of R_{cct} can be interpreted as due to the improved electrochemical accessibility of solid sulfur (insulating) to undergo polysulfide formation. The following increase in R_{cct} is due to the formation of insulating and insoluble Li_2S and

Li_2S_2 . For both coated and uncoated sulfur electrodes this charge transfer process is similar. However, R_{int} shows distinctly different behaviors for coated and uncoated cathodes. In the case of titania coated cathodes, R_{int} value is seen to increase in zone 1, presumably due to the adsorption of dissolved polysulfides at the defect sites of titania. It is interesting to observe that the interphase resistance drops in zone 2, where longer polysulfides are reduced to shorter polysulfides.

During the charging of the cell, solid Li_2S and Li_2S_2 should eventually oxidize back to elemental sulfur through intermediate polysulfide formation. The analysis of the variation of the R_{int} during the charging process provides useful information about the underlying mechanism of the titania coated electrode as shown in Fig. 3.15c. Once Li_2S starts to oxidize to intermediate polysulfide chains, the interphase resistance, R_{int} is expected to decrease as the conductivity improves for the titania coated electrode (Fig. 3.15c). In contrast, the R_{int} of the uncoated sulfur electrode is seen to increase as charging progresses (Fig. 3.15d). It is reasonable to assume that this conversion ($\text{Li}_2\text{S}/\text{Li}_2\text{S}_2$ to intermediate polysulfides) may take place at the electrode matrix-electrolyte interface since there are considerable amounts of dissolved polysulfides remaining in the electrolyte. As the sulfur growth takes place on the surface, the interphase resistance, R_{int} continues to increase (Fig. 3.15d). It is also noted that, the effect on electrolyte resistance due to the dissolved polysulfide is considerably small (Fig. 3.15e) in the case of titania coated cathode.

Dissolution of polysulfides increases the viscosity of the electrolyte causing an increase in electrolyte resistance (R_e) noticeable in Fig. 3.15e and 3.15f in different magnitudes. Titania coated sulfur electrodes show a stabilized R_e , however, due to the adsorption activity of titania layer. It is evident from the relative magnitudes of the changes in R_e that

coating of the sulfur electrode with titania has significantly limited the polysulfide dissolution into the electrolyte. Finally, variation of, R_{act} during cycling is presented in Fig. 3.15e and 3.15f for both coated and uncoated cathodes as evidence for polysulfide shuttling and Li_2S and Li_2S_2 formation on the anode surface. Li_2S and Li_2S_2 are known to be formed on the anode by reducing the dissolved polysulfides (from cathode) in the electrolyte after shuttling to anode. For the uncoated sulfur cathode, R_{act} increases almost linearly until 20th cycle and then shows an abrupt rise confirming the continuous formation of Li_2S/Li_2S_2 on the anode. On the contrary, the titania coated cathode shows saturation of R_{act} after the 20th cycle implying limited formation of Li_2S/Li_2S_2 as a result of encapsulation of soluble polysulfide within the titania coating.

3.8 Conclusions

Titania coating of the sulfur electrode with proper electrical contact with the current collector has proven to be effective to enhance the cyclability of Li-S batteries by retaining a stable capacity of 980 mAh g⁻¹ discharge profile over 100 cycles. The performance of mesoporous titania coated sulfur was compared with that of uncoated sulfur electrodes using EIS and CV techniques. The mechanism of trapping dissolved polysulfide within the titania layer was verified by investigating *in-situ* impedance measurements. R_{act} of the cell with titania coated sulfur electrode was stabilized at 20 Ω while R_{act} for uncoated sulfur electrode continued to rise beyond 20 Ω during charging and discharging. Such increase in charge transfer resistance at the anode in uncoated sulfur cathode is due to deposition of solid Li_2S on lithium metal anode. The electrical bridging technique to improve the electrical conductance between the interior of the sulfur/carbon composite and the current collector is proven to contribute significantly for the superior performance of titania coated

sulfur electrodes. Otherwise, the role of titania to improve the cyclability of sulfur electrode with high discharge capacity will be undermined due to the poor electrical conductance between the interior of the electrode and the current collector. In addition, Raman and XPS analysis confirm the effective polysulfide trapping by the mesoporous titania coating even though the isolation of different polysulfide species was difficult. Finally, the XRD analysis concludes non-existence of any phase changes in titania confirming that the polysulfide is trapped only by adsorption onto titania.

CHAPTER 04

ANODE DEVELOPMENT USING α -MoO₃ FOR HIGH CAPACITY Li-S BATTERIES

4.1 Scope

This chapter is mainly focused on using pre-lithiated α -MoO₃ as an anode material in Li-S batteries to eliminate the Li metal anode. This goal is reached by synthesizing α -MoO₃ by HWCVD technique and proposing a novel method to pre-lithiate α -MoO₃. The application of pre-lithiated α -MoO₃ as an anode material with sulfur cathode is discussed and its electrochemical performances are also presented.

4.2 Introduction

When sulfur electrodes are tested against lithium metal as the anode (half-cell), the electrochemical performance suffers from lithium metal related phenomena such as dendrite formation [107] and SEI layer [108] etc. In order to construct full Li-S cells, the candidate materials for anode must be carefully chosen by considering their cathodic and anodic potential and capacity matching. Graphite, Si and Sn etc. fulfill the above requirements and have been studied as anodes in Li-ion full cells

The anode which we discussed here has been adopted from the work reported in Ref [9]. They have demonstrated α -MoO₃ to be a good anode material for Li-ion batteries with initial discharging capacity of 1043 mAhg⁻¹. This discharging capacity as an anode material is a good match for sulfur cathode to be used in a Li-S full cell. MoO₃ is known

to have several phases. α - MoO_3 and β - MoO_3 were found to coexist in their material synthesized by Hot Wire CVD technique. In a typical Li-S half-cell, two distinct plateaus can be observed in the potential-capacity curves at two different potentials. These plateaus are prominent partly due to the high electrical conductivity of Li metal. Li-S full cells made of silicon anode also show the two step discharge plateaus due to the better charge transfer processes as a result of their high electrical conductivity. Several researches have attempted fabricating Li-S full cells using silicon anodes. Ref [109], discusses a method of fabricating a silicon nanowire anode mixed with carbon and three dimensionally deposited Au nanoparticles. Another group [110] has fabricated Li-S full cell using Li_2S -C cathode and Si/C anode. A Li-S full cell, starting from Li_2S cathode and silicon nanowire anode has been investigated in [111]. In each case similar performances have been observed with continuous degradation of discharge capacity. The reason for such degradation is due to the use of poorly encapsulated sulfur in the cathode and degradation of Si upon continuous cycling. However, in this work we are using an optimized mesoporous TiO_2 coated sulfur electrode which we have investigated recently[112]. Therefore, we believe that, the electrochemical characteristics of pre-lithiated α - MoO_3 can be isolated and observed in a Li-S full cell. In [9], it has been found that, high capacity with good stability can be achieved by adding small amount of Si nanoparticles to Hot Wire CVD deposited α - MoO_3 . To our knowledge, this is the only work on Li-S full cell using pre-lithiated α - MoO_3 ($\text{Li}_{1.33}\text{Mo}_{0.66}\text{O}_2$) anode. Therefore, we believe that the work discussed in this dissertation can lead to valuable finding on Li-S battery technology.

4.3 α -MoO₃ synthesis and S-Li@MoO₃ full cell assembling in coin cell format

The sulfur cathode is prepared using activated carbon according to the method described in Chapter 3 by coating a sulfur/activated carbon electrode with mesoporous TiO₂.

In order to synthesize α -MoO₃ for the anode, first the method described in [9] was followed using a hot wire CVD technique. The material was deposited on the inner wall of quartz glass tube using a co-centric Mo wire. The synthesis process was carried out for about 72 hours to collect ample amount of MoO₃ and scraped off the reactor in powder form. The resulting MoO₃ was analyzed by XRD and confirmed to be α -MoO₃. The color of as synthesized α -MoO₃ was found to be blue, which is typical for α -MoO₃. In order to reproduce the results reported in [9], Si nanoparticles suspended in ethanol is added to α -MoO₃ in micro gram quantity. Then, 5 mg of Silicon decorated α -MoO₃ is mixed with 7 mg of teflonized carbon binder (mixture of Polytetrafluoroethylene (PTFE) and acetylene black). This enables easy processing of electrode material to form circular pellets (0.7 mm in diameter and 0.5 mm thick) which can be easily pressed on to a stainless-steel mesh (Alpha Aesar- 80 mesh) current collector fitting in CR2032 coin cells. Before the assembly of full cell, it is important to ensure proper quantities of the anode and cathode materials. In the half-cell assembly, metallic Li acts as a reservoir for Li-ions, whereas in the full cell configuration, the lithiated anode materials is the only source of Li-ions (in addition to electrolyte). Therefore, capacity balancing is necessary to ensure the availability of active material during cycling. Simple calculation of such capacity matching of sulfur cathode and Li_{1.33} Mo_{0.66}O₂ anode yields that ~5 mg of α -MoO₃ is required with 2 mg of sulfur. A detailed description about the calculation considering the mass balancing of the full cell is included in the supporting material. First, α -MoO₃ and Lithium metal electrodes were

assembled in the coin cell format in a dry argon glove box as the initial step towards the Li-S full cell fabrication process. The electrolyte used in this cell is 1:1 ratio of 1,2-Dimethoxyethane (DME Sigma Aldrich) and 1,3-Dioxialane (DOL Sigma Aldrich) and 1M of Bis(trifluoromethanesulfonimide) lithium salt (LiTFSI) and 1% wt of LiNO₃. The assembled coin cell was connected to a battery tester (Arbin-16 cannels) and α -MoO₃ was galvanostatically lithiated with a constant current of 0.14 mA (C/10) to form Li_{1.33}Mo_{0.66}O₂. In this electrochemical lithiation process, α -MoO₃ electrode functions as a cathode. After α -MoO₃ is fully lithiated, the coin cell was disassembled inside the glove box and Li_{1.33}Mo_{0.66}O₂ electrode was carefully and assembled as the anode in a fresh coin cell against afore mentioned sulfur electrode with fresh electrolyte which is same as in the lithiation process. Then the new S- Li_{1.33}Mo_{0.66}O₂ full cell was connected to the battery tester to perform the galvanostatic electrochemical testing.

The electrochemical activity of the S- Li_{1.33} Mo_{0.66}O₂ full cell is further investigated using cyclic voltammetry and electro-chemical impedance techniques using a three-electrodes Swagelok cell. The three electrodes Swagelok cell consisting of active cathode (sulfur) and anode (Li_{1.33}Mo_{0.66}O₂) as the working and counter electrodes with a platinum wire as the reference electrode.

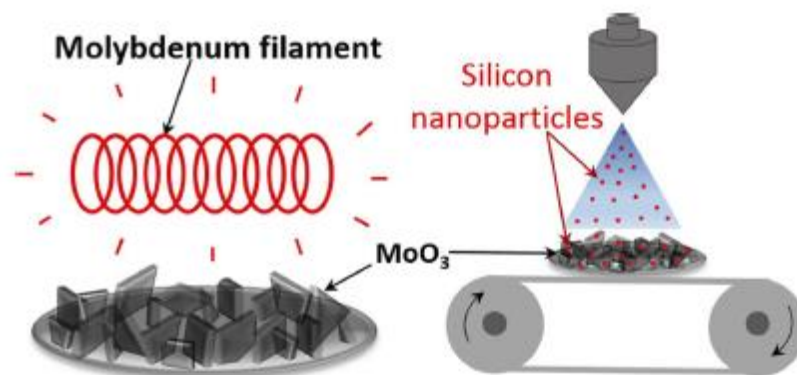


Figure 4.1. Synthesis process of α -MoO₃ using Hot Wire CVD technique [9]

4.4 Electrochemical and structural analysis

The full cells were cycled between 0.5 V and 2.8 V in galvanostatic mode using 16 channel Arbin battery test system. Cyclic voltammetry (CV) was performed at a scan rate of 0.3 mV/s in the range of 1.5 to 2.8 V (in a three electrode Swagelok cell configuration) using a biologic sp-200 electrochemical system. AC electrochemical impedance spectroscopy (EIS) of the cell was also studied in the three electrodes configuration using the same electrochemical system over the frequency range of 1 mHz to 1 MHz. All the measurements were carried out at 25 °C.

4.5 Characterization

The morphology of the electrode surface was characterized by a TESCAN scanning electron microscope (SEM). X-ray Diffractometer (Bruker D8) employed to analyze the MoO₃.

4.6 Results and discussion

In the beginning, similar to the work reported in [9], α - MoO_3 was directly deposited on a stainless steel substrate using hot filament CVD and used in half cell configuration against Li in a coin cell. After full lithiation, the cell was disassembled and the binder free anode material ($\text{Li}_{1.33}\text{Mo}_{0.66}\text{O}_2$) was tested in a Li-S full cell against sulfur cathode. However, they appear to degrade the capacity very quickly presumably due to delamination of anode material. Therefore, to eliminate delamination problem α - MoO_3 is synthesized by Hot Wire CVD and scraped into a powder form and then mixed with carbon and binder in such a way that, mAh charge capacity (vs Li/ Li^+) is matched with the sulfur electrode. To confirm the electrochemical activity of Si decorated MoO_3 in carbon/binder matrix, *in-situ* XRD test is carried while the α - MoO_3 is being lithiated. Fig. 4.2 shows *in-situ* XRD spectra during lithiation (including the spectrum of the as prepared material) of Hot Wire CVD deposited MoO_3 powder in teflonized acetylene black carbon binder electrode. The XRD results confirm that the pre-lithiation process in our sample is similar to that of directly deposited α - MoO_3 on stainless steel reported in [9]. The diffraction pattern of the as prepared Si@ MoO_3 (red curve) is consistent with α - MoO_3 (JCPDS 00-005-0508) having an orthorhombic crystal structure and cell parameters $a = 3.962 \text{ \AA}$, $b = 13.858 \text{ \AA}$, $c = 3.697 \text{ \AA}$. The XRD spectra at the discharge voltages of 1.5 V, 1 V, and 0.2 V (black curves) show peaks corresponding to $\text{Li}_2\text{Si}_2\text{O}_5$ (004 and 111 reflections) and $\text{Li}_{1.33}\text{Mo}_{0.66}\text{O}_2$ (311 and 400 reflections) (JCPDS 01-073-2300). Interestingly, 311 peak downshifts as the lithiation progresses implying increase of d spacing during lithiation.

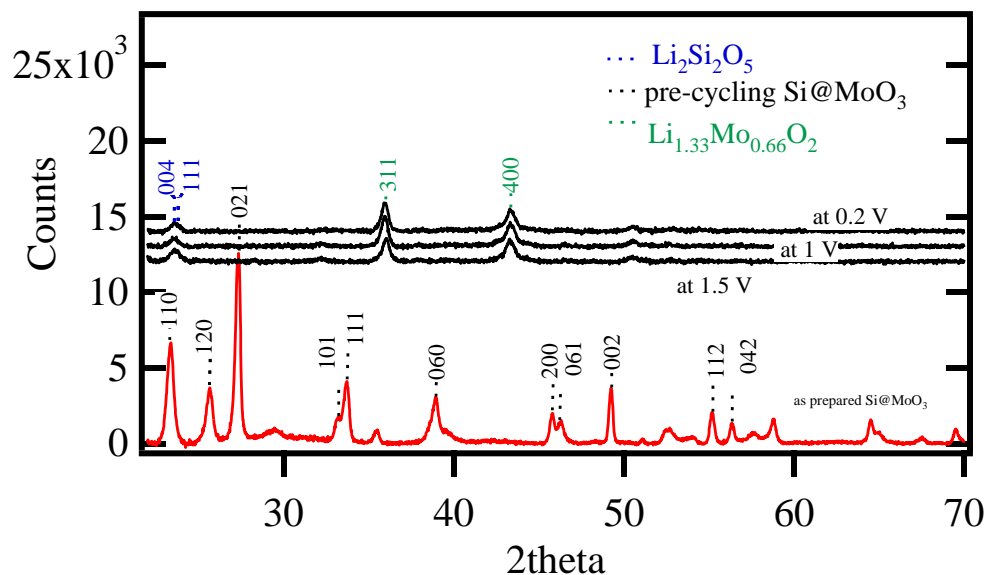


Figure 4.2. *In-situ* XRD analysis for pre-lithiation of Hot Wire CVD deposited MoO_3 powder in teflonized acetylene black carbon binder electrode. $\alpha\text{-MoO}_3$ [00-005-0508], $\text{Li}_{1.33}\text{Mo}_{0.66}\text{O}_2$ [01-073-2300] and $\text{Li}_2\text{Si}_2\text{O}_5$ [00-015-0637]

The discharge characteristics of the S- $\text{Li}_{1.33}\text{Mo}_{0.66}\text{O}_2$ full cell assembled in coin cell configuration are presented in Fig. 4.3a and 4.3b during cycling at C/10 rate. Initial capacity of 905 mAhg^{-1} is seen to retain at 400 mAhg^{-1} (with respect to sulfur weight) after 50th cycle at C/10 rate. The full cell is designed in such a way that the capacity is limited by the cathode. The cell has an open cell potential of around 2.3 V. The IR drop of the voltage-capacity curve is higher compared to a Li-S half-cell. The specific capacity is seen to fade steadily with the cycle number. One reason could be due to the Li^+ loss at the solid electrolyte interface. To improve the stability of the gravimetric capacity retention, we may have to investigate different stable electrolytes which broaden the scope of this research. This assumption is validated by the near 100 % coulomb efficiency indicating that at each cycle there is a loss of Li^+ ions at the SEI layer. Degradation of sulfur electrode may also

contribute for such capacity loss, but it may be small according to the CV (Fig .4.4a to be discussed later)

Full cells are assembled in three electrodes Swagelok cell configuration for cyclic voltammetry and electrochemical impedance measurements. These techniques can shed light on further understanding of S-Li_{1.33}Mo_{0.66}O₂ full cell electrochemistry. Fig. 4.4a shows the cyclic voltammetry (CV) curve of S-Li_{1.33}Mo_{0.66}O₂ full cell. Three electrodes Swagelok test cell

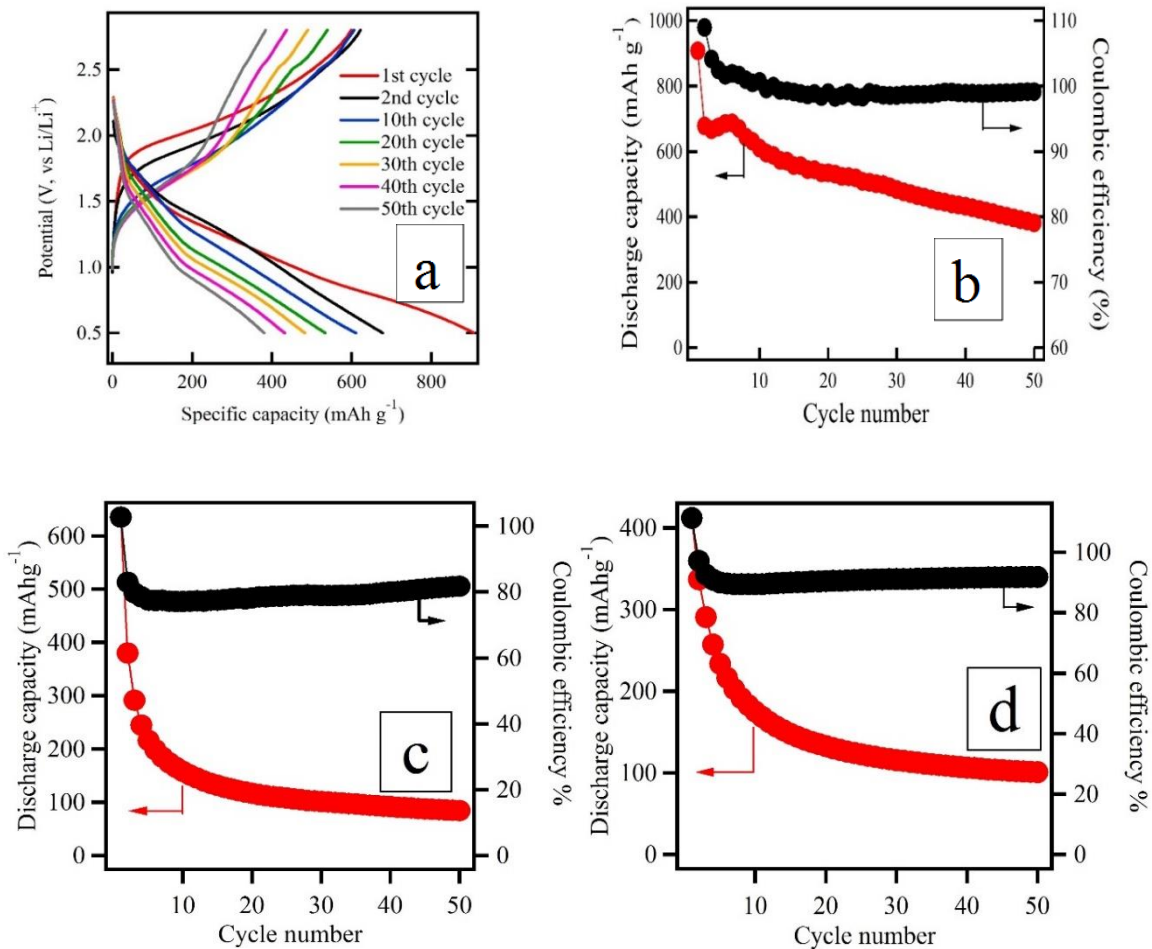


Figure 4.3. (a) Potential vs discharge curve of S-Li_{1.33}Mo_{0.66}O₂ full cell, at C/10 rate (b), (c) and (d) capacity vs cycle number and coulomb capacity of Li_{1.33}Mo_{0.66}O₂-S full cell at C/10, C/3 and 1 C.

(schematically shown in Fig.4.4b) was used for the CV by keeping lithium as the reference electrode, $\text{Li}_{1.33}\text{Mo}_{0.66}\text{O}_2$ anode as the counter and sulfur cathode as the working electrode. Potential is measured in the range of 2.8 -1.5 V between working and reference electrodes while the current is applied between working and counter electrodes. As can be seen from the CV curves shown in Fig. 4.4a, the oxidation and reduction electrochemical activity in the sulfur (working) electrode is compatible with Li-S half-cell electrochemical activity [112]. The reduction peak at 2.4 V is known to occur when soluble Li_2S_8 forms. Further reduction of longer poly sulfide chains to shorter poly sulfide chains first forming soluble Li_2S_6 and Li_2S_4 and finally converting to solid forms of Li_2S_2 and Li_2S is represented by a second reduction peak at 1.9 V. The presence of oxidation peak at 2.5 V, confirms the reversibility of the S- $\text{Li}_{1.33}\text{Mo}_{0.66}\text{O}_2$ full cell which requires enough Li ions (available from the counter electrode) during the cell cycling

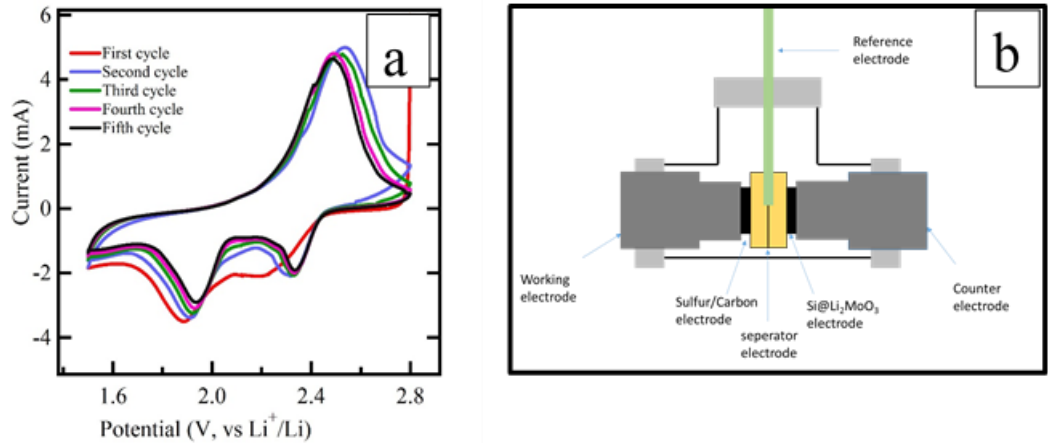


Figure 4.4. (a) Cyclic voltammetry curve of S- $\text{Li}_{1.33}\text{Mo}_{0.66}\text{O}_2$ (working electrode vs reference electrode) (b) Schematic of three electrode Swagelok test cell which used for CV.

Finally, the electrochemical impedance analysis (EIS) is carried out in the T-Swagelok cell, (schematically shown in Fig. 4.4b) but with a platinum wire as the reference electrode. The sulfur electrode is used as the working electrode while $\text{Li}_{1.33}\text{Mo}_{0.66}\text{O}_2$ electrode is used as the counter electrode. For EIS studies, a platinum wire used as the reference electrode due to its ability to work alone as a reference electrode [113] and to minimize the influence on EIS data. Further, the reference electrode is positioned in the middle of two glass-fiber separators of equal thickness (1 mm).

The impedance was measured in the A/C frequency range of 1MHz to 1mHz at potential values of 1 V, 0.7 V and 0.5 V and 0.2 V (100% DoD) during the discharge and at 1 V, 1.5 V, 2 V and 2.8 V (100% DoC) during the charging as shown in Fig. 4.5a and 4.5b.

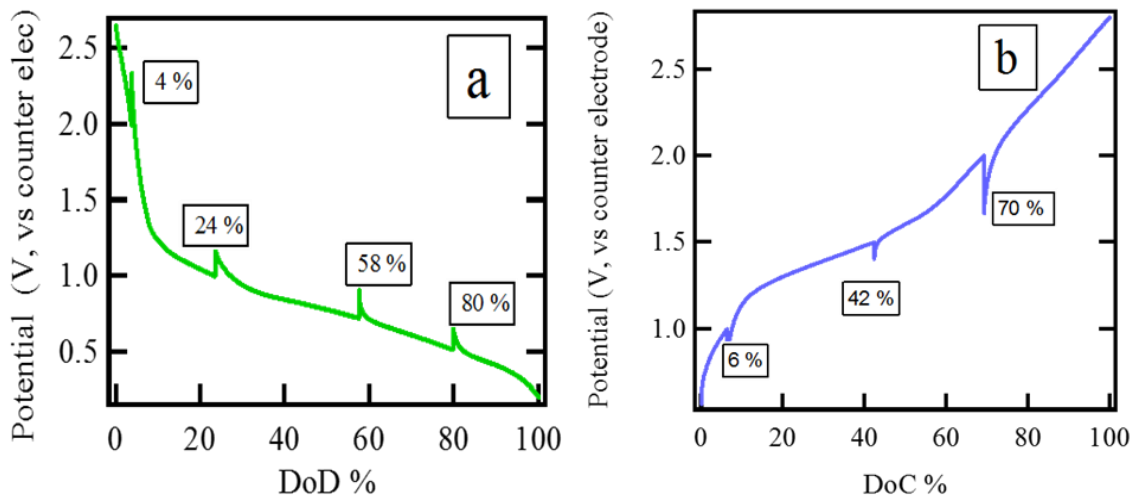


Figure 4.5. (a) discharging and (b) charging curves for impedance analysis. DoD % (percent depth of discharge), DoC % (percent depth of charge). Sharp peaks on discharge and charge curves indicate the points at which the impedance was measured.

Fig. 4.6c and 4.6d show the Nyquist plots for pristine full cell (0 % discharge) while Fig. 4.6e and 4.6f show the Nyquist pots at 100 % (2.8 V) charge. Equivalent circuit in Fig. 4.6a was used to fit the Nyquist pots of cathode and equivalent circuit in Fig. 4.6b used to fit Nyquist plots of anode. Nyquist plots were fitted using EIS fitting software (EC-LAB). A constant phase element and a resistor in parallel represent a semi-circle of Nyquist plots. Two convoluted semi-circles were identified in each Nyquist plot. Resistance values were identified for the electrolyte resistance (R_e), Charge transfer resistance (R_{cct} and R_{act}) and interface resistance (R_{int}) by fitting with appropriate network models. It is clearly noted that, in the Nyquist plot for the working electrode, the Warburg diffusion behavior is not present because Li_2S is a conversion reaction, which minimizes diffusion contribution. However, the Warburg contribution due to the diffusion is clearly present in the Nyquist plot of the counter electrode which is due to the intercalation of Li^+ in the anode.

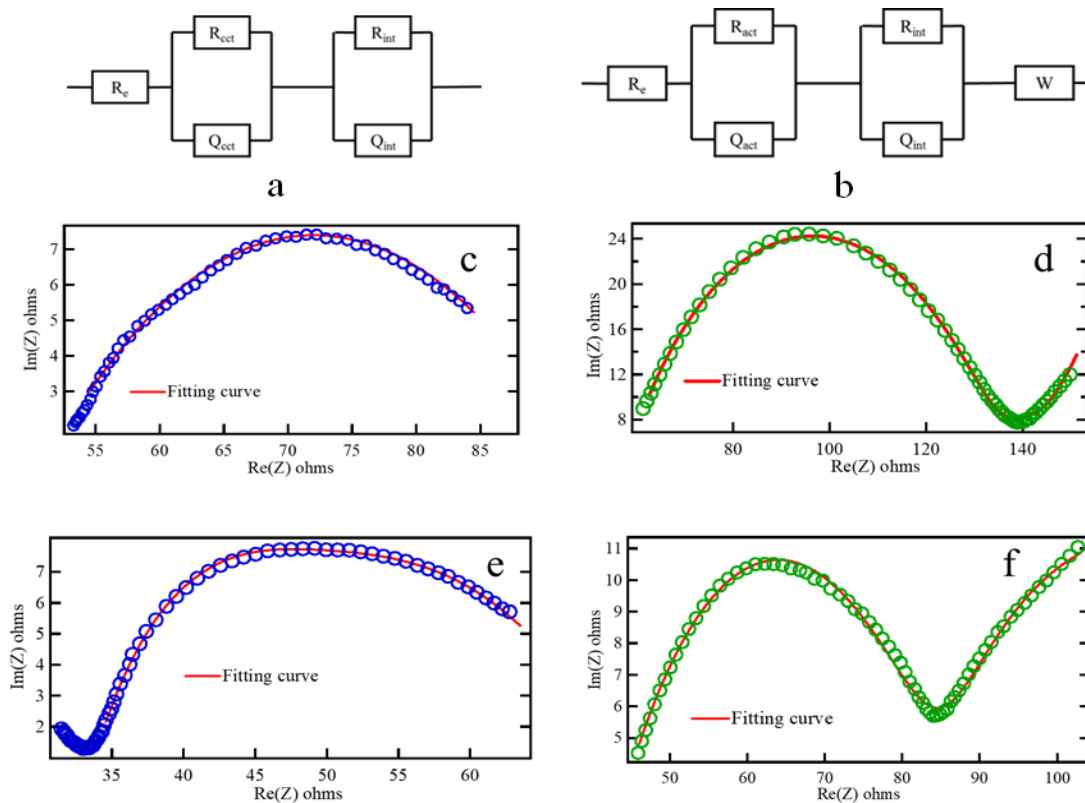


Figure 4.6. (a) equivalent circuit for the working electrode and (f) equivalent circuit for counter electrode Nyquist plots of c) working (sulfur) electrode at discharge. d) counter ($\text{Li}_{1.33}\text{Mo}_{0.66}\text{O}_2$) electrode at discharge e) working electrode at charging, f) counter electrode at charging

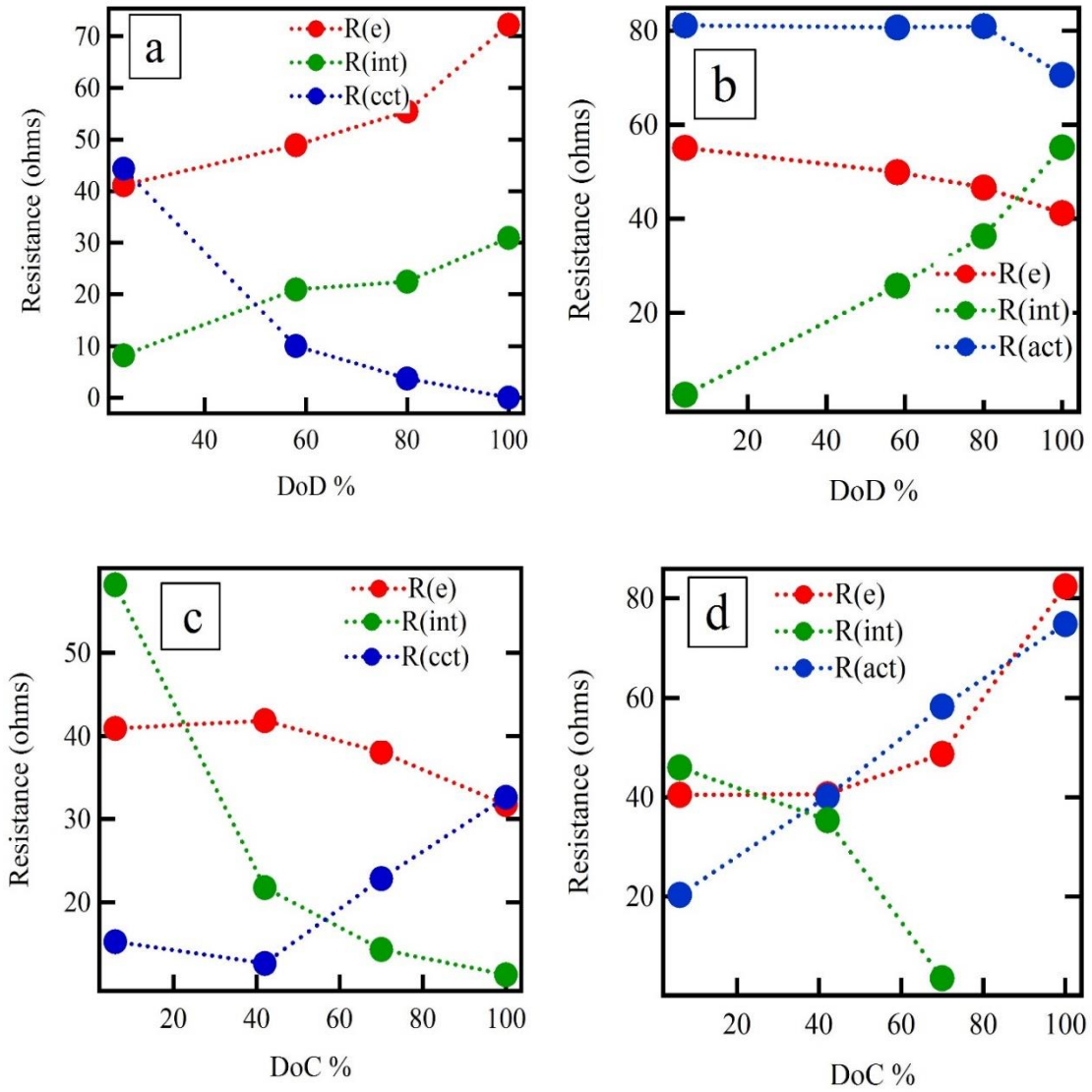


Figure 4.7. Fitted resistance values at depth of discharge (DoD) and depth of charge (DoC) for (a) and (b) working electrode and counter electrode at discharge, (c) and (d) working electrode and counter electrode at charge

Fig. 4.7a-d show the fitted resistance values, $R(e)$, $R(cct)$, and $R(int)$. The increment of electrolyte resistance, $R(e)$ in Fig. 4.7a (cathode) indicates that lithium polysulfides are formed and hence electrolyte resistance increases from the initial value of 40Ω up to about 70Ω at 100 % discharge. As the electrochemical reaction progresses in the sulfur electrode, charge transfer resistance, $R_{(cct)}$ decreases since electrically insulating elemental sulfur is converted into ionic Li_2S . In the same time, solid electrolyte interface on sulfur electrode, $R_{(int)}$ increases from the initial value of 10Ω to the final value of 30Ω . This could be due to the solid Li_2S formation which could influence in electrode-electrolyte interactions. The electrolyte resistance $R_{(e)}$ near anode electrode, however, shows a decrease by few ohms while the interface resistance rises on the anode as well (Fig. 4.7b). Charge transfer resistance of counter electrode, $R_{(act)}$ at discharge however is comparatively stable. Thus, we can assume that, Carbon/ $Li_{1.33}Mo_{0.66}O_2$ electrode integrity is intact while discharging. When the full cell is charged (Fig. 4.7c), it is noticeable that, $R_{(e)}$ near the sulfur electrode is decreased as the polysulfide concentration is lowered due the oxidation of S^{-2} to S . charge transfer resistance $R_{(cct)}$ is increased as the cathode accumulates sulfur introducing poor electronic conductivity of the cathode. It is an interesting phenomenon to observe that, $R_{(int)}$ at cathode drops as the cell is re-charged which is the expected result when Li_2S dissociate in Li an S . Anode (Fig. 4.7d) on the other hand shows an increase of $R_{(e)}$ and $R_{(act)}$. This can be explained as due to the shuttling of any dissolve polysulfides towards the anode. Migration of dissolved polysulfides is believed to increase the electrolyte resistance ($R_{(e)}$). Increase of $R_{(act)}$ could be due to the lattice expansion of $Li_{1.33}Mo_{0.66}O_2$ upon recharge, hence Carbon/ $Li_{1.33}Mo_{0.66}O_2$ contact loss.

4.7 Conclusions

In this work, it has been proven that $\text{Li}_{1.33}\text{Mo}_{0.66}\text{O}_2$ is a potential candidate as an anode material in Li-S batteries. Cyclic voltammetry curves indicate that redox reactions in the sulfur electrode performed similar to in Li-S half-cell. In addition, $\alpha\text{-MoO}_3$ can be synthesized in high quantities using H_2/Ar so that $\alpha\text{-MoO}_3$ can be used in powder form to scale up the Li-S full cell fabrication.

CHAPTER 05

HIGH ENERGY DENSITY LITHIUM MOLYBDATE-SULFUR POUCH CELL FORMATION

5.1 Scope

In this Chapter, methods for improving the α -MoO₃ yield and the material quality are described. First, synthesis of α -MoO₃ by hydrogenation of impure MoO₃ is discussed. Then, a novel three electrode pouch cell design is presented which facilitates the Li-S pouch cell formation in one step process. Then, the performance of assembled pouch cell will be improved using α -MoO₃ nanowire structures. Finally, the technical details of making a high energy density pouch cell is described.

5.2 Material preparation

After preliminary investigation of S- Li_{1.33}Mo_{0.66}O₂ full cell in coin cell configuration, it was necessary to scale up the α -MoO₃ production to enable the fabrication of high energy Li-S cells. The amount of α -MoO₃ synthesized using hot wire CVD technique described above is very low (20 mg in 72 hours). In order to scale up the α -MoO₃ synthesis, a novel and cost-effective method was investigated. First, synthesis of pre-lithiated MoO₃ using solvo-thermal technique was attempted using LiOH and MoO₂, but only resulted in Li₂MoO₄, which for obvious reasons is not a good reversible anode material for Li-S full cell applications. Since Mo in Li₂MoO₄ is at its highest oxidation state (+6), when

assembled against a sulfur electrode, it cannot oxidize any further via delithiation and cannot generate any open circuit voltage. Further, it was found to be difficult to directly intercalate lithium into layered MoO_3 using chemical or solvo-thermal techniques.

It was necessary to synthesize $\alpha\text{-MoO}_3$ in bulk quantity and to develop a technique to assemble a Li-S full cell using a single step process, which eliminates the cumbersome process of disassembling the cell after initial lithiation and re-assembling as we did for Li-S full cell in coin cell format. In order to synthesize $\alpha\text{-MoO}_3$ in bulk quantity, Mo was oxidized by heating Mo powder at 500 °C in air for two hours. The as prepared MoO_3 (white powder) was found to be monoclinic but converted to orthorhombic $\alpha\text{-MoO}_3$ after the reduction by heating in a flow of 40% H_2/Ar (50 sccm) at 150 °C. After 10 hours of processing, the initial white powder turned blue and the final product was found to be predominantly $\alpha\text{-MoO}_3$ as evidenced by XRD.

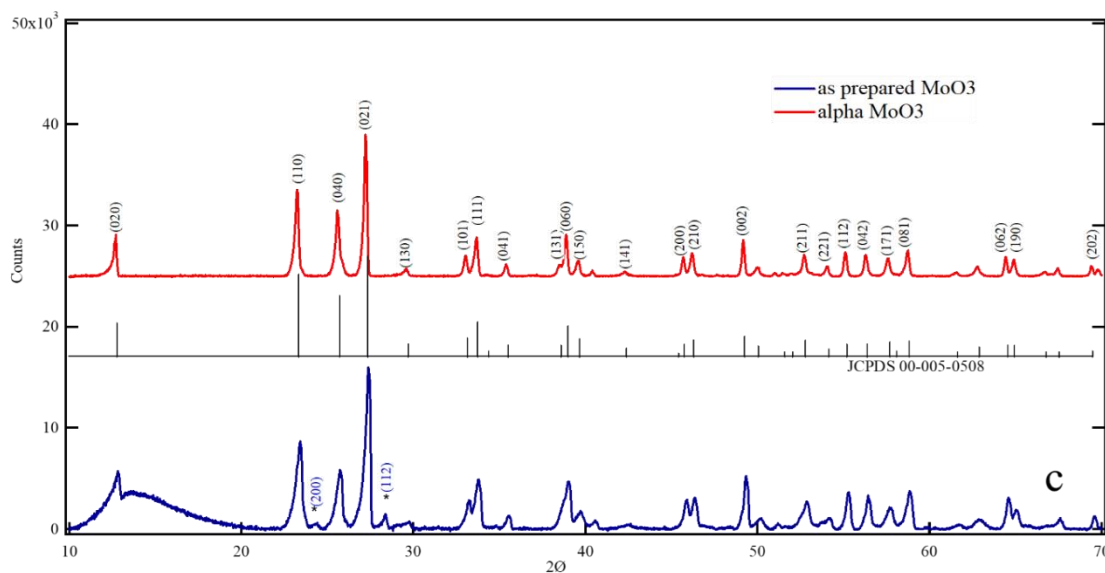
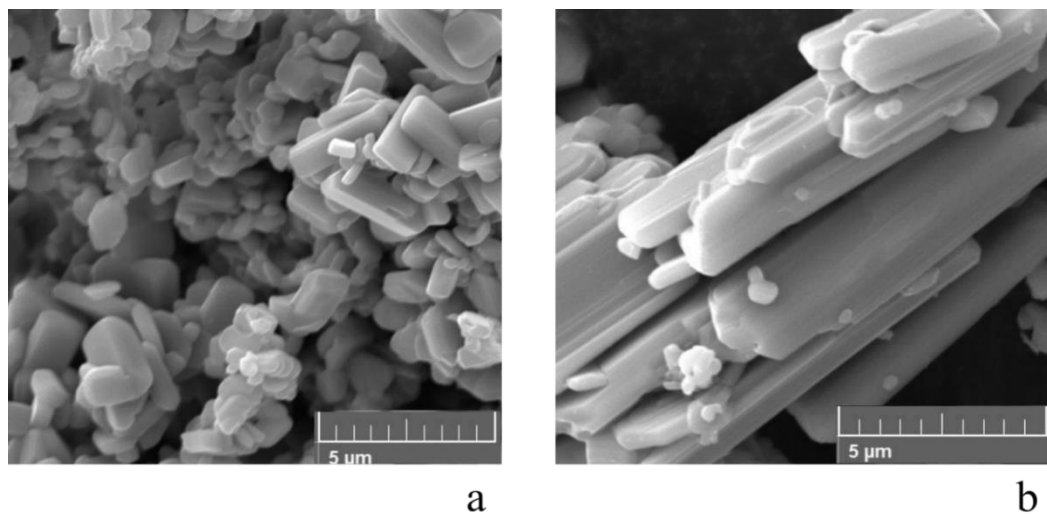


Figure 5.1. (a) as prepared MoO_3 after oxidizing at 500°C (b) $\alpha\text{-MoO}_3$ after reduction in 40 % H_2/Ar at 150°C (c) XRD spectrums of as prepared MoO_3 and $\alpha\text{-MoO}_3$ after reduction in 40 % H_2/Ar .

Fig. 5.1 (a) and (b) show the SEM images of as prepared MoO_3 (by direct oxidation of Mo powder) and after reduction in a flow of Ar/H_2 respectively. The as prepared MoO_3 sample consists of planar platelets co-existing with other irregular particles smaller than $5\ \mu\text{m}$ as seen by the SEM image in Fig 5.1 (a). It appears that the initial oxidation of Mo results in

mixed α/β -MoO₃ phases. After reduction in H₂/Ar, the morphology of the particles has been changed primarily to larger planar platelets of α -MoO₃ as evidenced by the SEM image in Fig. 5.1b. Fig. 5.1c shows the XRD spectra of MoO₃ sample before and after reduction. The XRD spectrum for the sample before reduction is consistent with α -MoO₃ (JCPDS 00-005-0508) having an orthorhombic crystal structure and cell parameters $a=3.962$ Å, $b=13.858$ Å, $c=3.697$ Å and additional peaks located at $2\theta = 23.95^\circ$ and 28.73° which were assigned to the characteristic reflections from (020) and (112) planes of β -MoO₃ (JCPDS 01-084-1360), respectively. The XRD pattern for the sample after reduction mostly consists of α -MoO₃.

Electrochemical characteristics of half-cell prepared by the α -MoO₃ cathode and Li anode can be found in Appendix 1, Fig. 3. In order to assemble high energy Li-S cells, electrodes were assembled in a pouch cell configuration. The main goal of this Li-S prototype is to fabricate a Lithium sulfur cell in a single step. In practice, direct synthesis of prelithiated α -MoO₃ was found to be difficult. When α -MoO₃ is electrochemically prelithiated, Li⁺ intercalate between the α -MoO₃ layers. (intercalation effectively takes place only in layered structures.) Therefore, it was necessary to adopt a special design as shown in Fig. 5.2 to fabricate a Li-S full cell starting with α -MoO₃ (before lithiation) and sulfur cathode using a single step process. The schematic diagram in Fig. 5.2 of the pouch cell shows (a) before lithiation of α -MoO₃ (b) after lithiation of α -MoO₃. Red dashed lines show the separator completely covering both electrodes. Middle inter layer in green color is the lithium foil supported on a stainless-steel mesh.

Both cathode (sulfur) and anode (α -MoO₃ prior to lithiation) were synthesized in the ambient environment and Aluminum and Nickel tabs were spot-welded to the cathode and

anode respectively as the battery terminals. A Polypropylene separator (25 μm) was then wrapped around each electrode. The pouch was fabricated using laminated aluminum sheets (MTI battery corporation). When designing the pouch cell prototype, target capacity was determined to be 5 mAh, Mass loading, electrode size and pouch size were decided according to the mAh capacity of the pouch cell. Pouch and electrodes were dried in vacuum at 80 $^{\circ}\text{C}$ and then loaded into an Argon glove box for final assembly of the pouch cell. In this special pouch cell design, an additional thin lithium metal foil (80 μm) is sandwiched with two electrodes which are already wrapped with separators. The Lithium foil serves as a sacrificial layer which is only utilized to lithiate the $\alpha\text{-MoO}_3$ anode. After loading the components in to the pouch, 0.5 ml of electrolyte consisting of 1:1 ratio of 1,2-Dimethoxyethane (DME Sigma Aldrich) and 1,3-Dioxialane (DOL Sigma Aldrich) and 1M of Bis(trifluoromethanesulfonimide) lithium salt (LiTFSI) and 1% wt. of LiNO_3 was filled. Pouch cell is then sealed using a pouch cell sealer inside the glove box. In this initial lithiation process, terminal “L” (Lithium metal) and the terminal “M” ($\alpha\text{-MoO}_3$) are connected to the battery tester as the counter electrode and the working electrode respectively. After $\alpha\text{-MoO}_3$ is fully lithiated, terminal “M” and terminal “S” (Sulfur) are connected to the battery tester as the counter electrode and the working electrode respectively for full cell cycling. When the full cell is designed, balancing of the electrodes masses is carefully done considering the sulfur cathode as the capacity limiting electrode.

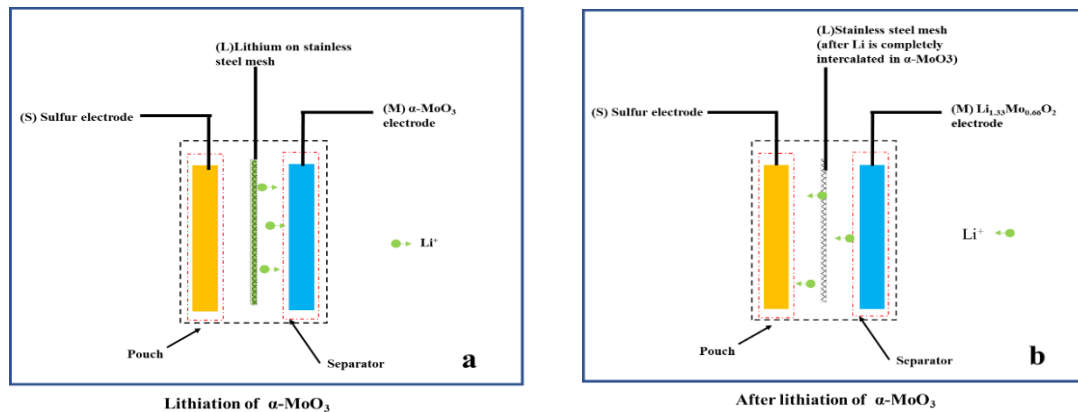


Figure 5.2. Schematic diagram of the pouch cell (a) before lithiation of $\alpha\text{-MoO}_3$ (b) after lithiation of $\alpha\text{-MoO}_3$. Red dashed lines show the separator completely covering both electrodes. Middle inter layer in green color is the lithium foil supported on a stainless-steel mesh.

5.3 Electrochemical measurements of lithium molybdate-sulfur pouch cells

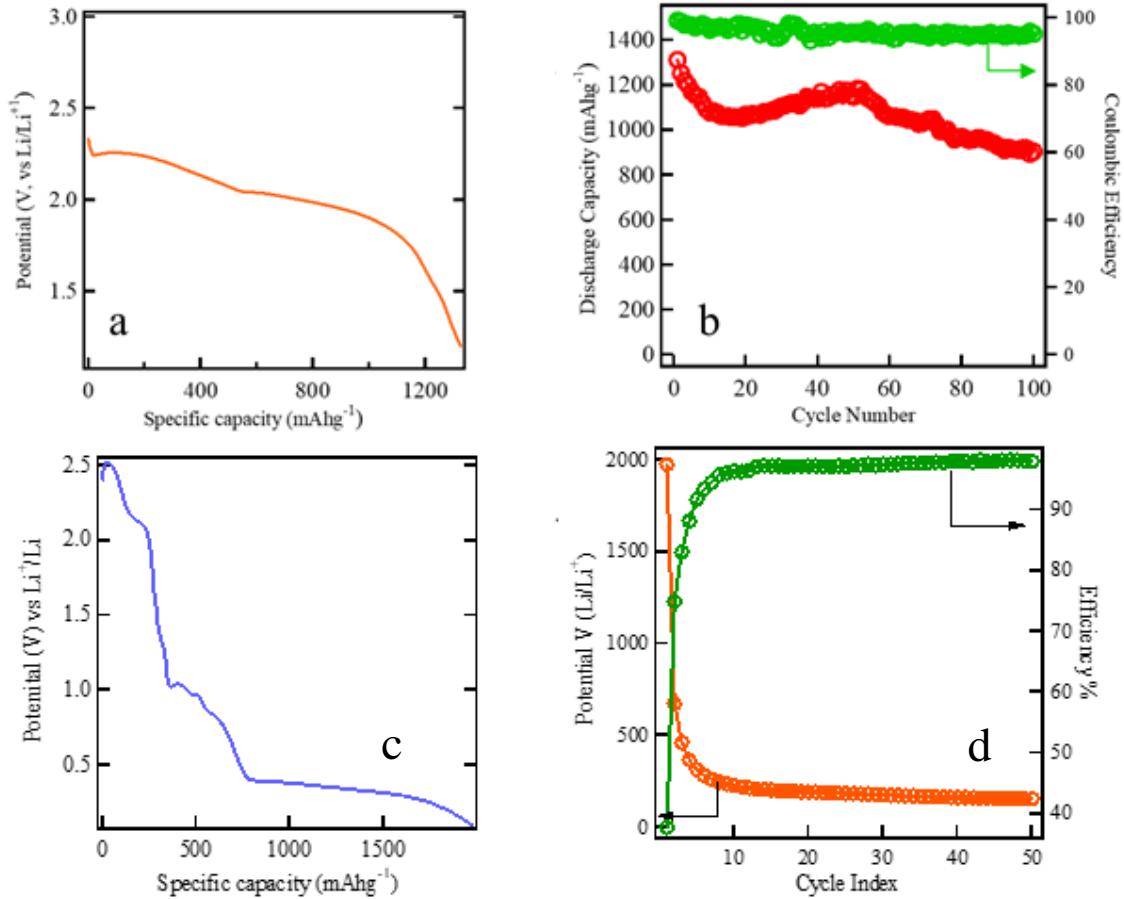


Figure 5.3. (a) Potential vs specific capacity curve of sulfur-Li half cell (first cycle) (b) Capacity retention and coulombic efficiency of sulfur-Li half cell (c) Potential vs specific capacity of α -MoO₃-Li half cell, (d) Capacity retention and coulombic efficiency of α -MoO₃-Li half-cell. (Half cells were cycled at C/3 current rate)

Fig. 5.3 shows the half-cell electrochemical performance of sulfur cathode (sulfur mixed with activated carbon and coated with mesoporous TiO₂) [112] and α -MoO₃ anode each against Li/Li⁺. The cathode shows capacity as high as 900 mAh/g even after 100 cycles at C/3 rate, but the anode capacity fades to ~300 mAh/g after 50 cycles. Sulfur cathode has

a potential of 2.4 V and fully lithiated α -MoO₃ (Li_{1.33}Mo_{0.66}O₂) has a potential of ~0.2 V, both versus Li/Li⁺. Therefore, a combination of these two electrodes will give an open circuit voltage of ~2.3 V.

High energy density pouch cell was also tested using Arbin battery tester. Fig. 5.4b and 5.4c show the performance of the pouch cell assembled from the respective cathode and anodes after the initial lithiation process. The pouch cell has a gravimetric capacity of 1500 mAh g⁻¹ at the first cycle and about 380 mAh g⁻¹ at the 50th cycle at C/3 rate. By looking at the specific capacity, it is apparent that, the Li-S battery with sulfur/carbon cathode and α -MoO₃ anode in the proposed pouch cell design renders a specific capacity greater than the available Li-ion technologies. The sulfur cathode which we used in this full cell was fabricated according to the same procedure described in Chapter 3 which shows a stable specific capacity over 900 mAh g⁻¹ over 100 cycles. However, the specific capacity of the full cell started to degrade and finally stabilized at 300 mAh g⁻¹. The reason for such capacity degradation could be due to the poor performances of the Li_{1.33}Mo_{0.66}O₂ anode which tend to stabilize ~ 300 mAh g⁻¹ as shown in Fig. 5.3d.

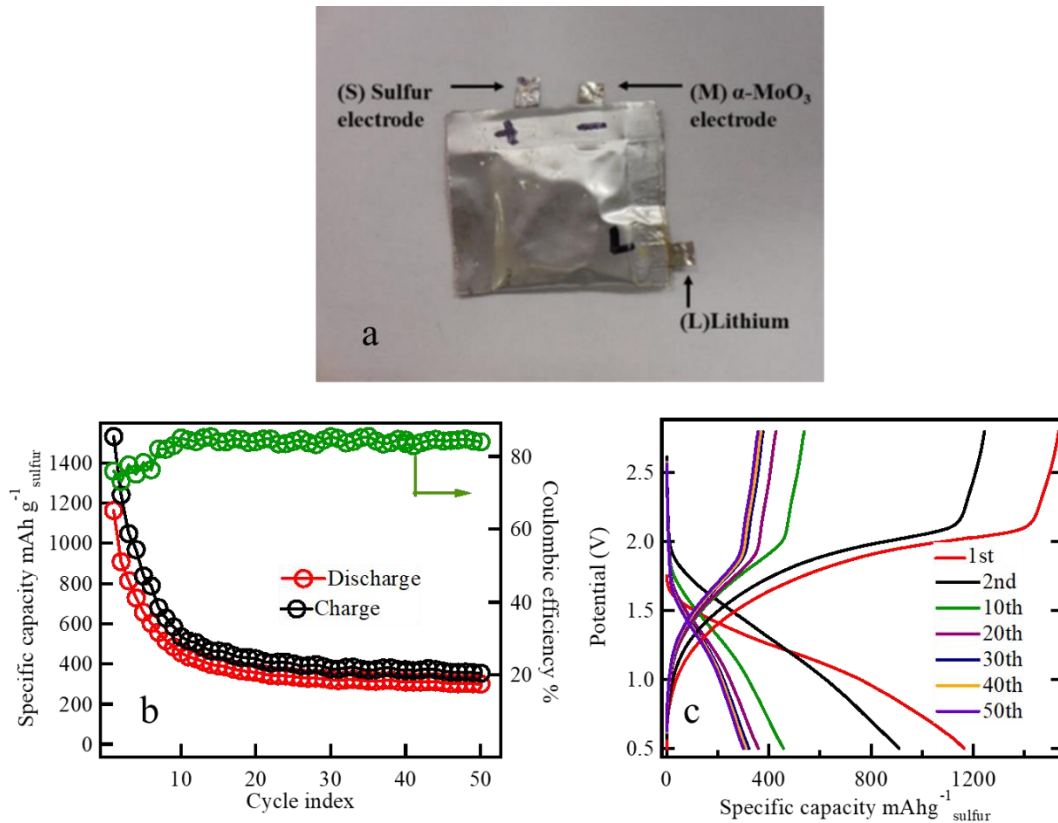


Figure 5.4. (a) lithium molybdate-sulfur pouch cell (b). Discharge capacity vs Cycle index (c) Potential vs specific capacity of S-Li_{1.33}Mo_{0.66}O₂ (c) Potential vs specific capacity curve for lithiating the α -MoO₃ (d) Specific capacity retention curve for α -MoO₃ vs Li/Li⁺

5.4 Capacity matching of cathode and anode

In half-cell evaluations, the capacity of the electrode of interest is calculated with respect to the reference electrode. For example, in Li-S batteries, the capacity of sulfur is calculated w.r.t lithium metal. In half-cells, capacity is limited by the maximum usable potential window between the cathode and the anode. However, the capacity matching determines the usable potential window. In laboratory, the electrode of interest is screened against a reference electrode which has excess of material. In this work Li metal serves as the

reference electrode. William R. Bennett [1] has published an article describing the capacity matching in full cells with details. Figure 5.5 shows a first three cycles of a typical Li-ion battery given in Ref[1].

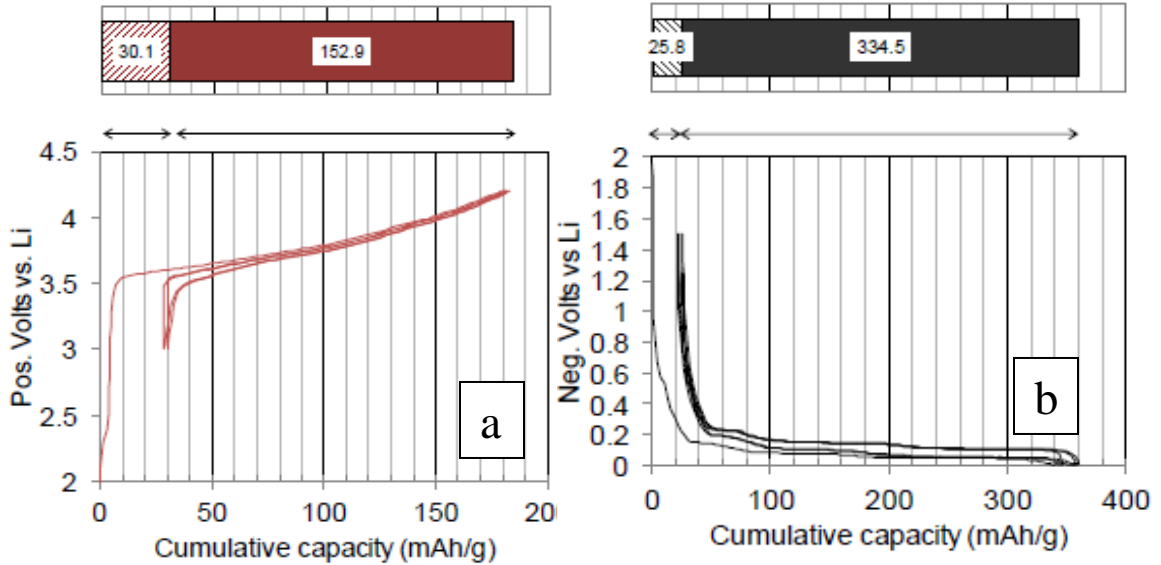


Figure 5.5. (a) charge capacity of positive electrode (b) charge capacity of negative electrode [1]

According to Fig 5.5, during de-lithiation, positive electrode becomes more electro positive while negative electrode and become electro-negative by accepting electrons. This process will be reversed on discharge. In a typical Li-ion cell, the first charge capacity is noticeably higher than the first discharge capacity. The difference between the first charging capacity and the first discharging capacity is called the irreversible capacity. The capacity loss in the irreversible region is due to various factors such as phase transitions in electrode materials, absorbance at solid electrolyte interface layer etc. The reversible capacity is the capacity available for the load after the cell is charged.

As per Fig. 5.5, following simple calculations show a total capacity of 183 mAh/g in the first cycle and a reversible capacity of 153 mAh/g, yielding a loss of 30 mAh/g in the irreversible region which amounts to about 19.7 % (30/153) of the reversible capacity.

Table 5.1 Specific capacity of electrodes in mAhg⁻¹ with reference to the capacity curves shown in figure 5.1 [1]

	Positive	Negative
Irreversibility	30.1	25.8
Reversibility	152.9	334.5
Total	183.0	360.3
Irreversibility	19.7%	7.7%

When a full cell is designed, capacities of apposing electrodes must be matched. Usually, electrodes need to have equal surface area and must exchange same capacity. In the above example of Li-ion full cell, the positive electrode is the Li⁺ source and the anode supposed to absorb the Li⁺ to surpass the irreversible capacity in SEI layer and for reversible capacity. Typically, Positive/negative ratio (P/N) is kept slightly lower than 1. By doing so, cell capacity is limited by the positive electrode and it will prevent lithium plating on the anode. When performing the capacity matching, gravimetric capacity of each electrode is irrelevant. What is important is Ah capacity of each electrode.

For the example given here, when mAhg⁻¹ capacity of given capacity is converted to Ah, the positive reversible capacity is 35 Ah. According the calculations, positive irreversible capacity is equal to 19.7 % of reversible capacity $19.7\% \times 35 \text{ Ah} = 6.90 \text{ Ah}$. Then the

total positive capacity needed in the positive electrode is 41.90 Ah. To limit the cell by positive electrode, 10% of extra capacity can be added to the negative electrode with P/N ratio becoming 0.909. Thus, negative electrode capacity will become 46.09 Ah. But there is an irreversible capacity of 7.7% in the negative electrodes too. Thus, effective reversible capacity will be 42.79 Ah. Table 5.2 and Fig. 5.6 summarizes the above calculations.

Table 5.2 Capacity values for baseline 35 Ah cell [1]

Capacity in Ah	Positive	Negative
Irreversible	6.90	3.30
Reversibility	35.00	42.79
Total	41.90	46.09
Irreversibility (% of rev)	19.7%	7.7%

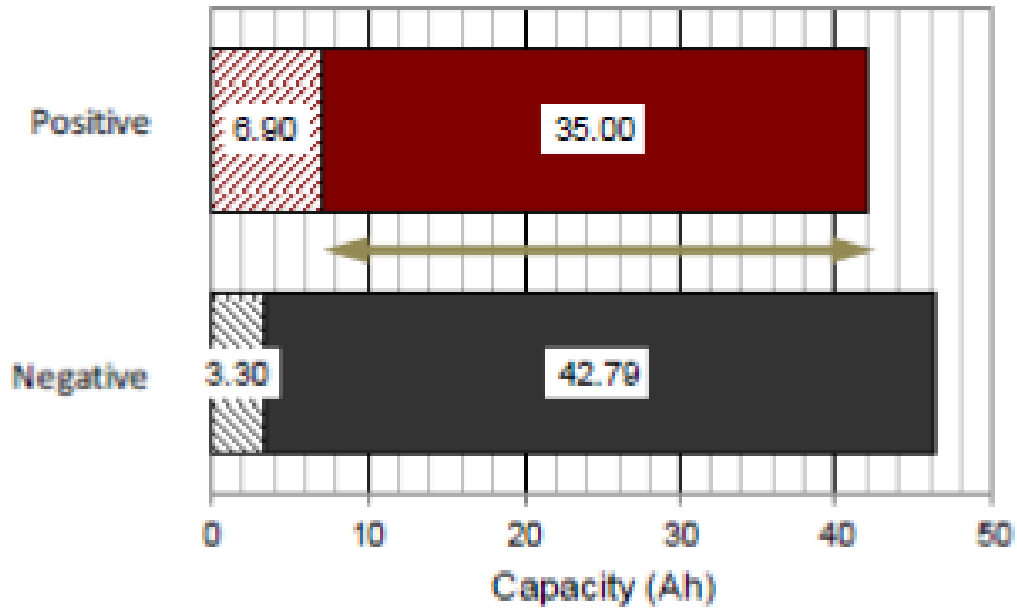


Figure 5.6. Capacity balancing in a hypothetical 35 Ah cell [1]

However, the capacity matching limits the usable potential window of the full cell. For example, the usable window of operation of the negative electrode is limited to 35 Ah according to the given example above. Thus, the negative electrode neither fully lithiates nor fully discharges.

The maximum state of charge for the anode; $\frac{6.90+35-3.30}{42.79} = 90.2\%$

Minimum state of charge for the anode; $\frac{6.90-3.30}{42.79} = 8.4\%$

Thus, the effective potential range for the anode is shown in Fig. 5.7

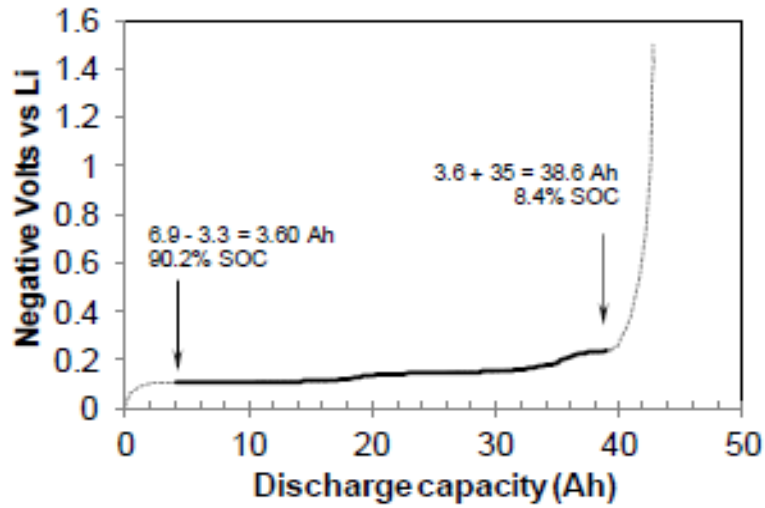


Figure 5.7. Effective potential range of the negative electrode [1]

After the capacity matching is calculated in Ah, the mass loading of each electrode can be calculated by dividing it by its specific capacity. Fig. 5.8 demonstrates the required mass loading given by the above example.

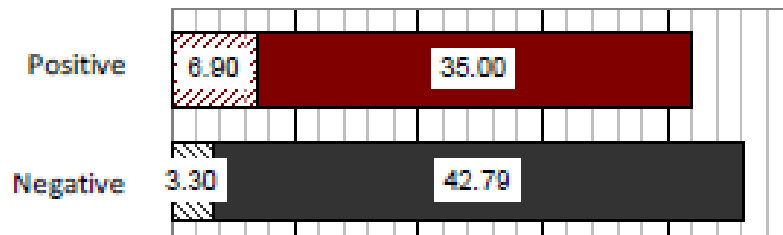


Figure 5.8. Ah capacity matching of positive electrode and negative electrode [1]

Table 5.3 Required mass loading calculation for the given example[1]

	Positive	Negative
Reversible capacity (Ah)	35.00	42.79
Specific capacity (mAh/g)	152.85	334.50
Active material (g)	229.00	127.90

5.5 Capacity retention and voltage profile improvement using MoO₃ nano-wires in anode formation

S-Li@MoO₃ full cells made using MoO₃ powder (particle size of 3 – 5 μm) show poor voltage stability and capacity loss. The root of the cause is perceived as due to the poor electrical conductivity of H₂ reduced MoO₃ powder. To improve the electronic properties of MoO₃, we proceeded to use α-MoO₃ nanowires. 1-dimensional semiconducting nanowire structures (metal oxides) typically demonstrate good electrical conductivity along their axes. The α-MoO₃ nanowires were synthesized by starting with thoroughly mixing MoO₂ and KCl (5:1 ratio). The mixture was then oxidized in air at 500 °C for 5 hours and then the sample was acid washed to remove any remaining potassium. The same conditions were applied during the subsequent H₂ reduction process as in α-MoO₃ powder preparation. The galvanometric capacity data of half-cells made of α-MoO₃ nanowire cathode and Li anode is shown in Fig. 5.9. Full cells are assembled in pouch cell format using the same technique for a targeted reversible capacity of 3 mAh. The cells were discharged and charged at the rate of C/10.

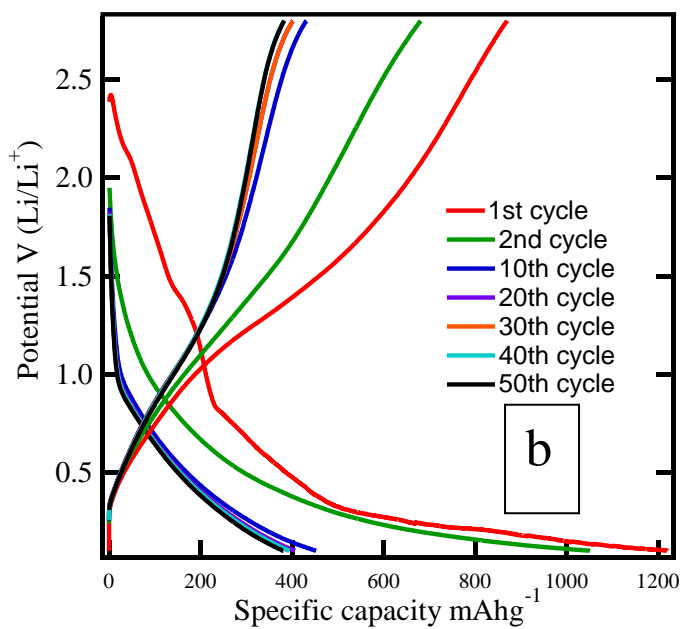
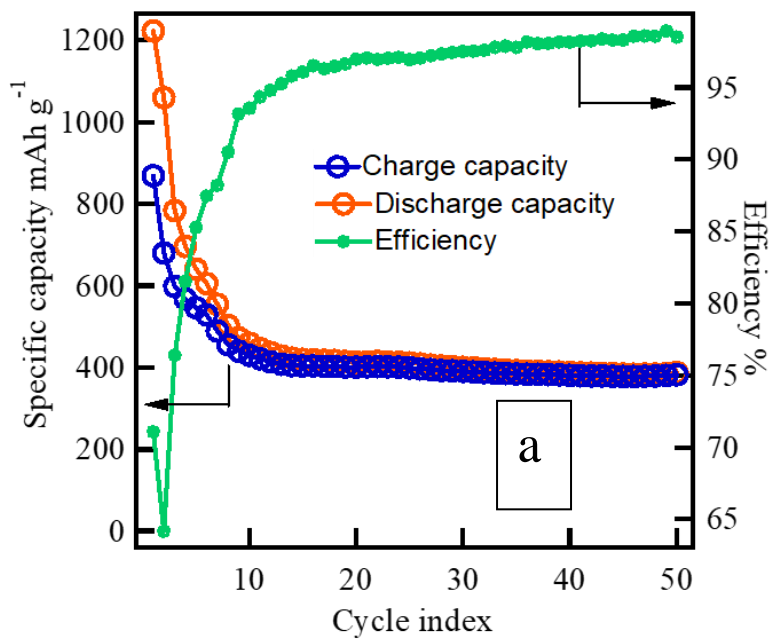


Figure 5.9. (a) charge/ discharge curves of α - MoO_3 nano-wire cathode and Li anode half cell (b) Potential vs specific capacity curves of α - MoO_3 (nano-wire)- Li half-cell. Testing were done at C/10 rate

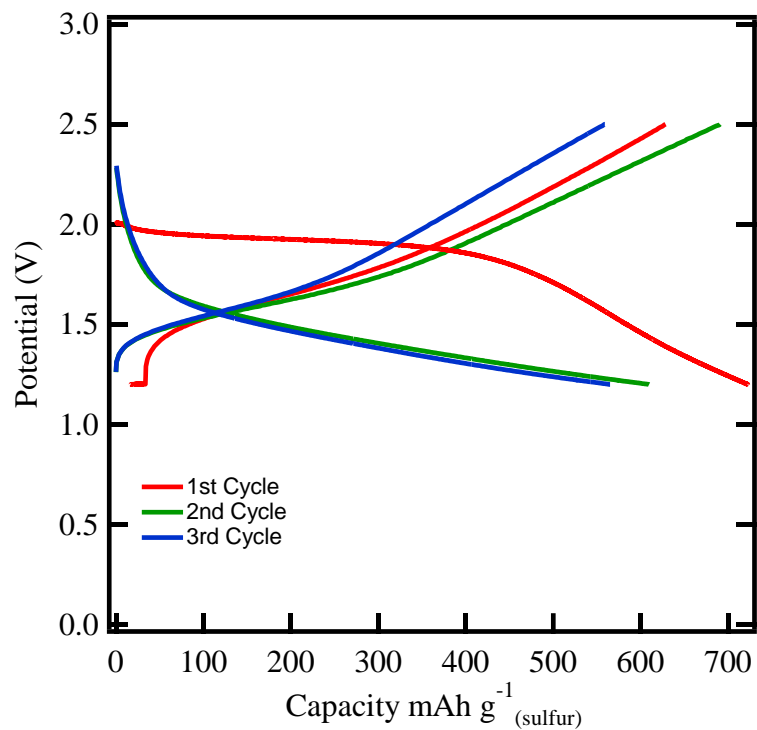


Figure 5.10. Potential vs specific capacity curves of S cathode and MoO₃ (nanowire) full cell (discharged at C/10).

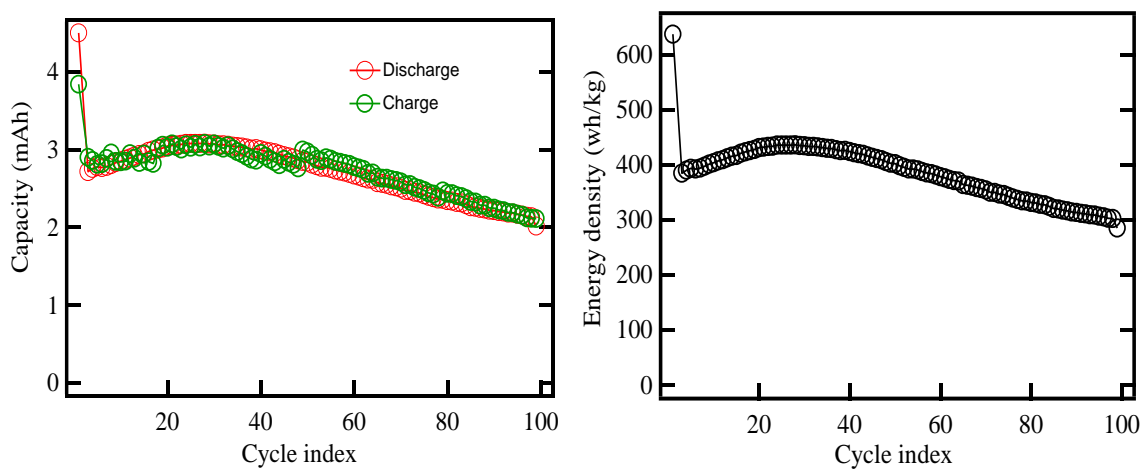


Figure 5.11. Capacity retention curves of S-Li@ α -MoO₃ (nanowire) full cell (a) mAh capacity vs cycle index (b) Energy density vs cycle index (discharged at C/10)

Use of MoO₃ nanowire has significantly improved the capacity retention and voltage stabilization over 50 cycles (Fig. 5.11). The capacity retention reached a value above 400 Whkg⁻¹ after 50th cycle which is quite promising. The stable capacity at 1.8 V at first cycle and 1.5 V after second cycle (Fig 5.10), makes this Li-S full cell technology is applicable in the electronic market where non-rechargeable 1.5 V alkaline batteries are commonly used.

5.6 Scale-up of sulfur cathode and α -MoO₃ anode formation

In Chapters 3 and 4, material synthesis for cathode and anode was described. Here, it is intended to describe a methodology to adapt previously described lab scale Li-S battery research into a large-scale Li-S battery fabrication process. The electrochemical performances were analyzed in laboratory scale and introduced simplified cathode and anode synthesis process to fabricate sulfur cathode and MoO₃ anode.

In Chapter 3, the methodology for fabricating mesoporous coated carbon/sulfur cathode was discussed. Specifically, the sulfur cathode electrode was dip-coated, mounted on a stainless-steel mesh and assembled in CR2032-coin cells. Scaling up of this method to fabricate high capacity pouch cell has couple of hurdles. First, sulfur/carbon composite electrode material must be modified so that carbon/sulfur composite can be coated on an Aluminum current collector. Secondly, the method of coating the mesoporous titania coating needs to be modified because the dip coating used is only applicable for smaller electrodes.

When synthesizing and fabricating the α -MoO₃ anode, 40% H₂/Ar was used to reduce the as prepared MoO₃. The purity of α -MoO₃ is needed to be improved in order to scale-up

the α -MoO₃ electrode fabrication process. The yield of pure α -MoO₃ material synthesis can be improved by using a mechanical vibrating method to thoroughly mix and homogenize MoO₃ (contained in a quartz boat) during the annealing process in the quartz reactor. Figure 5.12a shows a motor attached to the quartz tube to vibrate the MoO₃ sample uniformly. The synthesized material was further sonicated in de-ionized water to delaminate the layered α -MoO₃. This allowed the selective separation of orthorhombic α -MoO₃ and other non-layered MoO₃ phases.

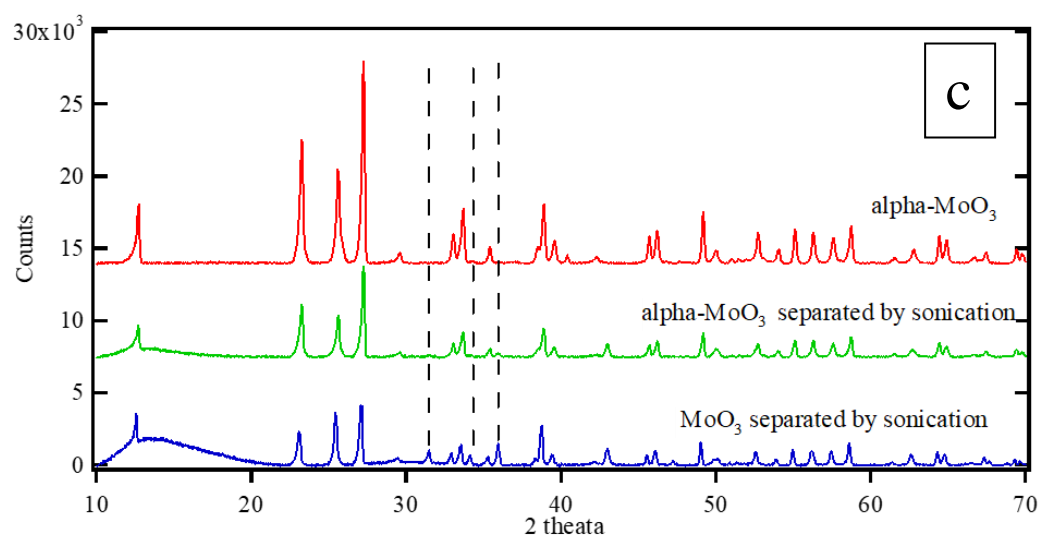
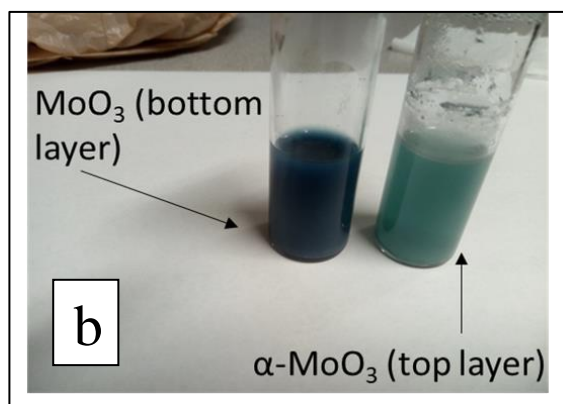
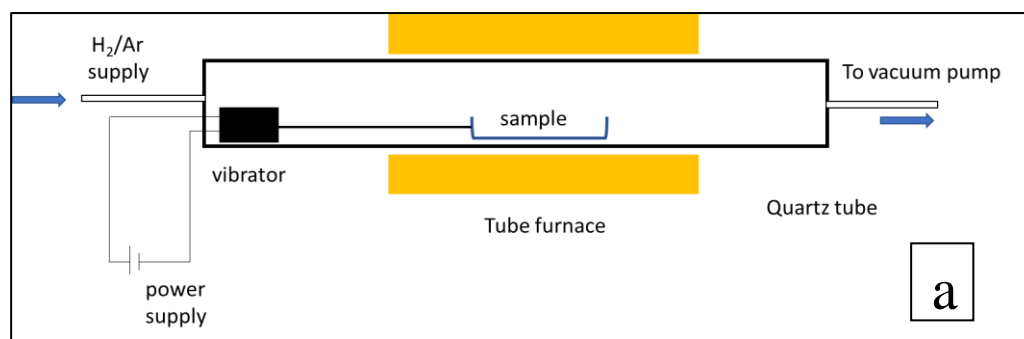


Figure 5.12. (a) vibrator attached to the sample holder to shake the sample for efficient reduction (b) Two samples after decanting (c) XRD spectrum comparison of two different MoO₃ samples separated by sonication and XRD of pure α- MoO₃ sample (red line)

5.7 Electrode formation and assembling of high energy density 1.5 V, 700 mAh Li-S pouch cell

A 700 mAh Li-S pouch cell is designed so that the capacity is limited by the sulfur cathode. The mass loading and the capacity matching is carefully done according to the following calculations based on the cathode and anode capacity curves shown in Fig. 5.13. Cathode being the limiting factor, calculations for electrode design must be started with the cathode mass loading.

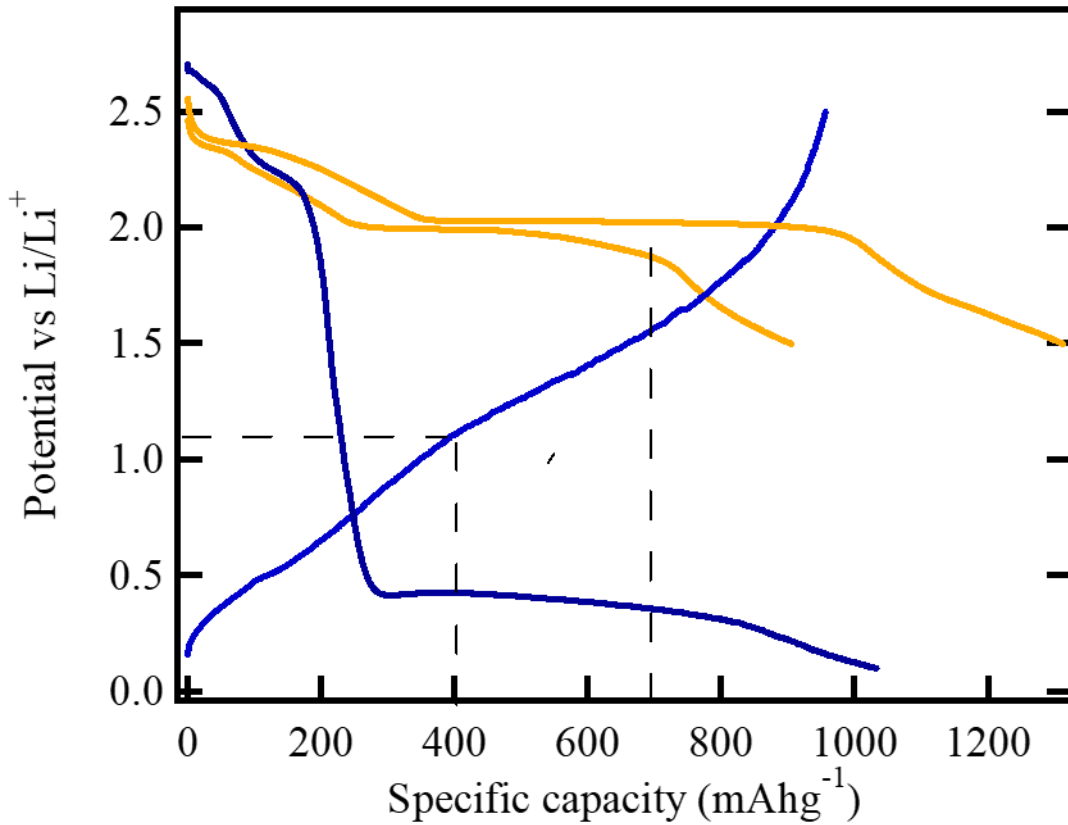


Figure 5.13. Capacity curves of sulfur cathode and α -MoO₃ anode

Data presented in Fig. 5.13 is extracted from half-cell charge-discharge curves of sulfur cathode (presented in Fig. 3.11b) and α -MoO₃ nanowire anode half-cell data (presented in

Fig. 5.9b). Sulfur electrode has an irreversible capacity of 400 mAhg⁻¹ and reversible capacity around 900 mAhg⁻¹. On the contrary, MoO₃ shows an irreversible capacity ~ 600 mAhg⁻¹ and a reversible capacity of ~ 400 mAhg⁻¹. Fig. 5.14a shows the comparison of reversible/irreversible capacities of cathode and anode in mAh g⁻¹. The mass loading is then calculated for the desired 0.7 Ah full cell by loading the anode material in such a way the positive (cathode) to negative (anode) mass ratio, P/N is 0.9. By doing so, cathode has less material compared to the anode, thus the cell capacity is limited by the cathode. Fig. 5.14b shows the Ah capacity matching which can eventually be able to convert to mass according to the table 5.4.

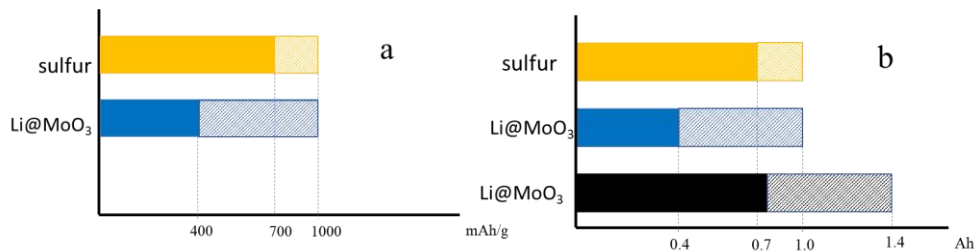


Fig 5.14. (a) Comparison of reversible and irreversible capacities of cathode and anode, (b) capacity matching for S-Li@MoO₃ full cell. (black line shows the capacity of MoO₃ required to have in the anode)

Table 5.4 Capacity matching and required mass loading for 700 mAh S-MoO₃ full cell

	Positive electrode	Negative electrode
Reversible capacity (Ah)	0.7	0.8
Specific capacity (mAhg ⁻¹)	700	400
Active material (g)	1.00	2.00
Required mass loading (including irreversible capacity) (g)	1.00	3.50

Cathode fabrication: 2 g of sulfur powder (3 μm- Sigma Aldrich) and 2 g of activated carbon (surface area ~ 1300 m²/g) are mixed for Sulfur content to become 50 %. The sulfur/carbon mixture is blended with 5% PVDF/NMP binder in such a way that the solid content percentage becomes 40 %. The slurry is prepared by mechanically mixing the sulfur/carbon and polymer mixture and filtering through a 100-mesh filter. The slurry is then coated on a 100 μm battery grade Aluminum foil (35 μm). A mesoporous titania coating is used as the polysulfide trapping agent. Anatase titania powder (3 – 5 μm) is homogenously sprinkled over the wet sulfur/carbon coating so that a thin layer of titania particles adhere on the coating while extra titania particles can be re-used. Then the titania/sulfur/carbon composite cathode is dried at 90 °C and calendared to achieve a 70 μm particle coating.

Anode formation: 1.5 g of α-MoO₃ is mixed with 70 mg of 3 – 5 μm silicon (Sigma Aldrich) and 135 mg of carbon. The final carbon composition was maintained to be ~ 10 %. The powder mixture is then mechanically mixed with 5% PVDF/NMP binder in such a way that the solid content percentage becomes 40 %. A copper foil is used as the anode

current collector and the slurry is coated to a thickness of 100 μm and subsequently calendared to achieve the thickness $\sim 80 \mu\text{m}$.

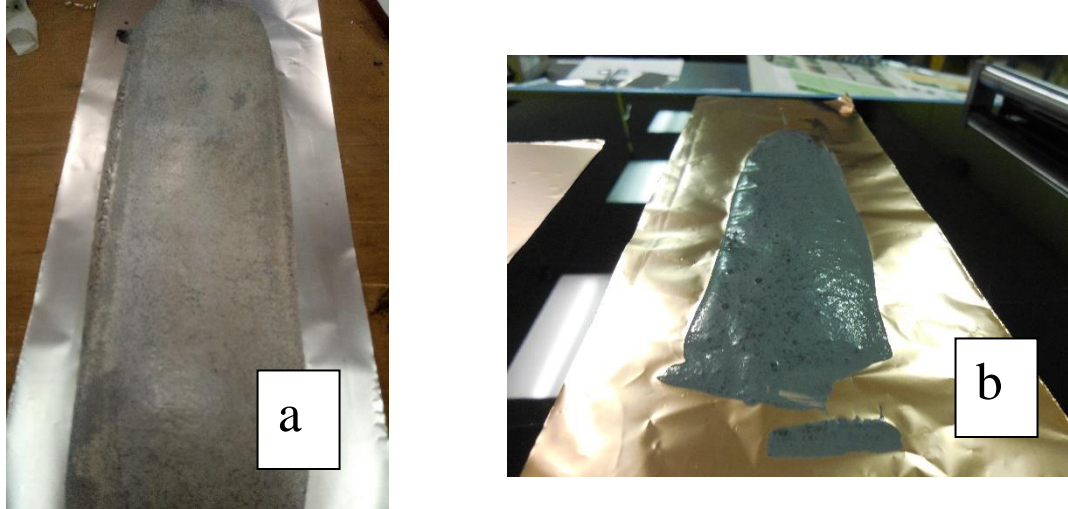


Figure 5.15. (a) Cathode coating on Aluminum (b) Anode coating on Copper

Cathode coating is designed to carry 4.2 mg cm^{-2} which will give $\sim 4 \text{ mAh}$, if 1000 mAhg^{-1} is the first cycle capacity. However, eventually the capacity of the cathode will drop to 2.8 mAh as the reversible capacity according to the capacity matching data shown in Fig. 5.14a and 5.14b. Then to make 700 mAh full cell, cathode material needs to be coated in an area of 175 cm^2 ($700 \text{ mAh} / 4 \text{ mAh cm}^{-2} = 175 \text{ cm}^2$).

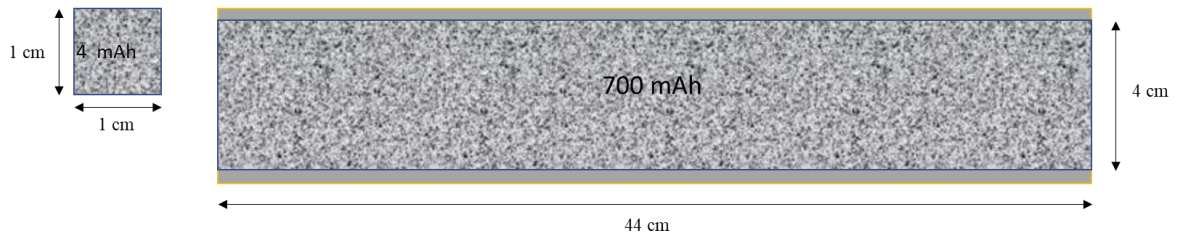


Figure 5.16. Schematics of cathode electrode

The α -MoO₃ coated copper foil must be coated to 5.6 mg cm⁻² to compensate the capacity of sulfur cathode including the irreversible capacity. Anode is coated with equal area of sulfur cathode.



Figure 5.17. Schematic of anode electrode

The Li-S full cell architecture consists of a lithium layer pressed onto a copper mesh to initiate the lithiation of the anode. In the intended 700 mAh pouch cell, 100 mesh copper cloth with wire diameter of 0.0045 inch was used with the lithium coating of ~ 2.00 mg cm⁻². The required lithium mass per area can be calculated by considering the amount of lithium required to compensate the irreversible capacity of MoO₃. Therefore, total lithium mass needed for 700 mAh battery is $1400 \text{ mAh} \div 3860 \text{ mAh g}^{-1} = 0.362 \text{ g}$. This requires a coating of $\sim 0.362 \text{ g}$ on a 175 cm² copper mesh resulting ~ 2.00 mg cm⁻². These three components are separated by polypropylene 25 μm celgard separator as shown in the pouch cell inside schematic and shown in Fig. 5.18a. Battery terminals are attached to the electrode by ultra-sonic spot welder. Al tab is spot welded to the cathode and Ni tab is spot welded to the anode and copper mesh before plating lithium. Then the assembling of the pouch cell is done in the Ar glove box. The assembling sequence include lithium plating on copper, electrode wrapping, inserting to laminated pouch, electrolyte filling and finally the sealing of pouch. 2 ml of 1 M LiTFSI (1:1 ratio of DOX:DME) is used as the electrolyte.

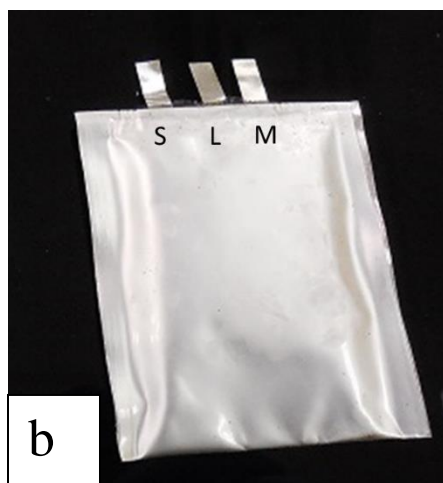
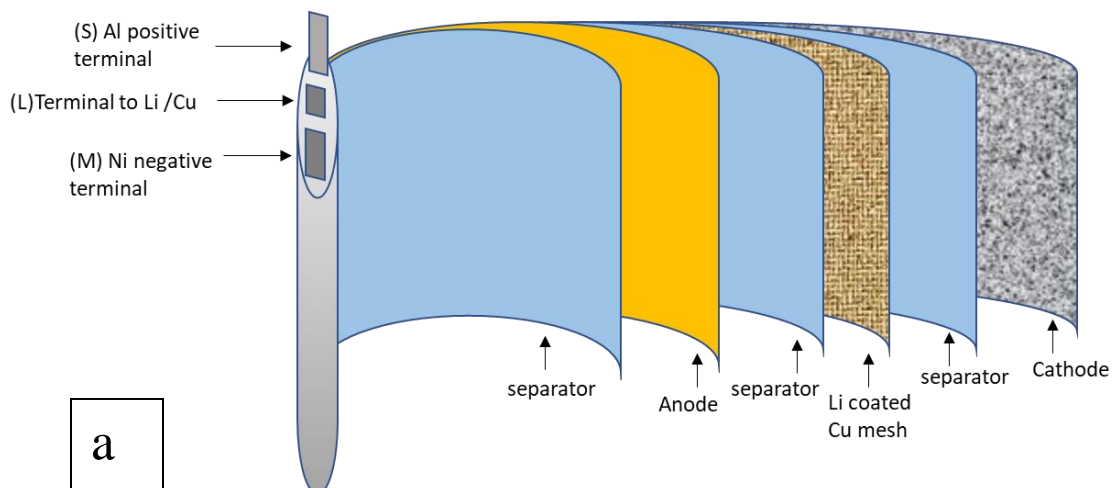


Figure 5.18. (a) internal schematic of Li- S pouch cell (b) external appearance of Li-S pouch cell (c) finished pouch cell after L terminal removed after lithiation

5.8 Conclusions

The major challenge of fabricating a Lithium metal free Li-S full cell using sulfur cathode and MoO_3 anode is the pre-lithiation process of MoO_3 . The attempted chemical and solvo-thermal based techniques led to the final product of Li_2MoO_4 which is unsuitable to be

used as the anode material in Li-S batteries since Mo is already at its highest oxidation state (+6). In contrary, electrochemical lithiation of α -MoO₃ produces Li_{1.33}Mo_{0.66}O₂. However, despite many attempts, we were unable to produce Li_{1.33}Mo_{0.66}O₂ using chemical or solvo-thermal methods. Our understanding is that formation of Li_{1.33}Mo_{0.66}O₂ requires an intercalation process which can be readily accomplished in an electrochemical process. Therefore, a novel cell design was introduced so that a Li-S battery could make in a single-step process. This is a unique and novel method that could potentially open the opportunity for scaling up of the production of lithium metal free Li-S batteries using sulfur cathode and pre-lithiated α -MoO₃ anode. S-Li@MoO₃ full cells were made using the α -MoO₃ micro-particles and nano-wires. α -MoO₃ nanowire-based Li-S were found to perform the best. Finally, it was able to fabricate S-Li@MoO₃ full cells with stable energy density exceeding 300 Wh kg⁻¹ over 100 cycles. Table 5.5 summarizes the specific energy densities of lithium molybdate-sulfur batteries made with α -MoO₃ anodes from different methods which were investigated in this dissertation. The specific energy density of state of-the-art Li-ion battery made by Tesla (2170) is also included in the table for comparison.

Table 5.5 Specific energy densities of lithium molybdate-sulfur batteries made with pre-lithiated α -MoO₃ from different synthesis techniques.

α -MoO ₃ powder (H ₂ reduction)	α -MoO ₃ powder (HWCVD)	α -MoO ₃ nano-wires (H ₂ reduction)	Li-ion Battery (Tesla 2170)
720 Wh kg ⁻¹ (1 st cycle)	540 Wh kg ⁻¹ (1 st cycle)	650 Wh kg ⁻¹ (1 st cycle)	—
180 Wh kg ⁻¹ (at 50 th cycle)	240 Wh kg ⁻¹ (at 50 th cycle)	400 Wh kg ⁻¹ (at 50 th cycle)	250 Wh kg ⁻¹

REFERENCES

1. R.Bennett, W., *Considerations for estimating electrode performance in Li-ion cells*.
2. Cristian Julien, A.M., Ashok Vijh, Karim Zaghib, *Lithium Batteries-Science and Technology* 2016.
3. David Linden, T.B.R., *Handbook Of Batteries* Mcgraw-Hill handbooks, 2001. **3rd edition**
4. Diebold, U., *The surface science of titanium dioxide*. surface science reports, 2003. **48**: p. 53-229.
5. Armand, J.-M.T.M., *issues challenges facing rechargeable lithium batteries*. nature, 2001. **414**: p. 359-367.
6. Zhang, S.S., *Liquid electrolyte lithium/sulfur battery: Fundamental chemistry, problems, and solutions*. Journal of Power Sources, 2013. **231**: p. 153-162.
7. Scheers, J., S. Fantini, and P. Johansson, *A review of electrolytes for lithium-sulphur batteries*. Journal of Power Sources, 2014. **255**: p. 204-218.
8. Amine, K., R. Kanno, and Y. Tzeng, *Rechargeable lithium batteries and beyond: Progress, challenges, and future directions*. MRS Bulletin, 2014. **39**(05): p. 395-401.
9. Martinez-Garcia, A., et al., *High rate and durable, binder free anode based on silicon loaded MoO₃ nanoplatelets*. Scientific Reports, 2015. **5**: p. 10530.
10. Andre, D., et al., *Future high-energy density anode materials from an automotive application perspective*. Journal of Materials Chemistry A, 2017. **5**(33): p. 17174-17198.
11. Yao, D.D., et al., *Electrodeposited α - and β -Phase MoO₃ Films and Investigation of Their Gasochromic Properties*. Crystal Growth & Design, 2012. **12**(4): p. 1865-1870.
12. Van Noorden, R., *The rechargeable revolution: A better battery*. Nature, 2014. **507**: p. 26-28.
13. Manthiram, A., et al., *Rechargeable lithium-sulfur batteries*. Chem Rev, 2014. **114**(23): p. 11751-87.
14. USDRIVE, *Electrochemical Energy Storage Technical Team Roadmap*. 2017.
15. Bruce, P.G., L.J. Hardwick, and K.M. Abraham, *Lithium-air and lithium-sulfur batteries*. MRS Bulletin, 2011. **36**(07): p. 506-512.
16. Bruce, P.G., et al., *Li-O₂ and Li-S batteries with high energy storage*. Nature Materials, 2012. **11**(1): p. 19-29.
17. Lu, J., et al., *Aprotic and aqueous Li-O(2) batteries*. Chem Rev, 2014. **114**(11): p. 5611-40.
18. Barchasz, C., et al., *Lithium/sulfur cell discharge mechanism: an original approach for intermediate species identification*. Anal Chem, 2012. **84**(9): p. 3973-80.
19. Yin, Y.X., et al., *Lithium-sulfur batteries: electrochemistry, materials, and prospects*. Angew Chem Int Ed Engl, 2013. **52**(50): p. 13186-200.
20. Mikhaylik, Y.V. and J.R. Akridge, *Polysulfide Shuttle Study in the Li/S Battery System*. Journal of The Electrochemical Society, 2004. **151**(11): p. A1969.
21. Xiao, J., et al., *Following the transient reactions in lithium-sulfur batteries using an in situ nuclear magnetic resonance technique*. Nano Lett, 2015. **15**(5): p. 3309-16.
22. Akridge, Y.V.M.a.J.R., *Polysulfide Shuttle Study in the LiS Battery System*. Journal of The Electrochemical Society, 2004. **11**: p. A1969-A1976.

23. Diao, Y., et al., *Shuttle phenomenon – The irreversible oxidation mechanism of sulfur active material in Li–S battery*. Journal of Power Sources, 2013. **235**: p. 181-186.
24. Park, J.-W., et al., *Solvent Effect of Room Temperature Ionic Liquids on Electrochemical Reactions in Lithium–Sulfur Batteries*. The Journal of Physical Chemistry C, 2013. **117**(9): p. 4431-4440.
25. Barchasz, C., et al., *Revisiting TEGDME/DIOX Binary Electrolytes for Lithium/Sulfur Batteries: Importance of Solvation Ability and Additives*. Journal of the Electrochemical Society, 2013. **160**(3): p. A430-A436.
26. Jozwiuk, A., et al., *The critical role of lithium nitrate in the gas evolution of lithium–sulfur batteries*. Energy Environ. Sci., 2016. **9**(8): p. 2603-2608.
27. Ma, L., et al., *Nanomaterials: Science and applications in the lithium–sulfur battery*. Nano Today, 2015. **10**(3): p. 315-338.
28. Li, X., et al., *Optimization of mesoporous carbon structures for lithium–sulfur battery applications*. Journal of Materials Chemistry, 2011. **21**(41): p. 16603.
29. Ma, G., et al., *Enhanced performance of lithium sulfur battery with polypyrrole warped mesoporous carbon/sulfur composite*. Journal of Power Sources, 2014. **254**: p. 353-359.
30. Helen, M., et al., *Single step transformation of sulphur to Li₂S₂/Li₂S in Li-S batteries*. Sci Rep, 2015. **5**: p. 12146.
31. Zhang, K., et al., *Synthesis of spherical porous carbon by spray pyrolysis and its application in Li-S batteries*. Journal of Solid State Electrochemistry, 2013. **17**(12): p. 3169-3175.
32. Xu, T., et al., *Mesoporous carbon-carbon nanotube-sulfur composite microspheres for high-areal-capacity lithium-sulfur battery cathodes*. ACS Appl Mater Interfaces, 2013. **5**(21): p. 11355-62.
33. Wang, N., et al., *In situ synthesized Li₂S@porous carbon cathode for graphite/Li₂S full cells using ether-based electrolyte*. Electrochimica Acta, 2017. **256**: p. 348-356.
34. Chen, S.-R., et al., *Ordered mesoporous carbon/sulfur nanocomposite of high performances as cathode for lithium–sulfur battery*. Electrochimica Acta, 2011. **56**(26): p. 9549-9555.
35. Wang, Z., et al., *A Metal–Organic Framework with Open Metal Sites for Enhanced Confinement of Sulfur and Lithium–Sulfur Battery of Long Cycling Life*. Crystal Growth & Design, 2013. **13**(11): p. 5116-5120.
36. Ding, B., et al., *Nanospace-confinement copolymerization strategy for encapsulating polymeric sulfur into porous carbon for lithium-sulfur batteries*. ACS Appl Mater Interfaces, 2015. **7**(21): p. 11165-71.
37. Lyu, Z., et al., *Hierarchical carbon nanocages confining high-loading sulfur for high-rate lithium–sulfur batteries*. Nano Energy, 2015. **12**: p. 657-665.
38. Ryu, H.S., et al., *Self-discharge characteristics of lithium/sulfur batteries using TEGDME liquid electrolyte*. Electrochimica Acta, 2006. **52**(4): p. 1563-1566.
39. Weiyang Li, G.Z., Yuan Yang, Zhe Wei Seh, Nian Liu and Yi Cui, *high performance hollow sulfur nanostructured battery cathode through a scalable room temperature one step bottom up approach*. Proceedings of the National Academy of Sciences of the United States of America, 2013. **110**: p. 7148-7153.
40. Wang, W.G., et al., *In situ sulfur deposition route to obtain sulfur–carbon composite cathodes for lithium–sulfur batteries*. J. Mater. Chem. A, 2014. **2**(12): p. 4316-4323.
41. Wang, D.-W., et al., *Carbon–sulfur composites for Li–S batteries: status and prospects*. Journal of Materials Chemistry A, 2013. **1**(33).
42. Chen, H., et al., *Ultrafine sulfur nanoparticles in conducting polymer shell as cathode materials for high performance lithium/sulfur batteries*. Sci Rep, 2013. **3**: p. 1910.

43. Nan, C., et al., *Durable carbon-coated Li₂(S) core-shell spheres for high performance lithium/sulfur cells*. J Am Chem Soc, 2014. **136**(12): p. 4659-63.
44. Wu, F., et al., *Graphene-Li₂S-Carbon Nanocomposite for Lithium-Sulfur Batteries*. ACS Nano, 2016. **10**(1): p. 1333-40.
45. Zhou, W., et al., *Yolk-shell structure of polyaniline-coated sulfur for lithium-sulfur batteries*. J Am Chem Soc, 2013. **135**(44): p. 16736-43.
46. Wei Seh, Z., et al., *Sulphur-TiO₂ yolk-shell nanoarchitecture with internal void space for long-cycle lithium-sulphur batteries*. Nat Commun, 2013. **4**: p. 1331.
47. Xiao, M., et al., *Sulfur@graphene oxide core-shell particles as a rechargeable lithium-sulfur battery cathode material with high cycling stability and capacity*. RSC Advances, 2013. **3**(15): p. 4914.
48. Dai, H., *Graphene-Wrapped Sulfur Particles as a Rechargeable Lithium Sulfur Battery Cathode Material with High Capacity and Cycling Stability*, in *acs*. 2011. p. 2644-2647.
49. Yongguang Zhang, Y.Z.a.Z.B., *A novel lithium sulfur battery based on sulfur graphene nanosheet composite cathode and gel polymer electrolyte*. Nanoscale Research Letters, 2014. **9**(137).
50. Xiao, M., et al., *Sulfur@graphene oxide core-shell particles as a rechargeable lithium-sulfur battery cathode material with high cycling stability and capacity*. RSC Advances, 2013. **3**(15).
51. Su, Y.S., Y. Fu, and A. Manthiram, *Self-weaving sulfur-carbon composite cathodes for high rate lithium-sulfur batteries*. Phys Chem Chem Phys, 2012. **14**(42): p. 14495-9.
52. Singhal, R., et al., *A free-standing carbon nanofiber interlayer for high-performance lithium-sulfur batteries*. J. Mater. Chem. A, 2015. **3**(8): p. 4530-4538.
53. Xu, G., et al., *Absorption mechanism of carbon-nanotube paper-titanium dioxide as a multifunctional barrier material for lithium-sulfur batteries*. Nano Research, 2015. **8**(9): p. 3066-3074.
54. Yan, J., et al., *Long-Life, High-Efficiency Lithium-Sulfur Battery from a Nanoassembled Cathode*. Chemistry of Materials, 2015. **27**(14): p. 5080-5087.
55. Sun, L., et al., *Sulfur nanocrystals confined in carbon nanotube network as a binder-free electrode for high-performance lithium sulfur batteries*. Nano Lett, 2014. **14**(7): p. 4044-9.
56. Xie, J., et al., *Preparation of three-dimensional hybrid nanostructure-encapsulated sulfur cathode for high-rate lithium sulfur batteries*. Journal of Power Sources, 2014. **253**: p. 55-63.
57. Singhal, R., et al., *A free-standing carbon nanofiber interlayer for high-performance lithium-sulfur batteries*. Journal of Materials Chemistry A, 2015. **3**(8): p. 4530-4538.
58. Song, M.K., Y. Zhang, and E.J. Cairns, *A long-life, high-rate lithium/sulfur cell: a multifaceted approach to enhancing cell performance*. Nano Lett, 2013. **13**(12): p. 5891-9.
59. Juilin Wang, J.Y., Jingying Xie and Naixin Xu, *A novel conductive Polymer-Sulfur composite cathode material for rechargeable Lithium batteries*. Advanced Material, 2002. **14**: p. 0935-9648.
60. Zhou, L., et al., *Binder-free phenyl sulfonated graphene/sulfur electrodes with excellent cyclability for lithium sulfur batteries*. Journal of Materials Chemistry A, 2014. **2**(14).
61. Ma, L., et al., *Enhanced Li-S Batteries Using Amine-Functionalized Carbon Nanotubes in the Cathode*. ACS Nano, 2016. **10**(1): p. 1050-9.
62. Zhang, S.S. and D.T. Tran, *How a gel polymer electrolyte affects performance of lithium/sulfur batteries*. Electrochimica Acta, 2013. **114**: p. 296-302.

63. Tatsumisago, M., M. Nagao, and A. Hayashi, *Recent development of sulfide solid electrolytes and interfacial modification for all-solid-state rechargeable lithium batteries*. Journal of Asian Ceramic Societies, 2013. **1**(1): p. 17-25.
64. Tian, H., et al., *High capacity group-IV elements (Si, Ge, Sn) based anodes for lithium-ion batteries*. Journal of Materiomics, 2015. **1**(3): p. 153-169.
65. Bordes, A., et al., *Investigation of Lithium Insertion Mechanisms of a Thin-Film Si Electrode by Coupling Time-of-Flight Secondary-Ion Mass Spectrometry, X-ray Photoelectron Spectroscopy, and Focused-Ion-Beam/SEM*. ACS Appl Mater Interfaces, 2015. **7**(50): p. 27853-62.
66. Xiuwan Li, Z.Y., Yujun Fu, Li Qiao, Dan Li, Hongwei Yue, and Deyan He, *Germanium Anode with Excellent Lithium Storage Performance in a Germanium LithiumCobalt Oxide Lithium Ion Battery*. acs nano, 2015. **9**: p. 1858–1867.
67. Liang, B., Y. Liu, and Y. Xu, *Silicon-based materials as high capacity anodes for next generation lithium ion batteries*. Journal of Power Sources, 2014. **267**: p. 469-490.
68. J.Sarradin, N.B., G. Taillades, M. Ribes, *Tin/tin oxide thin film electrodes for lithium ion batteries.pdf*. Journal of Power Sources, 2001: p. 208-210.
69. Kasavajjula, U., C. Wang, and A.J. Appleby, *Nano- and bulk-silicon-based insertion anodes for lithium-ion secondary cells*. Journal of Power Sources, 2007. **163**(2): p. 1003-1039.
70. Li, X., et al., *Mesoporous silicon sponge as an anti-pulverization structure for high-performance lithium-ion battery anodes*. Nat Commun, 2014. **5**: p. 4105.
71. Candace K. Chan, H.P., Gao Liu, Kevin MCilwrath, Xiao Feng Zhang, and R.A.H.a.Y. Cui, *High performance lithium battery anodes using silicon nano wires*. nature nanotechnology, 2007. **3**.
72. Nian Liu, L.H., Matthew T. McDowell, Ariel Jackson and Yi Cui, *Prelithiated Silicon Nanowires as an Anode for Lithium Ion Batteries*. acs nano, 2011. **5**: p. 6487–6493.
73. Praveen Meduri, C.P., Vivekanand Kumar, and a.M.K.S. Gamini U. Sumanasekera, *Hybrid Tin Oxide Nanowiires as Stable and High Capacity Anodes Li-Ion Batteries*. Nano Lett, American Chemical Society 2009. **9**(2): p. 612-616.
74. Blomgren, G.E., *The Development and Future of Lithium Ion Batteries*. Journal of The Electrochemical Society, 2016. **164**(1): p. A5019-A5025.
75. Zhao-Karger, Z., et al., *Toward Highly Reversible Magnesium–Sulfur Batteries with Efficient and Practical Mg[B(hfip)4]2 Electrolyte*. ACS Energy Letters, 2018. **3**(8): p. 2005-2013.
76. Goodenough, J.B. and Y. Kim, *Challenges for Rechargeable Li Batteries†*. Chemistry of Materials, 2010. **22**(3): p. 587-603.
77. Xu, K., *Nonaqueous Liquid Electrolytes for Lithium-Based Rechargeable Batteries*. Chem Rev, 2004. **104**: p. 4303-4417.
78. Jerry Foropoulos Jr., a.D.D.D., *Synthesis, properties, and reactions of bis((trifluoromethyl)sulfonyl) imide, (CF3SO2)2NH*. inorg. chem., 1984. **23**: p. 3720–3723.
79. Lee, D.J., et al., *Progress in lithium-sulfur batteries: the effective role of a polysulfide-added electrolyte as buffer to prevent cathode dissolution*. ChemSusChem, 2013. **6**(12): p. 2245-8.
80. Abraham, K.M., Z. Jiang, and B. Carroll, *Highly Conductive PEO-like Polymer Electrolytes*. Chemistry of Materials, 1997. **9**(9): p. 1978-1988.
81. Henderson, W.A., *Glyme–Lithium Salt Phase Behavior*. The Journal of Physical Chemistry B, 2006. **110**(26): p. 13177-13183.
82. Michel Armand, *The history of polymer electrolytes*. Solid State Ionics, 1994. **69**: p. 309-319.

83. Mikhaylik, Y.V., *Electrolytes for Lithium Sulfur Cells*,. US 7358012, 2008.
84. Aurbach, D., et al., *On the Surface Chemical Aspects of Very High Energy Density, Rechargeable Li-Sulfur Batteries*. Journal of The Electrochemical Society, 2009. **156**(8): p. A694-A702.
85. Demir-Cakan, R., et al., *Li-S batteries: simple approaches for superior performance*. Energy & Environmental Science, 2013. **6**(1).
86. Xiong, S., et al., *On the role of polysulfides for a stable solid electrolyte interphase on the lithium anode cycled in lithium-sulfur batteries*. Journal of Power Sources, 2013. **236**: p. 181-187.
87. B. A. Boukamp, G.C.L.a.R.A.H., *All solid lithium electrodes with mixed conductor matrix*. J. electrochemical society, 1981. **128**: p. 725.
88. Hu, R., et al., *Progress on Sn-based thin-film anode materials for lithium-ion batteries*. Chinese Science Bulletin, 2012. **57**(32): p. 4119-4130.
89. Hashem, A.M., et al., *Two-phase reaction mechanism during chemical lithium insertion into α -MoO₃*. Ionics, 2007. **13**(1): p. 3-8.
90. Mai, L.Q., et al., *Lithiated MoO₃ Nanobelts with Greatly Improved Performance for Lithium Batteries*. Advanced Materials, 2007. **19**(21): p. 3712-3716.
91. Weiyang Li, F.C., Zhanliang Tao, and Jun Chen, *vapor transportation preparation and reversible lithium intercalation deintercalation of alpha microrods*. Journal of Physical Chemistry, 2005. **110**: p. 119-124.
92. Sakaushi, K., et al., *Aqueous Solution Process for the Synthesis and Assembly of Nanostructured One-Dimensional α -MoO₃ Electrode Materials*. Chemistry of Materials, 2013. **25**(12): p. 2557-2563.
93. Brezesinski, T., et al., *Ordered mesoporous alpha-MoO₃ with iso-oriented nanocrystalline walls for thin-film pseudocapacitors*. Nat Mater, 2010. **9**(2): p. 146-51.
94. Hassan, M.F., et al., *Carbon-coated MoO₃ nanobelts as anode materials for lithium-ion batteries*. Journal of Power Sources, 2010. **195**(8): p. 2372-2376.
95. Meduri, P., et al., *MoO(3-x) nanowire arrays as stable and high-capacity anodes for lithium ion batteries*. Nano Lett, 2012. **12**(4): p. 1784-8.
96. Mikhailova, D., et al., *Lithium Insertion into Li₂MoO₄: Reversible Formation of (Li₃Mo)O₄ with a Disordered Rock-Salt Structure*. Chemistry of Materials, 2015. **27**(12): p. 4485-4492.
97. Scott Evers, T.Y., and Linda F. Nazar, *Understanding the Nature of Absorption/Adsorption in Nanoporous Polysulfide Sorbents for the Li-S Battery*. acs, 2012. **116**: p. 19653-19658.
98. Yang, Z.Z., et al., *Hierarchical TiO₂ spheres as highly efficient polysulfide host for lithium-sulfur batteries*. Sci Rep, 2016. **6**: p. 22990.
99. Yang, X., et al., *Mesoporous TiO₂ nanosheet with a large amount of exposed {001} facets as sulfur host for high-performance lithium-sulfur batteries*. Journal of Solid State Electrochemistry, 2016. **20**(8): p. 2161-2168.
100. Wang, H., et al., *TiO₂ coated three-dimensional hierarchically ordered porous sulfur electrode for the lithium/sulfur rechargeable batteries*. Energy, 2014. **75**: p. 597-602.
101. Kim, M.S., et al., *Multifunctional Separator Coatings for High-Performance Lithium-Sulfur Batteries*. Advanced Materials Interfaces, 2016. **3**(22).
102. Xu, Y., et al., *Nanocrystalline anatase TiO₂: a new anode material for rechargeable sodium ion batteries*. Chem Commun (Camb), 2013. **49**(79): p. 8973-5.
103. Heegemann, W., et al., *The adsorption of sulfur on the (100) and (111) faces of platinum; A LEED and AES study*. Surface Science, 1975. **49**(1): p. 161-180.
104. Gsell, M., P. Jakob, and D. Menzel, *Effect of Substrate Strain on Adsorption*. Science, 1998. **280**(5364): p. 717-720.

105. Zhang, S.S., *Role of LiNO₃ in rechargeable lithium/sulfur battery*. *Electrochimica Acta*, 2012. **70**: p. 344-348.
106. Wu, H.L., L.A. Huff, and A.A. Gewirth, *In situ Raman spectroscopy of sulfur speciation in lithium-sulfur batteries*. *ACS Appl Mater Interfaces*, 2015. **7**(3): p. 1709-19.
107. M. Hagen , E.Q.-G., S. Dörfler , G. Fahrer , J. Tübke , M.J. Hoffmann , and R.S. H. Althues, M. Krampfert, S. Kaskel, H. Föll *studies of preventing Li dendrite formation in Li-S batteries by using Si microwire anodes.pdf*. *Journal of Power Sources*, 2014. **248**: p. 1058-1066.
108. An, S.J., et al., *The state of understanding of the lithium-ion-battery graphite solid electrolyte interphase (SEI) and its relationship to formation cycling*. *Carbon*, 2016. **105**: p. 52-76.
109. Krause, A., et al., *High Area Capacity Lithium-Sulfur Full-cell Battery with Prelithiated Silicon Nanowire-Carbon Anodes for Long Cycling Stability*. *Sci Rep*, 2016. **6**: p. 27982.
110. Himendra Jha, I.B., Xueyin Cui, Stefano Meini,* and Hubert A. Gasteiger, <Li_S batteries with Li₂S cathodes and Si_C anodes.pdf>. *Journal of The Electrochemical Society*, 2015. **9**(A1829-A1835).
111. Yang, Y., et al., *New nanostructured Li₂S/silicon rechargeable battery with high specific energy*. *Nano Lett*, 2010. **10**(4): p. 1486-91.
112. Dharmasena, R., et al., *Mesoporous TiO₂ coating on carbon-sulfur cathode for high capacity Li-sulfur battery*. *RSC Advances*, 2018. **8**(21): p. 11622-11632.
113. Kasem, B.K.K. and S. Jones, *Platinum as a Reference Electrode in Electrochemical Measurements*. *Platinum Metals Review*, 2008. **52**(2): p. 100-106.

APPENDICES

Appendix 1:

A1 Half-cell electrochemical characteristics of CMF based sulfur cathode

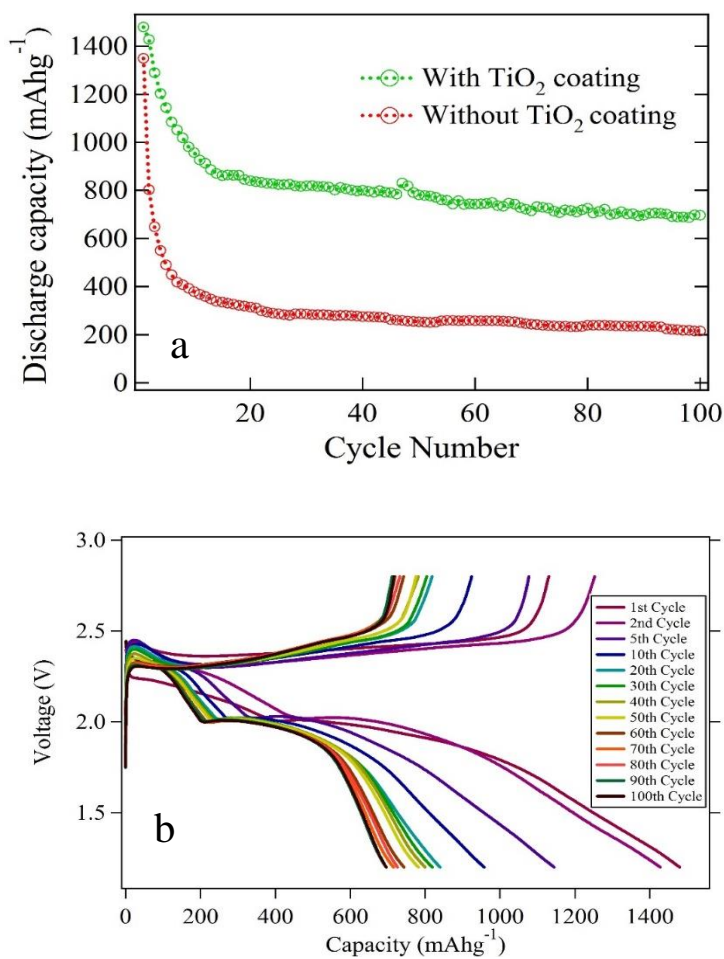


Figure 1. (a) Discharge capacity retention of sulfur cathode made of carbonized microfiber (b) potential vs specific capacity curves of the same sulfur cathode

Appendix 2:

A2.1 Half-cell electrochemical characteristics of HWCVD deposited α -MoO₃ vs

Lithium

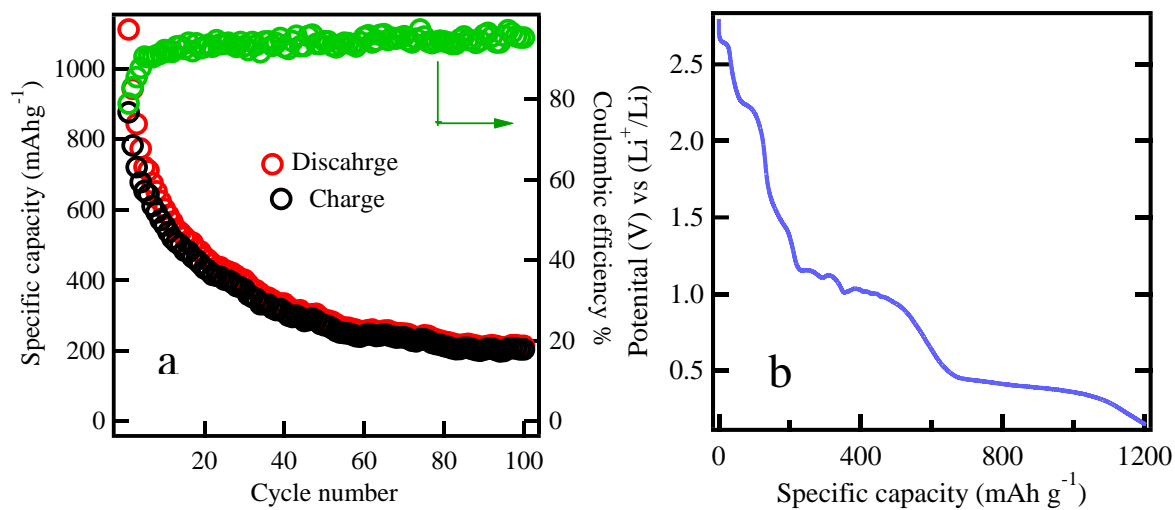


Figure 2 (a) Specific capacity vs cycle index (b) Discharge curve of electrochemically lithiated α -MoO₃ synthesized by HFCVD technique

A2.2 Half-cell electrochemical characteristics α -MoO₃ powder vs Lithium

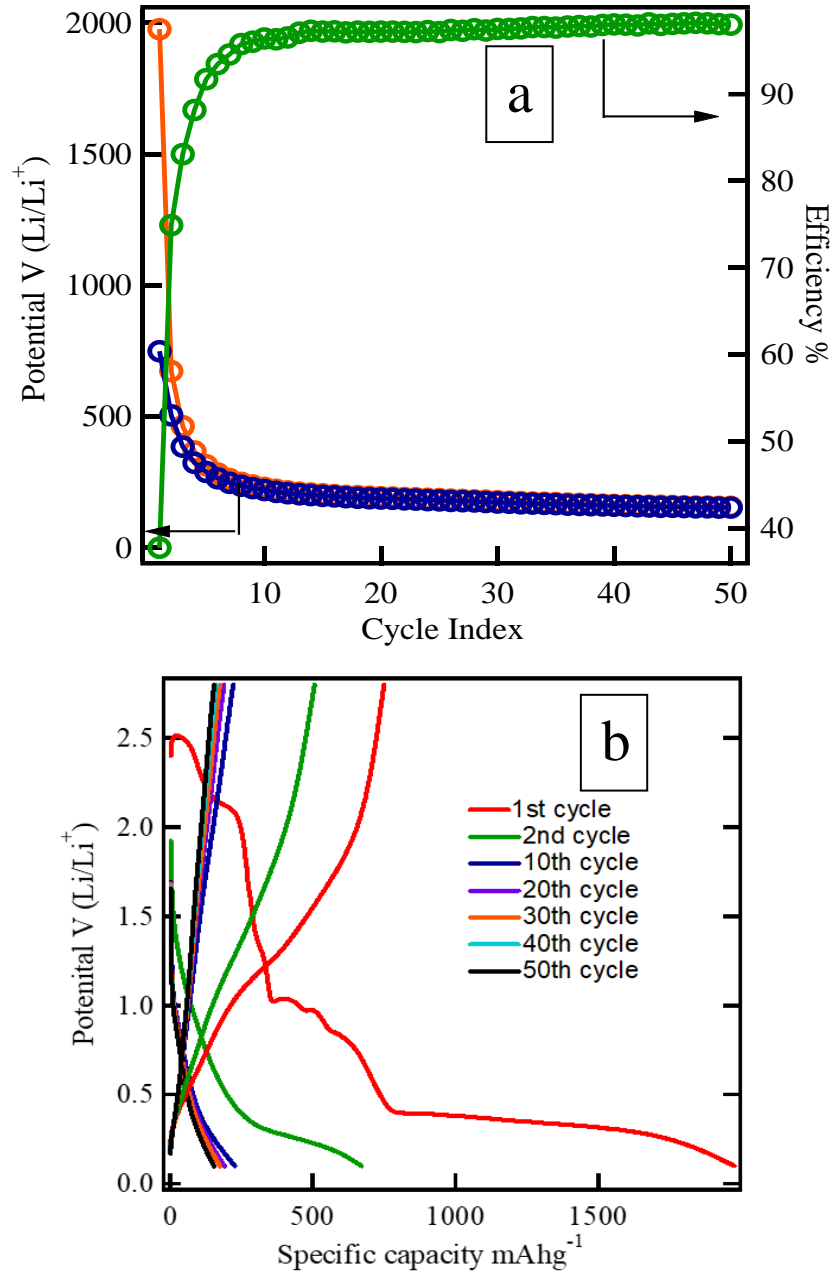


Figure 3 (a) charge/ discharge curves of α -MoO₃ micro particles cathode and Li anode half cell (b) Potential vs specific capacity curves of α -MoO₃- Li half-cell. Testing were done at C/10 rate.

Appendix 3:

A3.1 Electronic and optical properties of MoO₃

MoO₃ is known to be a n type semiconductor with a band gap of ~3.1 eV. The influence of α -MoO₃ subjected to controlled reduction in 40% H₂/Ar at 400 °C was significantly apparent as seen in the electrochemical performance described previously. Therefore, it is important to understand, how the electronic properties change in as prepared MoO₃ (mixture of α -MoO₃ and β -MoO₃) and after being reduced to α -MoO₃. The electrical and optical properties of pristine MoO₃ and final α -MoO₃ were studied using two different techniques; *ex-situ* UV-absorption and *in-situ* four probe conductivity measurement technique.

A3.2 Optical Properties of MoO₃ using UV absorption technique

MoO₃ is known for its n type semiconductor properties with a band gap of ~3.1 eV. In this work however, it was important to understand the optical properties, e.g., dependence of the band gap of the as prepared MoO₃ after reduction (presumably converting to α -MoO₃). The absorption spectra (Fig. 4) were obtained by Perkin-Elmer Lambda 950 UV- VIS spectrometer. To prepare the samples for optical measurements, a small portion of (i) MoO₃ material from as prepared MoO₃ powder, (ii) reduced α -MoO₃, (iii) as prepared MoO₃ nanowire and (iv) reduced α -MoO₃ were dissolved in ethanol and coated on glass slides. The spectrum was obtained from 200 nm to 800 nm visible range. Then $(\alpha h\nu)^{1/2}$ was plotted as a function of photon energy $h\nu$ (Tauc plot). Then the optical band gap E_g was determined using the linear range near the absorption edge, i.e., $\alpha > 10^{-4} \text{ cm}^{-1}$ (5). By extrapolating linearly to $(\alpha h\nu)^{1/2} = 0$, E_g was estimated as the x-axis intercept.

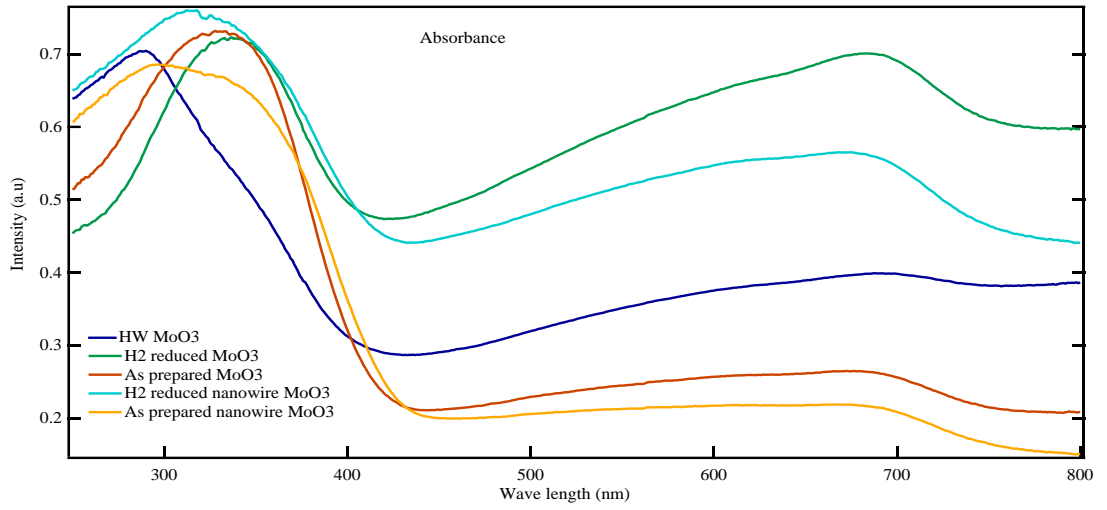


Figure 4. UV-VIS Absorbance spectrums of MoO₃ samples of different morphologies

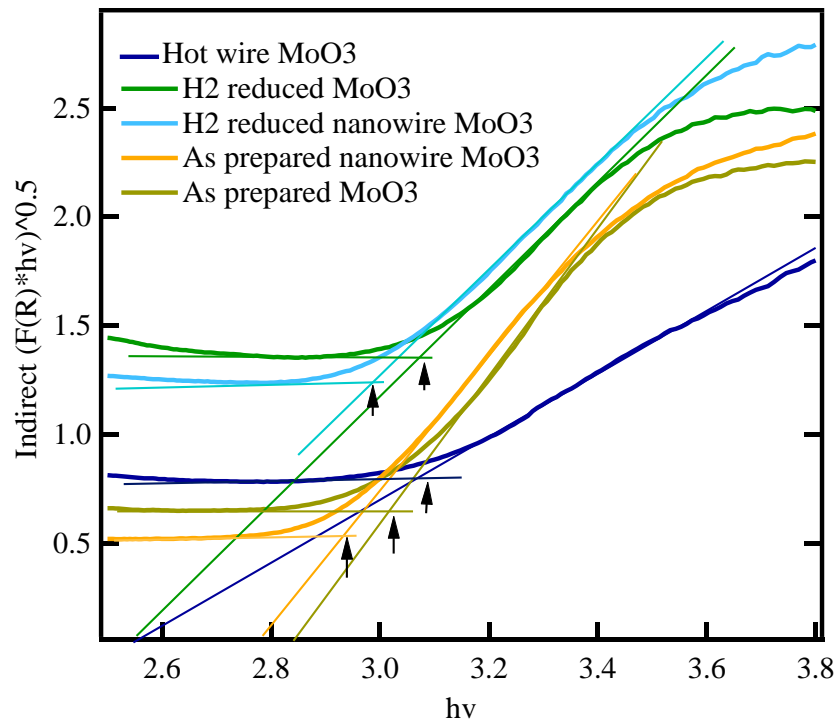


Figure 5. Tauc plots of MoO₃ samples with different morphologies

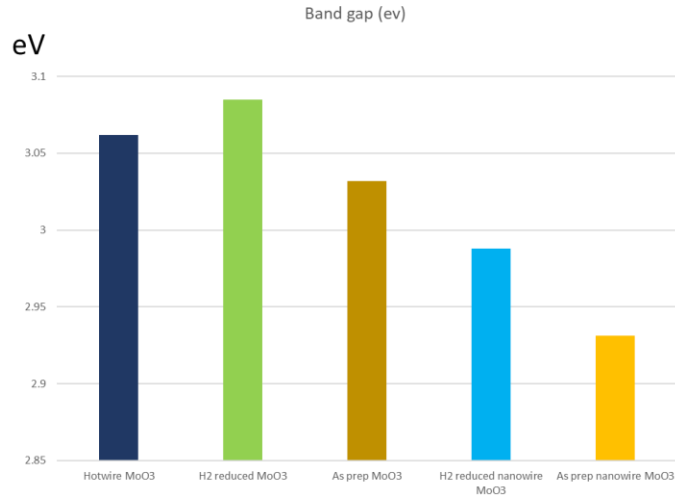


Figure 6. Comparison of band gap of different MoO₃ samples

The results obtained from the Tauc plots indicates a small increase in the optical band gap E_g of as prepared MoO₃ after reduction. The increase is however insignificant as shown in Fig. 6. Interestingly, α -MoO₃ synthesized via HWCVD technique having an energy band gap of 3.05 eV shows a small decrease down to 2.9 eV after H₂ reduction, still an insignificant change.

Appendix 4

A4.1 Electronic properties of α -MoO₃ using four probes technique

The transition from β -MoO₃ to layered α -MoO₃ seems to have a significant influence on the lithiation capacity of MoO₃. However, it is uncertain whether the electronic properties of layered structures influence more in improving the capacity of MoO₃. To understand this phenomenon, change in electronic properties were investigated using *in-situ*, four probes electrical conductivity testing.

MoO₃ particles and nanowires were subjected controlled reduction causing them to undergo transformation from β -MoO₃ to α -MoO₃. First, 20 mg of each material was pressed to form a thin 7 mm diameter circular pellet. The pellets were then mounted on the sample mount of an electrical measurement probe which will be placed inside a quartz tube as shown in Fig. 7c. The quartz reactor has the provisions for evacuation, purging with 40 % H₂/Ar and heated in a tube furnace as shown in Fig. 7c.

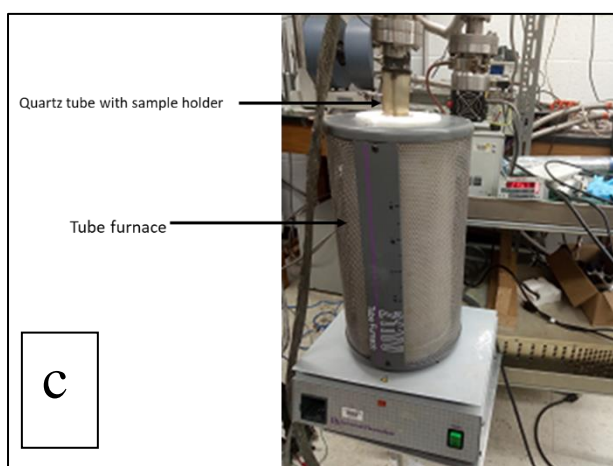
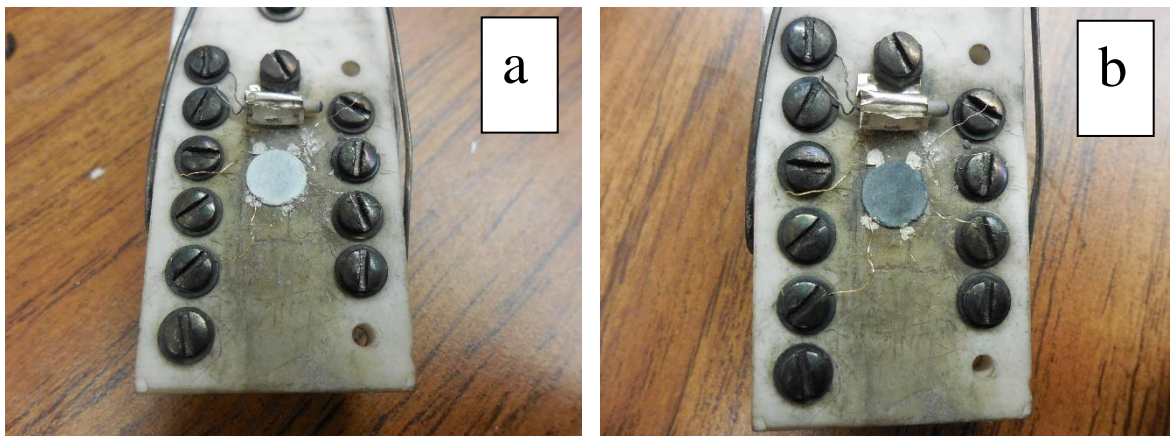


Figure 7. (a) as prepared β - MoO_3 pellet mounted on a chip carrier (b) After the pellet has been reduced to α - MoO_3 (c) Heating system for α - MoO_3 setup

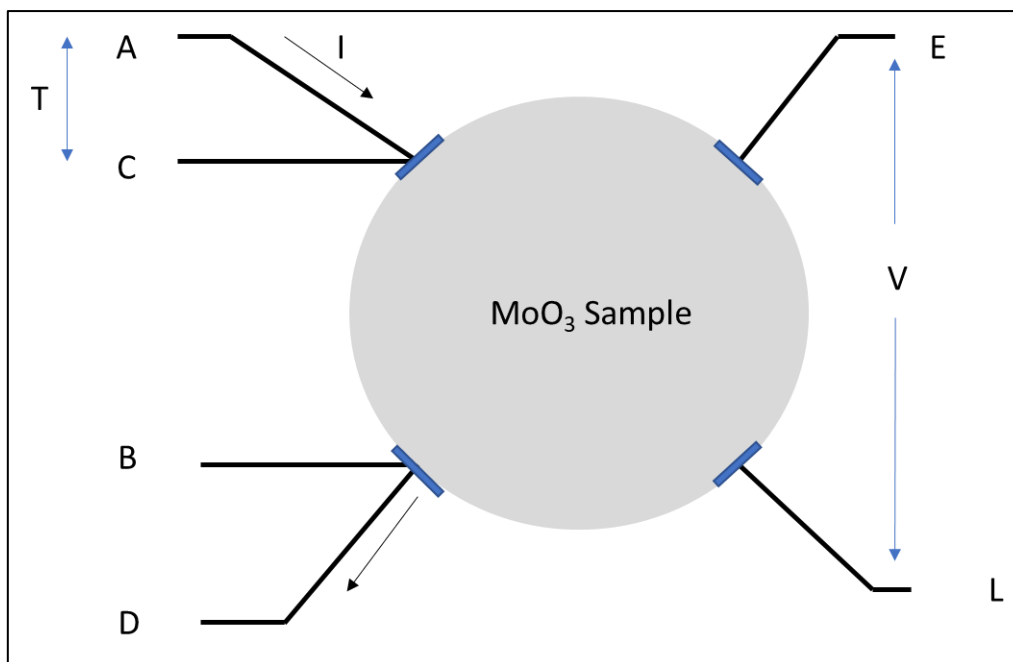


Figure 8. Schematic of contacts for 4 probes conductivity testing

In order to measure the electronic properties *in-situ*, technique, four contacts were made on the pellet using silver epoxy as shown in Fig. 8. The current and voltage was measure using a Keithley 2182 picoammeter while the temperature was measured using a thermocouple monitored using Fluke 8842A multimeter. First, the quartz chamber which hoses the probe containing the sample was vacuumed down to 75 mtorr. Next, the temperature was increased from room temperature to 300 °C, while monitoring the resistance with the temperature. When the system reached 300 °C, 40% H₂/Ar is introduced to a pressure of 300 mtorr and kept the pressure and temperature constant for 2 hours while monitoring the time dependence of the resistance. Then the system was cooled down to room temperature still monitoring the resistance as a function of temperature. Fig. 9 shows time dependence of the resistance (left axis) and the temperature (right axis) for MoO₃ particle and nanowire pellets.

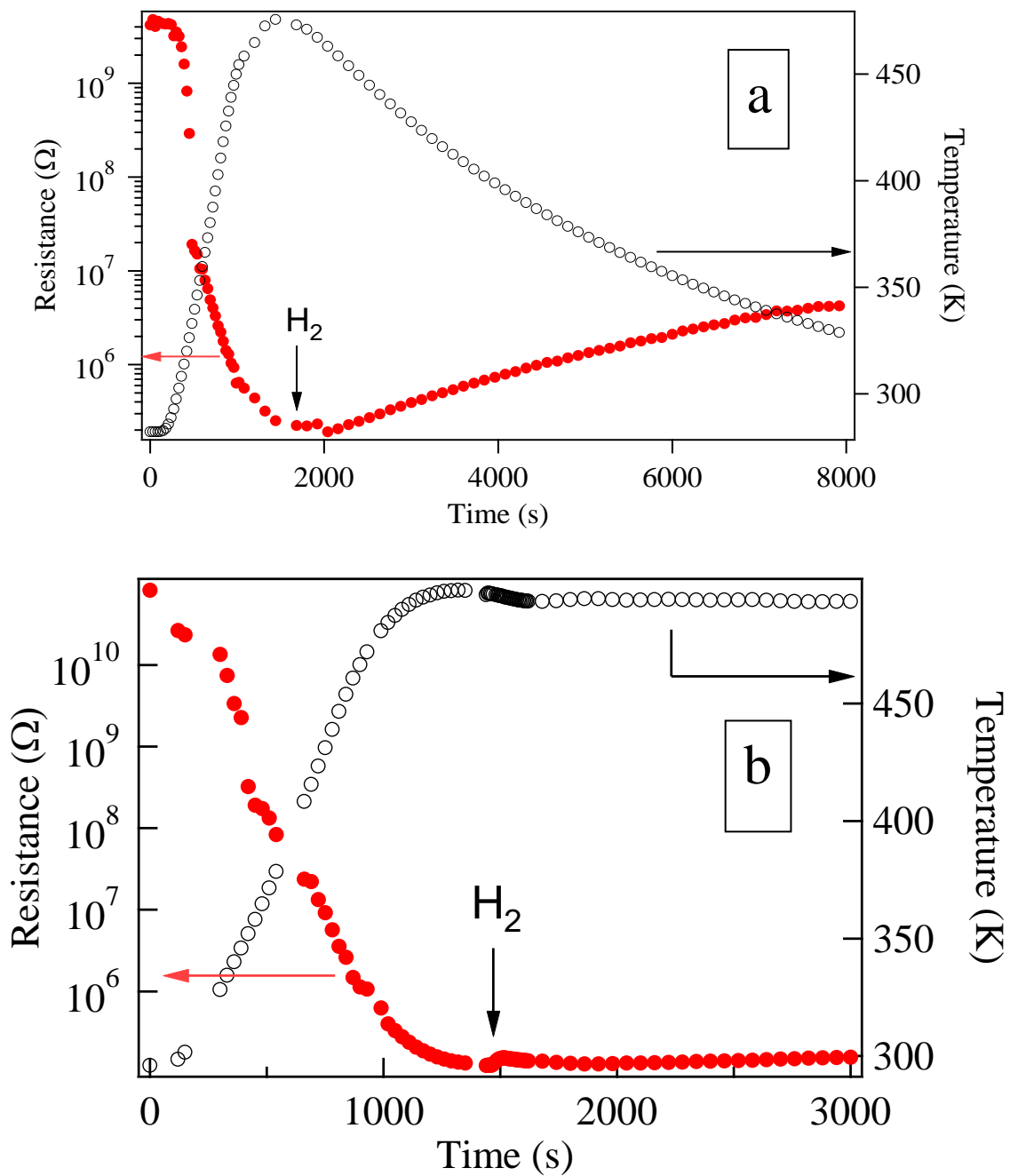


Figure 9. Dependence of resistance on temperature and H_2 reduction (a) Resistance of MoO_3 particles (b) Resistance of MoO_3 nanowire

The resistance drop with temperature is similar in both case as shown in Fig. 9a and 9b. The resistance drop with temperature is expected for a semiconductor as more electrons are available in the conduction band as the temperature rises. However, the observation of resistance change during the phase change is the goal of this experiment. It was found that, the resistance increases at the instance of the H₂ introduction. At this point the temperature was maintained at 300 °C. After the system was cooled down, an order of magnitude (10²-10³ ohms) change of the resistance was observed, which is a significant improvement of the electrical conductivity due to the reduction process

Appendix 5

A5.1 Effect of the lithiation on the Charge Transfer Resistance of α -MoO₃

In this section, the influence of lithiation (Li doping instead of hydrogen) on the electronic properties is investigated using the electrochemical impedance technique (EIS). The experiment was carried out using a three electrodes cell, keeping α -MoO₃ as the working electrode, lithium as the counter electrode as well as the reference electrode. Biologic SP-200 potentiostat was used to study the EIS in the range of 1 MHz to 1 mHz.

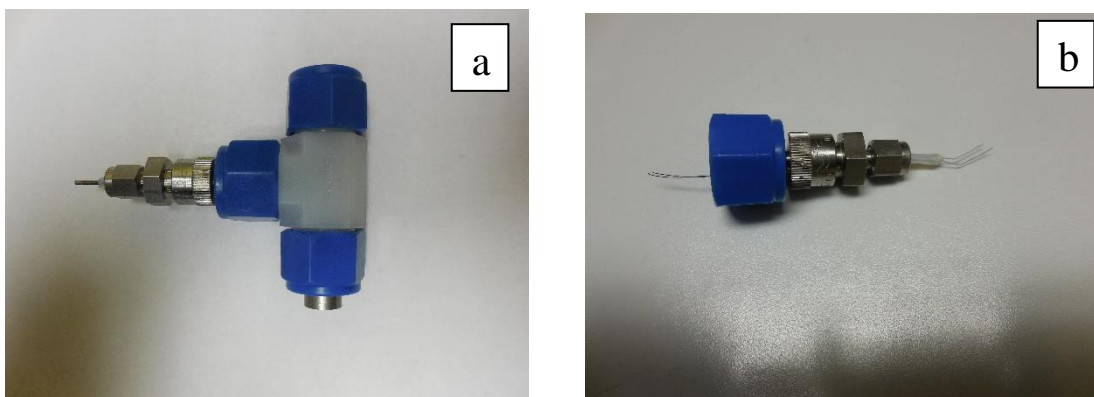


Figure 10. (a) three electrode Swagelok cell prepared impedance measurements (b) custom made reference electrode

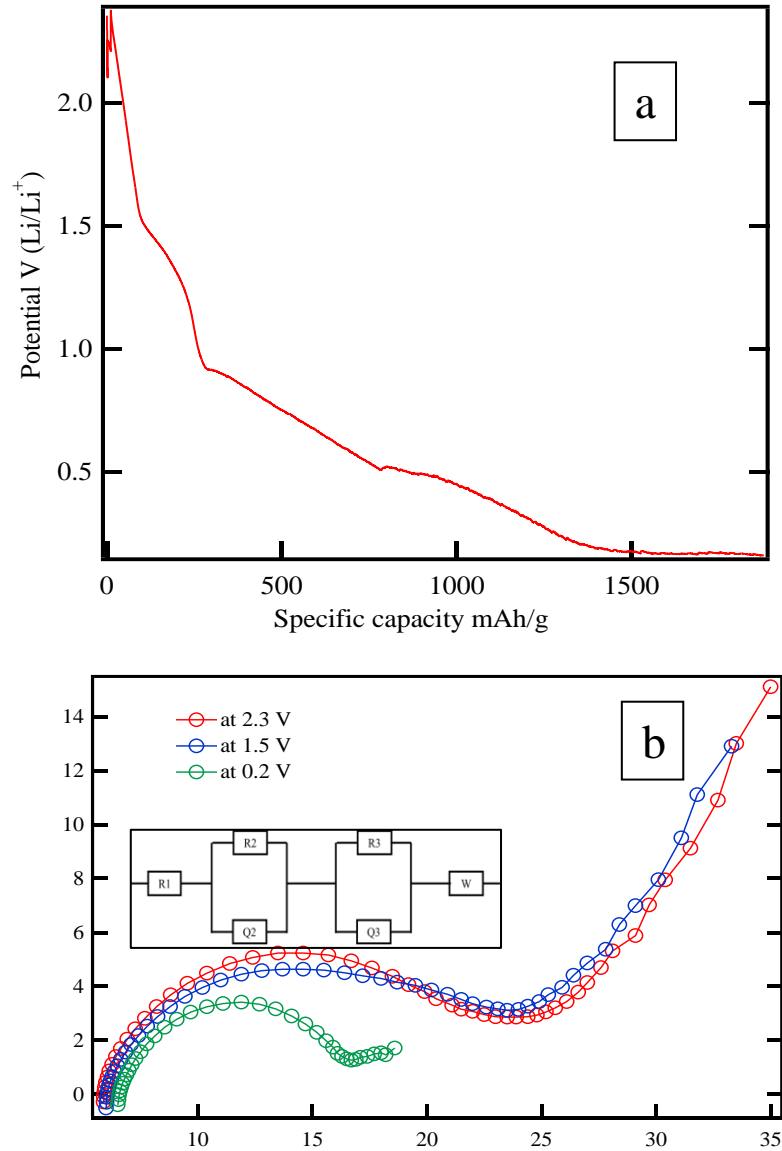


Figure 11. (a) Discharge curve of α -MoO₃. Cell was disconnected at 2.3 V, 1.5 V and 0.2 V for impedance testing (b) Nyquist plots at different depth of discharge

Table 1. Fitted resistor values of Nyquist plots shown in Fig. 11b. R1 is electrolyte resistance, R2 is charge transfer resistance and R3 is the interface resistance.

Potential	R1 (Ω)	R2 (Ω)	R3 (Ω)
2.3 V	5.87	7.078	10.14
1.5 V	5.99	8.98	10.54
0.2 V	6.55	2.99×10^{-8}	10.02

EIS testing was carried out at three different potentials along the discharging curve shown in Fig. 11a. In the Nyquist plots there is a clear drop of charge transfer resistance at 0.2 V, where it is lithiated to $\text{Li}_{1.33}\text{Mo}_{0.66}\text{O}_2$. The Nyquist plots were fitted using equivalent circuit model shown in Fig. 11b inset. In addition, two probe EIS was conducted on $\alpha\text{-MoO}_3$ synthesized from hot wire CVD technique before and after reduction with 40% H_2/Ar . Fig. 12 shows the a/c impedance carried for all three samples. It is apparent that, $\alpha\text{-MoO}_3$ synthesized by hot wire technique has higher conductivity.

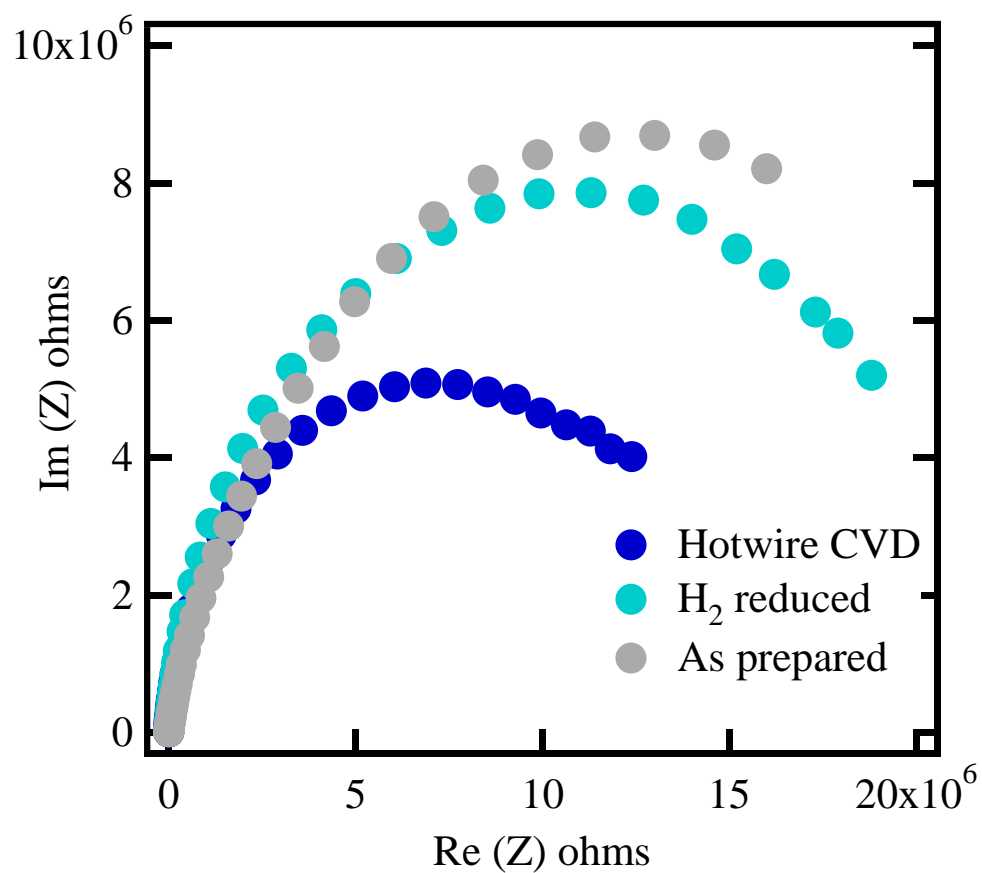


Figure 12. Nyquist plots of two probes ac impedance measurements for as prepared MoO_3 , H_2 reduced MoO_3 and HWCVD synthesized MoO_3 . Nyquist plots were obtained using the frequency range 1GHz to 1MHz ac frequency range

CURRICULUM VITAE

Ruchira Ravinath Dharmasena

EDUCATION:

- 2014 - 2019 Doctor of Philosophy (PhD)
Energy Storage-Li batteries
Department of Physics & Astronomy- University of Louisville-USA
Thesis Advisor: Dr. Gamini Sumanasekera, GPA: 3.78
- 2012 - 2014 Master of Science (MSc)
University of Louisville-Department of Physics
Thesis Advisor: Dr. Gamini Sumanasekera
- 2005 - 2009 Bachelor of Science (BSc)
Physics
University of Peradeniya-Sri Lanka

RESEARCH/ TEACHING EXPERIENCE:

- ❖ Research Assistant, University of Louisville-Conn Center for Renewable Energy Research (2014-2019)
 - Material synthesis for cathodes and anodes of Li batteries and electrode fabrication including slurry preparation and coating.
 - Electrochemical testing of Li batteries: Galvanostatic and Potentiostatic
 - Researched on high energy density electrode materials for novel Li battery technologies.

- ❖ Worked as a graduate teaching assistant in the Department of Physics and the Department of Chemistry of University of Louisville
 - Conducted entry level labs, covering topics such as classical mechanics, electromagnetism and elementary chemical synthesis. Also assisted for undergraduates those who had difficulties on understanding subject matter questions.

Relevant course work: Solid state theory, Quantum mechanics, Classical mechanics, Semiconductors and MEMS (micro-electro-mechanical systems) fabrication, Semiconductor theory, Physical electronics, Thermodynamics and statistical mechanics.

AREAS OF EXPERTISE:

- ❖ Lithium sulfur/Lithium ion battery fabrication and material synthesis, Experience in battery testing: capacity (ARBIN battery tester)/impedance/cyclic voltammetry, Coin cell fabrication and high capacity pouch cell fabrication. Experience in maintaining dry glove boxes and battery assembling machines.
- ❖ Extensive hands-on experience in working with hot filament chemical vapor deposition (HFCVD), Atomic layer deposition (ALD), RF Plasma reactors, Sputtering, Multi-zone quartz tube furnaces, vacuum pumps (mechanical, diffusion, turbo)
- ❖ In-depth knowledge in material and electrode analysis techniques and instruments such as: scanning electron microscope (SEM), X-ray diffraction (XRD), X-ray photoelectron spectroscopy (XPS), Raman spectroscopy, BET surface area/porosity analysis, Energy-dispersive X-Ray spectroscopy (EDAX), Scanning differential thermogravimetric analysis (SDT), Thermogravimetric analysis (TGA), Thermal Evaporation, Chemical vapor deposition (CVD).

AWARDS & ACHIEVEMENTS:

- ❖ First place for the business model at IDEA STATE U regional entrepreneurship competition (2016)
 - Manufacturing of battery packs for lightweight electric bicycles and other campus-friendly vehicles.
 - Launched a program to manufacture electric bicycles for in-campus travelling of student and staff
- ❖ Entrepreneur Prize-Business School-University of Louisville (2016)
- ❖ Filed a patent based on my research regarding Electrochemical study of sulfur cathode and Si decorated Lithium Molybdenum oxide anode full cell
- ❖ Achieved a special degree in physics with honors (2009 Bachelor of Science)

Patents:

1. Electrochemical study of sulfur cathode and Si decorated Lithium Molybdenum oxide anode full cell (Research Disclosure number: 17040).

Refereed Publications:

1. Mesoporous TiO₂ coating on carbon-sulfur cathode for Li-Sulfur battery, Ruchira Dharmasena, Arjun K.Thapa, Ram Krishna Hona, Jacek Jasinski, Mahendra Sunkara, Gamini U. Sumanasekera, RSC Adv., 2018, 8, 11622.
2. The prospects of phosphorene as an anode material for high-performance lithium-ion batteries: a fundamental study, Congyan Zhang, Ming Yu, George Anderson, Ruchira Dharmasena and Gamini Sumanasekera, Nanotechnology, 2017, 28 075401.
3. Study of nitrogen doping of graphene via in-situ transport measurements, Rong Zhao, Tareq Afaneh, Ruchira Dharmasena, Jacek Jasinski, Gamini Sumanasekera and Victor Henner, Physics B Condensed Matter, 2016, 490, 21–24.
4. In situ transport measurements and band Gap formation of fluorinated graphene, Rong Zhao, Ruwantha Jayasingha, Andriy Sherehiy, Ruchira Dharmasena, Meysam Akhtar, Jacek B. Jasinski, Shi-Yu Wu, Victor Henner and Gamini U. Sumanasekera, J. Phys. Chem. C 2015, 119, 20150–20155.
5. Fabrication of CdS/CdTe-based thin film solar cells using an electrochemical technique. I. M. Dharmadasa, P. A. Bingham, O. K. Echendu, H. I. Salim, T. Druffel, R. Dharmadasa, G. U. Sumanasekera, Ruchira Dharmasena, M. B. Dergacheva, K. A. Mit , K. A. Urazov, L. Bowen, M. Walls and A. Abbas, Coatings 2014 4:380-415.
6. Optimization of Multi-Walled Carbon Nanotube based CF_x electrodes for improved primary and secondary battery performances, Ruwantha Jayasinghe, Arjun Kumar Thapa, Ruchira R. Dharmasena, Tu Quang Nguyen, Bhabendra K. Pradhan, Hem Sharma Paudel, Jacek B. Jasinski, Andriy Sherehiy , Masaki Yoshio, G.U. Sumanasekera, Journal of Power Sources, 2014 253:404–411.
7. MOS tunneling strain sensor using an AC measurement technique. Li Zhu, Ruchira Dharmasena, Shamus McNamara. Annual IEEE International Conference on Nano/Micro Engineered and Molecular Systems 2013.
8. Electrochemical study of sulfur cathode and Si decorated lithium molybdenum oxide (Li_{1.33}Mo_{0.66} O₂) anode full cell. Ruchira Dharmasena, Arjun K.Thapa, Jacek Jasinski, Mahendra Sunkara, Gamini U. Sumanasekera (Manuscript in preparation).

Oral presentation: ECS 229th conference 2016 San Diego, CA, A novel sulfur cathode architecture for high capacity and durable Li-S battery, abstract-MA2016-01 240.